



January 2014

# Investigation Of The Seasonal Variations Of Aerosol Physicochemical Properties And Their Impact On Cloud Condensation Nuclei Number Concentration

Timothy Logan

Follow this and additional works at: <https://commons.und.edu/theses>

---

## Recommended Citation

Logan, Timothy, "Investigation Of The Seasonal Variations Of Aerosol Physicochemical Properties And Their Impact On Cloud Condensation Nuclei Number Concentration" (2014). *Theses and Dissertations*. 1679.  
<https://commons.und.edu/theses/1679>

This Dissertation is brought to you for free and open access by the Theses, Dissertations, and Senior Projects at UND Scholarly Commons. It has been accepted for inclusion in Theses and Dissertations by an authorized administrator of UND Scholarly Commons. For more information, please contact [zeinebyousif@library.und.edu](mailto:zeinebyousif@library.und.edu).

INVESTIGATION OF THE SEASONAL VARIATIONS OF AEROSOL PHYSICO-  
CHEMICAL PROPERTIES AND THEIR IMPACT ON CLOUD CONDENSATION  
NUCLEI NUMBER CONCENTRATION

by

Timothy S. Logan  
Bachelor of Arts, University of Virginia, 1993  
Master of Science, University of North Dakota, 2009

A Dissertation  
Submitted to the Graduate Faculty

of the

University of North Dakota

in partial fulfillment of the requirements

for the degree of

Doctor of Philosophy

Grand Forks, North Dakota

August  
2014

Copyright 2014 Timothy S. Logan

This dissertation, submitted by Timothy S. Logan in partial fulfillment of the requirements for the Degree of Doctor of Philosophy from the University of North Dakota, has been read by the Faculty Advisory Committee under whom the work has been done and is hereby approved.

---

Dr. Baike Xi

---

Dr. Xiquan Dong

---

Dr. Jianglong Zhang

---

Mike Poellot

---

Dr. Zhanqing Li

---

Dr. Michael Mann

This dissertation meets the standards for appearance, conforms to the style and format requirements of the Graduate School of the University of North Dakota, and is hereby approved.

---

Dr. Wayne Swisher, Dean

---

Date

## PERMISSION

Title            Investigation of the Seasonal Variations of Aerosol Physico-chemical  
                         Properties and Their Impact on Cloud Condensation Nuclei Number  
                         Concentration

Department    Atmospheric Sciences

Degree           Doctor of Philosophy

In presenting this dissertation in partial fulfillment of the requirements for a doctoral degree from the University of North Dakota, I agree that the library of this University shall make it freely available for inspection. I further agree that permission for extensive copying for scholarly purposes may be granted by the professor who supervised my dissertation work or, in his absence, by the chairperson of the department or the dean of the Graduate School. It is understood that any copying or publication or other use of this thesis or part thereof for financial gain shall not be allowed without my written permission. It is also understood that due recognition shall be given to me and to the University of North Dakota in any scholarly use which may be made of any material in my thesis.

Signature \_\_\_\_\_  
                         Timothy Logan

Date                    5/27/2014

## TABLE OF CONTENTS

LIST OF FIGURES .....	ix
LIST OF TABLES .....	xiii
ACKNOWLEDGEMENTS .....	xiv
ABSTRACT .....	xv
CHAPTER	
I.    INTRODUCTION .....	1
Aerosol Properties and Transport .....	1
Aerosol Indirect Effect.....	5
Purpose and Significance of this Dissertation .....	5
II.   DATASETS AND INSTRUMENTATION .....	7
Datasets .....	7
Particle Size Distribution .....	7
Aerosol Optical Depth and Angström Exponent .....	11
Absorption Aerosol Optical Depth and Absorption Angström Exponent .....	12
Single Scattering Albedo and Single Scattering Co-albedo.....	13
Hybrid Single Particle Lagrangian Integrated Trajectory Model.....	14
Instrumentation .....	14
Aerosol Robotic Network .....	14

	Aircraft Instruments .....	16
	Differential absorption LIDAR .....	17
	Nephelometer .....	18
	Particle soot absorption photometer .....	19
	Atmospheric Radiation Measurement Mobile Facility ...	19
	CALIPSO Satellite Observations.....	21
	MODIS Satellite Observations .....	22
	Dissertation Study Regions .....	24
III.	THEORETICAL DATABASE COMPARISON STUDY .....	26
	Theoretical Mineral Dust Model .....	27
	Methodology .....	29
	Meteorological Conditions .....	29
	Mineral Dust Properties Inferred from the Particle Volume Size Distribution, AOD, AAOD, $AE_{AOD}$ , and $AAE_{AOD}$ Parameters ...	32
	Comparisons of $\omega_o(\lambda)$ Between Theoretical Calculations and AERONET Retrievals.....	38
	Aerosol Radiative Effect .....	43
IV.	METHODOLOGY .....	47
	Aerosol Classification at Four Selected Single Mode Aerosol Dominated Sites .....	47
	Aerosol Classification Method Involving $AE_{AOD}$ and $\omega_{oabs}$ .....	51
	Aerosol Transport .....	53
V.	RESULTS AND DISCUSSIONS .....	56
	SQ1: What Are the Seasonal and Regional Variations of Aerosol Physico-chemical Properties at Four Selected Asian Sites? .....	56

Annual and Seasonal Aerosol Size Distributions .....	56
Seasonal Variation of Aerosol Optical Depth.....	59
Seasonal Variation of Absorption Aerosol Optical Depth.....	60
Seasonal Variation of Angström Exponent.....	61
Seasonal Variation of Absorption Angström Exponent...	62
Spectral Dependences of AOD, AAOD, and $\omega_{\text{obs}}$ .....	64
Aerosol Classification Method Involving $AE_{\text{AOD}}$ and $\omega_{\text{obs}}$ .....	67
SQ2: How Do These Aerosol Properties Change During Transpacific and Intra-continental Long Range Transport? .....	70
Asian Aerosol Transport.....	71
Biomass Burning Aerosol Transport over the Northern Great Plains .....	81
Biomass smoke plume transport .....	82
Biomass smoke plume optical properties .....	85
Biomass smoke plume physico-chemical properties.....	86
Biomass smoke plume radiative properties .....	91
SQ3: What Are the Impacts of Aerosol Properties on Marine Boundary Layer Cloud Condensation Nuclei Number Concentration? .....	94
Seasonal Aerosol Properties over the Azores .....	94
Aerosol Properties of Six Selected Cases and their Impacts on MBL $N_{\text{CCN}}$ .....	98
VI. CONCLUSIONS .....	113
The First Scientific Question .....	113

The Second Scientific Question .....	114
The Third Scientific Question .....	115
Future Areas of Research.....	117
APPENDICES .....	121
REFERENCES .....	131

## LIST OF FIGURES

Figure	Page
1. Global map of simulated aerosol transport from source to sink regions over land and ocean.....	3
2. The three aerosols modes: nucleation, accumulation, and coarse and corresponding number ( $dN/d\ln R$ ), surface area ( $dA/d\ln R$ ), volume ( $dV/d\ln R$ ) lognormal size distributions. ....	8
3. Particle volume size distribution of two pollution regions (NASA Goddard and Mexico City), a mineral dust region (Solar Village), and a biomass burning region (Alta Floresta).....	11
4. Global network of AERONET observation stations. ....	15
5. NASA DC-8 flight tracks during the 2006 INTEX-B field campaign from the Logan et al. (2010) study.....	17
6. The AMF-Azores and Graciosa AERONET sites used during the Clouds, Aerosol, and Precipitation in the Marine Boundary Layer (CAP-MBL) campaign are located on Graciosa Island. ....	20
7. Example of a biomass burning smoke plume captured over the Atmospheric Radiation Measurement-Southern Great Plains (ARM-SGP) facility as observed by CALIPSO. ....	22
8. Moderate Resolution Imaging Spectroradiometer (MODIS) Terra image of the biomass smoke plume from Figure 7 that spanned the Gulf of Mexico and was observed by the ARM-SGP facility (red star). ....	24
9. Combination of AERONET sites (stars) and study regions (boxes) for Asian aerosol properties and transport (white and red), North American aerosol properties and transport (blue), and aerosol impacts on marine CCN. ....	25
10. (a) 850 hPa geopotential heights showing the low pressure (purple) and high pressure systems (orange) and the inferred wind patterns as a result of their positions for the winter and (b) spring cases. ....	31
11. Particle volume size distributions of the (a) winter and (b) spring cases.....	33
12. Spectral dependence of AOD for the (a) winter and (b) spring cases. ....	34
13. Same as Fig. 12 but for AAOD. ....	35

14.	Comparison between the observed (solid) and theoretically calculated (dashed) $\omega_o$ for the winter (red circle) and spring (blue box) cases at (a) SACOL, (b) Xianghe, and (c) Taihu. ....	41
15.	Same as Fig. 14 but in this case the effective radius is held constant while the index of refraction varies. ....	42
16.	AERONET retrieved (a) AOD and (b) AAOD spectral dependences for single mode dominated sites from the Chung et al. (2012) study. ....	47
17.	Log-log relationship of the mean extinction aerosol optical depth (AOD) spectral dependence for all aerosol cases at each single mode aerosol site. ....	49
18.	Classification of four AERONET sites representing weakly absorbing (NASA Goddard) and strongly absorbing (Mexico City) pollution, mineral dust (Solar Village) and biomass burning (Alta Floresta) aerosol types. ....	52
19.	Aerosol volume size distributions over the four selected AERONET sites. ....	57
20.	Monthly means of the aerosol optical depth (AOD) parameter at the 440 nm wavelength. ....	60
21.	Same as Fig. 20 but for absorption aerosol optical depth (AAOD). ....	61
22.	Same as Fig. 20 but for the Angström exponent with a spectral range of 440-870 nm. ....	62
23.	Same as Fig. 20 but for the absorption Angström exponent. ....	63
24.	(a) Log-log relationship of the mean extinction aerosol optical depth spectral dependence for all aerosols cases at each AERONET site: 2001-2010 (Xianghe), 2005-2010 (Taihu), 2006-2011 (SACOL), and 2003-2009 (Mukdahan). ....	65
25.	$AE_{AOD}$ and $\omega_{obs}$ classification of the aerosol physico-chemical properties over the four selected AERONET sites. ....	67
26.	Transpacific transport of Asian aerosol plume (10 April 2006) intercepted by DC-8 aircraft over the eastern remote Pacific Ocean on 17 April 2006. ....	72
27.	Averaged MODIS AOD values with $0.5^\circ \times 0.5^\circ$ grid box during INTEX-B IOP the period 17 April-15 May 2006 on (a) Aqua and (b) Terra, and (c) their overall transpacific transport zonal trend. ....	73

28.	Aerosol scattering ratios observed by Differential Absorption LIDAR (DIAL) onboard the DC-8 aircraft during the INTEX-B field campaign over the remote Pacific Ocean.....	75
29.	(a,b) Case I and (c,d) Case II.....	77
30.	The NOAA HYSPLIT backward trajectories of dust plumes intercepted by DC-8 aircraft (denoted by black circles) over the remote Pacific Ocean for (a) Case I (2100 UTC 17 April 2006), (b) Case II (0300 UTC 24 April 2006), (c) Case III (0200 UTC 29 April 2006), and (d) Case IV (0400 UTC 29 April 2006). ....	80
31.	Aerosol loading of smoke plumes as evidenced by the periodic increase and decrease of the hourly aerosol optical depth (AOD) observed by the newly installed Grand Forks AERONET site (47.91°N, 97.32°W). ....	83
32.	HYSPLIT backward trajectories of the six cases (with the same color code as Fig. 30). ....	84
33.	Navy Aerosol Analysis and Prediction System (NAAPS) model output ( <a href="http://www.nrlmry.navy.mil/aerosol/">http://www.nrlmry.navy.mil/aerosol/</a> ) showing the locations of the wildfire source regions (dark red regions) for Cases (a) III, (b) V, and (c) VI while (d), (e), and (f) show the smoke plumes for the respective cases over Grand Forks (black circle).....	85
34.	Daily mean AERONET retrieved (a) particle volume size distributions and the spectral dependences of (b) AOD, (c) AAOD, and (d) $\omega_{\text{oabs}}$ for the six selected cases.....	86
35.	Monthly mean and standard deviation of Graciosa AERONET retrieved (a) AOD and (b) AE and (c) AMF-Azores mean wind speeds during CAP-MBL...	95
36.	AERONET retrieved yearly and seasonal mean aerosol (a) volume and (b) number size distributions.....	97
37.	AERONET retrieved (a) volume and (b) number size distributions as well as the (c) spectral dependences for the five selected cases.....	99
38.	Cases I, II, IV, and V AOS measured aerosol properties as classified by the Logan et al. (2013a) method: $AE_{\text{neph}} > 0.75$ ( $< 0.75$ ) for fine (coarse) mode, and $\omega_{\text{oabs}} < 0.07$ ( $> 0.07$ ) for weak (strong) absorption. ....	100
39.	HYSPLIT backward trajectories at 1.5-km level (solid lines) for the five selected cases.....	102

40.	(a-c) Scattering coefficient ( $\sigma_{sp}$ ) and fine mode fraction (FMF), (d-f) absorption coefficient ( $\sigma_{ap}$ ), and (g-i) CCN from hourly averaged AMF-Azores AOS observations.....	105
41.	Correlation plots (r-values) between CCN number concentration ( $N_{CCN}$ ) and $\sigma_{sp450}$ .....	110
42.	The log-log AIE relationships of the cloud base retrieved $r_e$ and surface measured $\sigma_{sp}$ for the (a) 10 July 2009 dust case, (b) 9 May 2010 volcanic ash case, and (c) 13 May 2010 pollution case during the CAP-MBL campaign conducted over the Azores. ....	119
A1.	Number size distributions for the (a) individual cases using the AERONET bin radius $R$ instead of the effective radius of the aerosol particle ( $r_e$ ) as well as the (b) yearly and seasonal means.....	124
B1.	Scatterplots of (a) total cation vs. total anion and (b) calcium vs. carbonate (cation-anion difference).....	125
B2.	Scatterplots of (a) anthropogenic (pollution) cations vs. anions and (b) sea salt ions ( $Na^+$ vs. $Cl^-$ ).....	128
B3.	Aerosol classification method using $Ca^{2+}$ concentration observations for (a) Case I, (b) Case II, and (c) Cases III and IV.....	129

## LIST OF TABLES

Table	Page
1. Summary of the AERONET retrieved aerosol optical properties for the winter and spring cases. ....	36
2. Summary of the theoretical model parameters used in this study. ....	37
3. Summary of the AERONET calculated BOA and TOA aerosol radiative effect (ARE) values. ....	44
4. Summary of statistical data from the four AERONET sites. ....	70
5. A summary of the physical and optical properties of the four selected Asian dust events intercepted by the DC-8 aircraft. ....	79
6. A summary of the mean AOD, AE, and AAE values for the six cases. ....	90
7. Hourly retrievals of aerosol radiative forcing (ARF) and aerosol radiative forcing efficiencies ( $ARF_{eff}$ ) at the surface for the six selected cases. ....	93
8. Summary of mean $AOD_{440}$ , Angström exponent (AE), and fine mode fraction (FMF) values for the five selected cases at the AMF-Azores site. ....	112

## ACKNOWLEDGEMENTS

Thank you to my beloved grandmother and my family for shaping my mind through the years. Thank you to all my friends at Morris School District in New Jersey who believed in me and helped me to realize that learning should always be lifelong, meaningful, and challenging. Thank you to my advising committee of Dr. Baike Xi, Dr. Xiquan Dong, Dr. Jianglong Zhang, Prof. Mike Poellot, Dr. Zhanqing Li, and Dr. Michael Mann for their guidance, expertise, and support. Thank you to UND At. Sci. and the Newman Center for all your help during the good and bad times. You never let me forget who I am and what I am capable of accomplishing.

This dissertation was partially supported by the North Dakota Space Grant Consortium, National Aeronautic and Space Administration (NASA), National Science Foundation (NSF), and the Department of Energy (DOE). All AERONET data was provided by the website located at <http://aeronet.gsfc.nasa.gov/> and I am grateful for all PI's in North America, Asia, and Africa. The HYSPLIT transport model was provided by the NOAA Air Resources Laboratory (ARL) and can be found at the READY website (<http://ready.arl.noaa.gov/>). Additional data was provided by the DOE Atmospheric Radiation Measurement (ARM) program located at [www.archive.arm.gov](http://www.archive.arm.gov). I also wish to thank all other scientists and friends in the United States, China, and other countries abroad for their help. It was an honor to work and collaborate with them during the past seven years. Their advice and input has been greatly appreciated and I look forward to future collaboration.

## ABSTRACT

Aerosols are among the most complex yet widely studied components of the atmosphere not only due to the seasonal variability of their physical and chemical properties but also their effects on climate change. The three main aerosol types that are known to affect the physics and chemistry of the atmosphere are: mineral dust, anthropogenic pollution, and biomass burning aerosols. In order to understand how these aerosols affect the atmosphere, this dissertation addresses the following three scientific questions through a combination of surface and satellite observations:

SQ1: What are the seasonal and regional variations of aerosol physico-chemical properties at four selected Asian sites?

SQ2: How do these aerosol properties change during transpacific and intra-continental long range transport?

SQ3: What are the impacts of aerosol properties on marine boundary layer cloud condensation nuclei number concentration?

This dissertation uses an innovative approach to classify aerosol properties by region and season to address SQ1. This is useful because this method provides an additional dimension when investigating the physico-chemical properties of aerosols by linking a regional and seasonal dependence to both the aerosol direct and indirect effects. This method involves isolating the aerosol physico-chemical properties into four separate regions using AERONET retrieved Angström exponent ( $AE_{AOD}$ ) and single scattering albedo ( $\omega_{obs}$ ) to denote aerosol size and absorptive properties. The aerosols events are

then clustered by season. The method is first applied to four AERONET sites representing single mode aerosol dominant regions: weakly absorbing pollution (NASA Goddard), strongly absorbing pollution (Mexico City), mineral dust (Solar Village), and biomass burning smoke (Alta Floresta). The method is then applied to four Asian sites that represent complicated aerosol components.

There are strong regional and seasonal influences of the four aerosol types over the selected four Asian sites. A strongly absorbing mineral dust influence is seen at the Xianghe, Taihu, and SACOL sites during the spring months (MAM) as given by coarse mode dominance. There is a shift towards weakly absorbing pollution (sulfate) and biomass (OC) aerosol dominance in the summer (JJA) and autumn (SON) months as given by a strong fine mode influence. A winter season (DJF) shift toward strongly fine mode, absorbing particles (BC and OC) is observed at Xianghe and Taihu. At Mukdahan, a strong fine mode influence is evident year round with weakly and strongly absorbing biomass particles dominant in the autumn and winter months, respectively, while particles exhibit variable absorption during the spring season.

To address SQ2, four cases are selected in Asia to investigate how the optical properties of Asian aerosol plumes change during transport across the remote Pacific Ocean. In addition, six strong smoke events are selected to investigate how the physical and chemical properties of biomass smoke aerosols change during transport in North America. From four selected Asian cases, it was shown by DC-8 aircraft in situ measurements that the Asian plumes contained varying amounts of mineral dust and pollution aerosols during transport. In addition, backward trajectory analysis identified two main dust source regions (Gobi and Taklamakan deserts) and urban/industrial

pollution regions in central and eastern China. During the anomalously active wildfire season of 2012 in North America, strong smoke events were observed over the Northern Great Plains region by the Grand Forks, North Dakota, AERONET site and selected as cases. The spectral dependences of absorption aerosol optical depth (AAOD) and  $\omega_{\text{oabs}}$  illustrated the varying absorption of the smoke plumes due to carbonaceous particle influences. The AAOD parameter was found to be primarily influenced by aerosol particle size while  $\omega_{\text{oabs}}$  was more sensitive to the carbonaceous content. The aerosols likely contain strongly absorbing carbonaceous particles generated from the flaming combustion mode. The cases represented complex mixtures of the flaming and smoldering combustion phases.

Lastly, SQ3 is addressed by using a multi-platform dataset from the Clouds, Aerosol, and Precipitation in the Marine Boundary Layer (CAP-MBL) Graciosa, Azores, 2009-2010 field campaign. The seasonal aerosol particle volume and number size distributions, AOD, and  $AE_{\text{AOD}}$  during the CAP-MBL campaign have shown that a low overall mean  $\text{AOD}_{440}$  of 0.12 denoted a clean environment over this region that typically contains MBL sea salt. In terms of aerosol volume, a bimodal signal was prominent where the coarse mode influence ( $r \geq 1 \mu\text{m}$ ) dominated that of the fine mode ( $r < 1 \mu\text{m}$ ) throughout the year. However, there are considerable continental fine mode aerosols advected to the Azores region during summer months, including Saharan mineral dust, volcanic ash, biomass smoke, and pollution from North American as identified by HYSPLIT backward trajectories. These aerosol types have been shown to have impacts on MBL cloud condensation nuclei (CCN) that are likely different from coarse mode marine aerosols (e.g., sea salt) (Rémillard et al. 2014; Wood et al. 2014). The alternating

presence of dominant clean air masses with periodic episodes of polluted air masses will provide a substantial variety in aerosol properties during the summer. This will provide a great opportunity to investigate the interactions between aerosol and cloud properties in terms of the aerosol indirect effect (AIE).

## **CHAPTER I**

### **INTRODUCTION**

Aerosols have an impact on global/regional climate change through their direct radiative effects by changing the optical properties of the Earth's atmosphere specifically through the scattering and absorption of both solar and thermal infrared radiation (Tanré et al. 2001). As a result, aerosols ultimately act as negative radiative forcing agents by reducing the amount of direct downwelling solar radiation to the surface creating a cooling effect (Ramanathan et al. 2001; Li et al. 2007a, b; Bergstrom et al. 2007). In addition, aerosols indirectly affect the climate by altering cloud microphysical properties such as cloud albedo, lifetime and precipitation (Li et al. 2007a, b; IPCC 2007; Ramanathan et al. 2001). What is not well known is the effects different types of aerosols (e.g., mineral dust, pollution, biomass burning) may have on cloud formation processes. Hence, studying the transport of aerosols plays a vital role in the understanding of regional and global climate change.

#### **Aerosol Properties and Transport**

Over the past few decades, numerous field campaigns have been carried out to investigate the impact of aerosol transport on downwind regions. Major studies include the Pacific Exploratory Mission (PEM) (Bachmeier et al. 1996), East Asian Studies of Tropospheric Aerosols: An International Regional Experiment (EAST-AIRE) (Li et al. 2007a, b), Transport and Chemical Evolution-Pacific (TRACE-P) in 2001 (Huebert et al.

2003; Jacob et al. 2003), Intercontinental Chemical Transport Experiment-Phase B (INTEX-B) (Singh et al. 2006), Fire Lab at Missoula Experiment (FLAME) (Mack et al. 2010), and the Clouds, Aerosol, and Precipitation in the Marine Boundary Layer (CAP-MBL) (Rémillard et al. 2012; Wood et al., 2014; Dong et al. 2014) field campaigns.

The PEM, TRACE-P, and ACE-Asia field campaigns investigated the impacts of Asian dust transport from source regions in the Gobi and Taklamakan Deserts to regions several hundreds to thousands of kilometers downwind. These field campaigns made use of ground-based and satellite retrievals and in situ aircraft measurements in the vicinity of the Asian mainland (ACE-Asia) as well as the remote Pacific Ocean (PEM and TRACE-P). As a result, many studies on the effects of Asian dust and pollution on the atmosphere have been and continue to be published. The more recent INTEX-B field campaign added aerosol chemical measurements to the wealth of aerosol physical data gathered by the other Asian campaigns. Chemical species such as calcium, sulfate, and organic carbon compounds could now be used to track the behavior of Asian dust, pollution, and biomass burning aerosols during transport, respectively.

Urban/industrial pollution, biomass burning smoke, and mineral dust particles originating from various source regions around the globe (e.g., Asia, Africa, Europe, and the Americas) have been studied over recent decades and continue to be of great importance when investigating their impacts on the climate and human health. The ongoing urbanization/industrialization in Asia, recent Saharan dust episodes in Africa, and pollution and biomass smoke events originating in the Americas and Europe have greatly added to the wide variety of aerosols observed in the atmosphere (Figure 1). This in turn has increased the level of uncertainty when evaluating global climate change

(Hansen and Sato 2001; Bergstrom et al. 2007; Eck et al. 2010; Logan et al. 2013a, c; Logan et al. 2014).

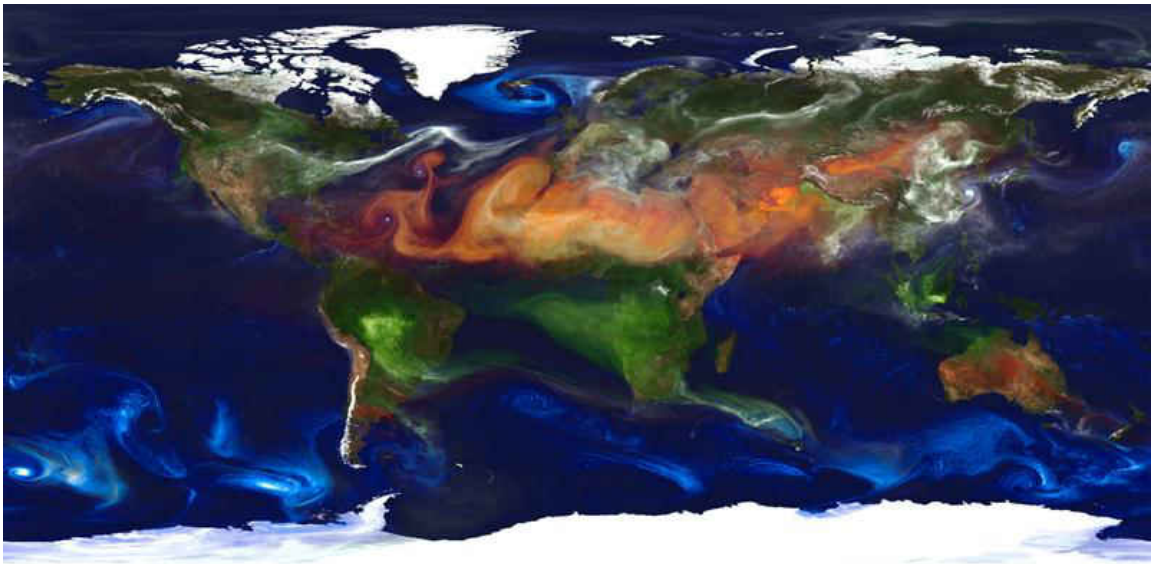


Figure 1. Global map of simulated aerosol transport from source to sink regions over land and ocean. Urban/industrial pollution (white), mineral dust (orange), biomass burning (green), and sea salt particles (light blue) are all represented. Courtesy of the NASA Goddard Earth Observing System Model, Version 5 (GEOS-5) (<http://gmao.gsfc.nasa.gov/GEOS/>).

Urban/industrial pollution is typically generated in or near large urban centers around the globe but is more concentrated in the Northern Hemisphere. Pollution aerosols consist primarily of sulfate, nitrate, and carbonaceous particles. The carbonaceous particles are comprised of strongly absorbing black and organic carbon (BC and OC) compounds which drive the absorption potential of the aerosols. Moreover, the absorptive properties of these aerosols have been shown to have a seasonal dependence (Logan et al. 2013a). Biomass burning aerosols are generated by both natural and anthropogenic processes such as wildfires and controlled agricultural burning. They are comprised primarily of carbonaceous particles whose absorptive properties depend on combustion temperature. For example, the high temperature flaming mode

tends to generate more strongly absorbing BC while the low temperature smoldering mode generates both weakly and strongly absorbing OC (Reid and Hobbs 1998; Reid et al. 1998; Lewis et al. 2008; Mack et al. 2010; Jacobson 2012).

Mineral dust aerosols strongly contribute to the aerosol direct effect and represent the largest uncertainty in radiative forcing (IPCC 2001, 2007). The largest mineral dust source regions in the world are found within the Asian and African continents. Strong Asian dust episodes are more probable and intense during the spring months (Li et al. 2007b; Huang et al. 2008a; Yang et al. 2008; Logan et al. 2010; Logan et al. 2013a, b) but can occur during any season. Under specific meteorological conditions (e.g., wind speeds greater than  $5 \text{ m s}^{-1}$  associated with a low-pressure system and a dry spring season), mineral dust and soil can be lofted into the free atmosphere and can be transported from Asia to North America via the Pacific Ocean (Murayama et al. 2001; Husar et al. 2001; Tsunematsu et al. 2005; Logan et al. 2010). In addition, the mineral dust can mix with regional urban/industrial pollution and biomass smoke along the transport pathway which creates more difficulty when investigating their impacts on global climate.

Similarly, Saharan dust is often transported across great distances due to favorable meteorological conditions (Logan et al. 2014). Strong high pressure systems situated in the eastern remote Atlantic Ocean during the late spring and summer seasons can transport Saharan dust, previously lofted into the atmosphere by continental low pressure systems, from Africa to sink regions in the Americas and even Europe. In addition, late summer and autumn cyclones (e.g., tropical waves, hurricanes, and extratropical systems) can also transport Saharan dust to these same sink regions (Logan et al. 2014). How the

properties of mineral dust particles evolve and are then able to impact locations far distant from their origin is still under investigation.

### **Aerosol Indirect Effect**

Aerosols are known to influence atmospheric radiative transfer through the aerosol indirect effect (AIE) by changing cloud and precipitation processes. Many studies have made the attempt to investigate how the AIE will manifest itself by using a combination of observations and model simulations (Feingold et al. 2006; Rosenfeld et al. 2008; Li et al. 2011; Rémillard et al. 2012; Dong et al. 2014; Wood et al. 2014). In most cases, the CCN concentration ( $N_{CCN}$ ), liquid water path (LWP), cloud droplet effective radius ( $r_e$ ), cloud-droplet number concentration ( $N_C$ ), and AOD parameters are examined (Feingold et al. 2001; Feingold et al. 2003; Kim et al. 2003; Feingold et al. 2006; Tao et al. 2012). Assuming a fixed amount of precipitable water vapor in the atmosphere, an increase in aerosol loading should lead to an increase in  $N_{CCN}$  and  $N_C$  while decreasing  $r_e$  due to competition for available water vapor (Feingold et al. 2003; Tao et al. 2012). However, not all aerosols cause an increase in  $N_{CCN}$  and can thus have conflicting results when investigating their role in the AIE (Logan et al. 2014). Hence, there is a great need for more studies that take into account the nature of specific aerosol types and their impacts on cloud forming processes (Wood et al. 2014).

### **Purpose and Significance of This Dissertation**

Though the concept of aerosol classification is not new (e.g., Jeong et al. 2005; Russell et al. 2010; Chung et al. 2012), this study uses an innovative approach to classify aerosol properties by region and season. This is useful because this method provides an additional dimension when investigating the physico-chemical properties of aerosols by

linking a regional and seasonal dependence to both the aerosol direct and indirect effects.

Three scientific questions have been addressed in this dissertation:

SQ1: What are the seasonal and regional variations of aerosol physico-chemical properties at four selected Asian sites?

SQ2: How do these aerosol properties change during transpacific and intra-continental long range transport?

SQ3: What are the impacts of aerosol properties on marine boundary layer cloud condensation nuclei number concentration?

A multi-platform data analysis approach consisting of ground-based Aerosol Robotic Network (AERONET) retrievals in addition to other surface, sub-orbital, and satellite measurements as well as model output is used. Re-analysis data will be used to illustrate the meteorological conditions that are responsible for aerosol transport. Surface aerosol and CCN measurements from an intensive operating period (IOP) field campaign conducted over the eastern remote Atlantic Ocean will provide information on aerosol type and MBL  $N_{CCN}$ .

## **CHAPTER II**

### **DATASETS AND INSTRUMENTATION**

#### **Datasets**

##### **Particle Size Distribution**

Atmospheric aerosol particles can be characterized by size (Schuster et al. 2006). The size ranges fall into three general categories: Aitken (or nucleation) mode, accumulation mode, and coarse mode. Note that in this study, the nucleation and accumulation mode categories represent the fine mode. The fine mode denotes particles of radius  $\leq 1 \mu\text{m}$  while the coarse mode denotes particles have a radius  $> 1 \mu\text{m}$  (Figure 2).

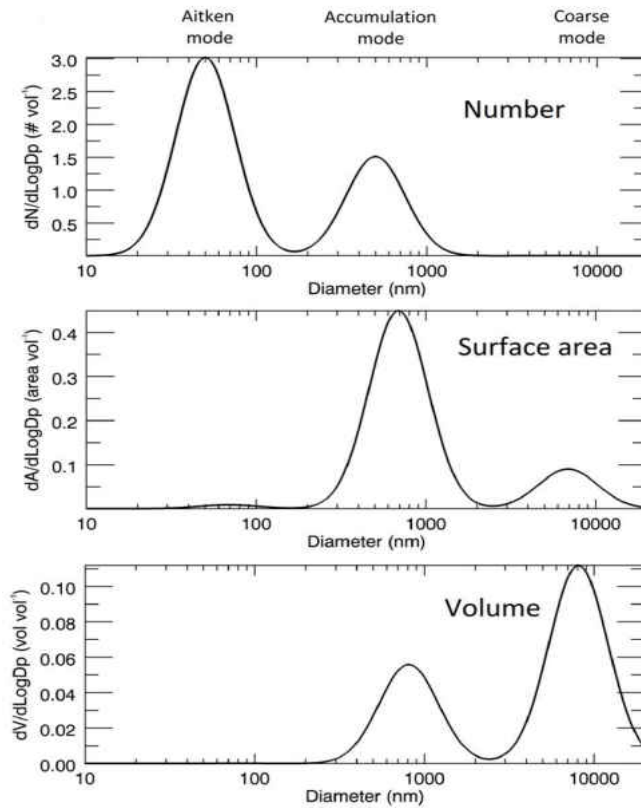


Figure 2. The three aerosols modes: nucleation, accumulation, and coarse and corresponding number ( $dN/d\ln R$ ), surface area ( $dA/d\ln R$ ), volume ( $dV/d\ln R$ ) lognormal size distributions. Note that fine mode particles dominate the number and surface area size distributions while coarse mode particles dominate the volume size distribution. Figure courtesy of Niall Robinson.

Urban/industrial pollution and biomass smoke particles are typically fine mode in size due to their manner of generation (e.g., flaming or smoldering combustion). In contrast, mineral dust particles are typically observed in the coarse mode as they are formed through the physical weathering of larger soil and rock particles. Mineral dust can also be found in the fine mode as a result of chemical reactions between the calcium and silicate compounds in the dust and acid compounds in the atmosphere such as sulfate and nitrate (McNaughton et al. 2009; Leitch et al. 2009).

The size distributions presented in Figure 2 assume a lognormal relationship between number, area, volume and the particle size (log x-axis). This is the primary assumption used in much of the aerosol community since it more accurately describes particle size distributions of typical aerosols found in the atmosphere (Schuster et al. 2006). The particle number size distribution ( $dN/d\ln R$ ) is useful in determining which mode dominates in terms of aerosol number concentration for a given range of particle radii. This is useful when determining the effects of aerosols on cloud forming processes such as growth from aerosol to cloud condensation nuclei to cloud droplet. Different types of aerosols have been known to facilitate these processes more than others. For example, hygroscopic (soluble) aerosols can readily activate as CCN while hydrophobic (insoluble) aerosols make poor CCN. The surface area size distribution ( $dA/d\ln R$ ) is more related to aerosol chemical properties. The accumulation mode dominates the size distribution since more surface area is exposed to be reacted upon (e.g., gas-to-particle and acid-base reactions) in this size range while there is a smaller peak in the coarse mode. Stochastically, the Aitken mode is too small for significant atmospheric chemical reactions to occur.

Many studies investigating aerosol optical properties use the particle volume size distribution ( $dV/d\ln R$ ) rather than  $dN/d\ln R$  because the radiative effects of atmospheric aerosols are more closely related to their volume rather than number (Schuster et al. 2006). Note that there is a difference between in situ (e.g., aircraft and ground-based) and column-integrated (e.g., AERONET and satellite) measurements of particle size distribution. In situ measurements of particle size distribution typically have number per units of sampling volume (e.g., #  $\text{cm}^{-3}$ ) while column integrated measurements have

number per units of cross-sectional area (e.g., #  $\mu\text{m}^{-2}$ ). Though these measurements are comparable, this dissertation makes the assumption that there is sufficient mixing of air between the surface and free troposphere in the atmospheric column being measured.

Figure 3 is generated from a multi-year data set of AERONET retrievals from four selected single mode dominated aerosol sites used in this dissertation. It illustrates how  $dV/d\ln R$  can be used as a general fingerprint of fine and coarse mode particle dominance for any given aerosol region (Dubovik et al. 2002; Eck et al. 2005; Logan et al. 2013a). NASA Goddard and Mexico City are located within large urban/industrial centers and thus have large fine mode influences. Solar Village is located in the vicinity of the Arabian Desert and thus has strong influences from coarse mode mineral dust. Alta Floresta is located within the Amazonian region and is susceptible to strong influences of fine mode biomass smoke particles. Bimodal distributions tend to suggest more than one type of aerosol and the total volume of the coarse and fine modes will indicate the size dominance in that region (Dubovik et al. 2002). However, this does not give much information on aerosol composition since pollution and biomass particles can yield similar size distributions.

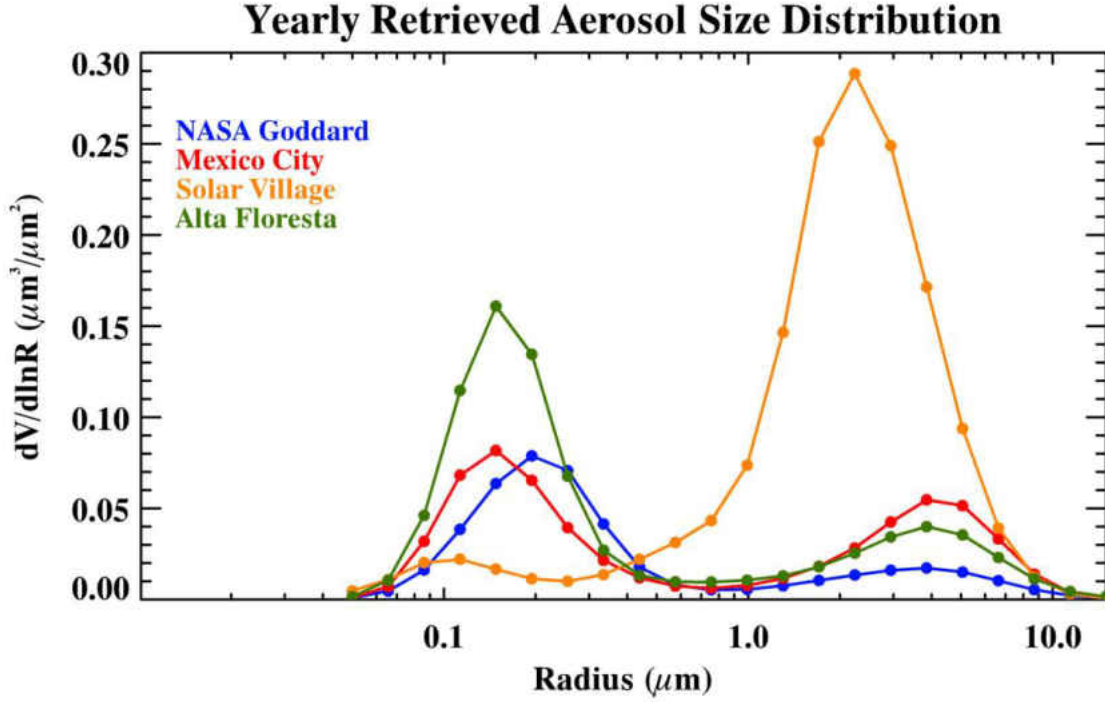


Figure 3. Particle volume size distribution of two pollution regions (NASA Goddard and Mexico City), a mineral dust region (Solar Village), and a biomass burning region (Alta Floresta). Note the fine mode dominance at NASA Goddard, Mexico City, and Alta Floresta while Solar Village is dominated by coarse mode particles.

### Aerosol Optical Depth and Angström Exponent

Aerosol optical depth (AOD) is defined as the amount of vertically integrated light extinction through a column of atmosphere and is also the sum of the scattering and absorption optical depths (SAOD and AAOD, respectively) (Eck et al. 1999). It is used as the primary parameter to quantify the magnitude of aerosol loading the atmosphere (Holben et al. 1998; Eck et al. 1999; Li et al. 2007a, b). The Angström exponent (AE) is a good indicator of particle size and is given by the following equation,

$$AE = -\frac{\log\left[\frac{AOD(\lambda_1)}{AOD(\lambda_2)}\right]}{\log\left[\frac{\lambda_1}{\lambda_2}\right]}, \quad (1)$$

where the negative log-log-slope relationship between AOD and  $\lambda$  is synonymous with the spectral dependence due to particle size (Eck et al. 1999; Schuster et al. 2006). The wavelengths ( $\lambda_1$  and  $\lambda_2$ ) used in this study are 440 nm and 870 nm, respectively.  $AE_{440-870}$  can range from negative values to much greater than 1 (Eck et al. 1999; Higurashi and Nakajima 2002; Gobbi et al. 2007). Though there are numerous studies that use an array of  $AE_{440-870}$  values to partition aerosols according to size, this dissertation adopts  $AE_{440-870} < 0.75$  to denote coarse mode particles while  $AE_{440-870} > 0.75$  denotes fine mode particles (Reid et al. 1999; Eck et al. 2005; Gobbi et al. 2007; Logan et al. 2013a).

### **Absorption Aerosol Optical Depth and Absorption Angström Exponent**

The absorption Angström exponent (AAE) parameter is calculated starting with spectral absorption aerosol optical depth (AAOD), given by

$$AAOD(\lambda) = (1 - \omega_o(\lambda)) * AOD(\lambda), \quad (2)$$

where  $\omega_o$  is the single scattering albedo and  $\lambda$  ranges between 440 and 870 nm. The same equation for AE (Eq. 1 and same  $\lambda$  range) is used to calculate AAE

$$AAE = - \frac{\log \left[ \frac{AAOD(\lambda_1)}{AAOD(\lambda_2)} \right]}{\log \left[ \frac{(\lambda_1)}{(\lambda_2)} \right]}, \quad (3)$$

where AAE is the negative log-log-slope relationship between AAOD and  $\lambda$  which can be used to relate absorption spectral dependence to particle composition (Bergstrom et al. 2004; Bergstrom et al. 2007; Russell et al. 2010).

A range of  $AAE_{440-870}$  values has been previously determined which corresponds to various aerosol types. For example, submicron BC particles typically have  $AAE_{440-870}$  close to unity (Bergstrom et al. 2007; Gyawali et al. 2009; Russell et al. 2010). Urban

pollution and biomass particles typically have  $AAE_{440-870}$  values that range from  $\sim 1$  to 2 or greater depending on the relative amounts of BC, OC, and sulfate, while mineral dust particles can be 1.5 or higher depending on chemical composition (e.g., iron oxide content) (Schuster et al. 2005; Xin et al. 2007; Lack and Cappa 2010; Russell et al. 2010; Giles et al. 2011). It should be noted that the overlap in AAE values can raise concerns for regions dominated by a mixture of aerosol types.

### **Single Scattering Albedo and Co-albedo**

The single scattering albedo ( $\omega_o$ ) parameter is defined as the ratio of particle scattering to particle extinction (e.g., SAOD/AOD). This parameter ranges between 0 (pure absorption) to 1 (pure scattering). In the atmosphere,  $\omega_o$  values are generally observed to be between 0.7 and 0.99 with a strong dependence on the internal composition of the aerosols. The  $\omega_o$  parameter is important in the aerosol community since small changes in the magnitude of  $\omega_o$  can lead to large changes in radiative forcing in the atmosphere. Aerosols have long been known to cause a cooling effect at the surface, but some aerosol types (e.g., mineral dust and BC) can warm the layer in which they reside in addition to causing a cooling effect at the surface. Many studies have shown that a change in  $\omega_o$  from 0.95 to 0.9 can change the sign of atmospheric radiative forcing from negative to positive (Takemura et al. 2002). Hence, it is very important to investigate aerosol radiative properties especially during transport from their source to sink regions.

The single scattering co-albedo ( $\omega_{oabs}$ ) (ratio of AAOD to AOD or  $1-\omega_o$ ) explains the loss of photons due to the absorption of particles. This parameter can be useful in identifying particle composition, especially carbonaceous particles (Corrigan et al. 2006).

This dissertation will use  $\omega_{\text{obs}}$  to focus on aerosol absorption rather than scattering in order to (a) reduce ambiguities in aerosol composition and (b) reveal a correlation between absorption and aerosol composition (e.g., Corrigan et al. 2006; Logan et al. 2013a).

### **Hybrid Single Particle Lagrangian Integrated Trajectory Model**

The Hybrid Single Particle Lagrangian Integrated Trajectory Model (HYSPLIT) computes the advection of a single pollutant particle by assuming a dispersion rate (Draxler and Hess, 1997; Draxler and Hess 1998; Draxler 1999; Draxler and Rolph 2012; Rolph 2012). Model inputs include: meteorological re-analysis data, trajectory mode (forward or backward), location of particles (latitude/longitude), model time span, time of model initiation (UTC time), and particle height (AGL in meters). Robock (1988), Qiu and Sun (1994), Logan et al. (2013c), and Logan et al. (2014) pointed out that aerosol particles can be transported at altitudes from just above the boundary layer (2 km) to the upper troposphere (7 km). This dissertation will use backward trajectories that temporally range from 84-240 hours to denote the probable source regions and transit times of various aerosol plumes. For example, Asian and African dust and pollution events can take up to 240 hours (10 days) to reach North America while smoke aerosols from biomass burning events can take 24-84 hours (1-3 days) or longer to disperse. The trajectory accuracy has been shown to be highly dependent on meteorological conditions and are therefore validated using satellite imagery (e.g., MODIS and CALIPSO) to ensure the spatial and temporal location of aerosol events during transport.

## **Instrumentation**

### **Aerosol Robotic Network**

The AERosol RObotic NETwork (AERONET) consists of CIMEL sun/sky radiometers placed in a world-wide framework of observation stations (Holben et al. 1998, Figure 4). The radiometers are capable of retrieving aerosol optical property products at discrete wavelengths ranging from 340 to 1020 nm (Eck et al. 2005; Schuster et al. 2006). This dissertation uses Level 1.5 (cloud screened) and Level 2.0 (cloud screened, quality assured) products to ensure data quality and accuracy (Holben et al. 2006). The aerosol products were generated using the inversion techniques developed by Dubovik and King (2000) and Dubovik et al. (2000), and quality assurance using Holben et al. (2006).

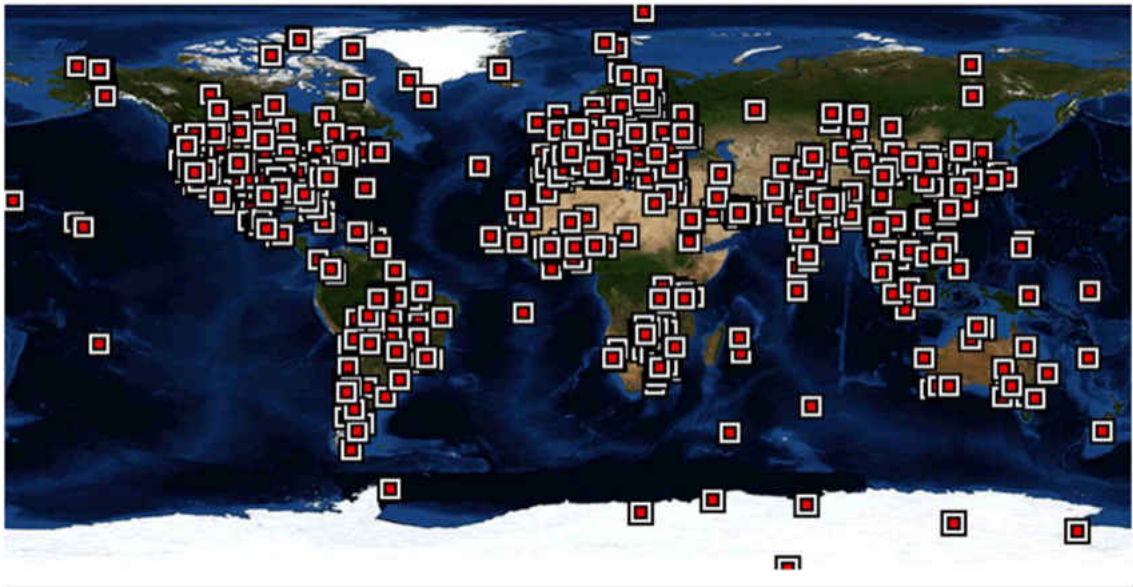


Figure 4. Global network of AERONET observation stations. Courtesy of the AERONET website ([http://aeronet.gsfc.nasa.gov/new\\_web/index.html](http://aeronet.gsfc.nasa.gov/new_web/index.html)).

The AERONET products analyzed in this study include: particle effective radius ( $r_e$ ), volume particle size distribution ( $dV/d\ln R$ ), spectral aerosol optical depth [ $AOD(\lambda)$ ], and spectral single scattering albedo [ $\omega_o(\lambda)$ ]. The number size distribution ( $dN/d\ln R$ ) can be calculated from  $dV/d\ln R$  by using  $r_e$ . This method is explained in detail in Appendix

A. Note that similar wavelength ranges between 440 and 1020 nm are used for the AERONET aerosol retrievals.

The uncertainties of AOD and  $\omega_o$  are approximately  $\pm 0.01$  and  $\pm 0.03$ , respectively, for AOD<sub>440</sub> larger than 0.4 (Holben et al. 1998; Eck et al. 1999; Dubovik et al. 2002). Filtering the retrievals based on these criteria will certainly lead to data loss. This dissertation chooses AERONET sites with at least five years of high quality, Level 2.0 data that are near or downwind of strong aerosol source regions. For example, clean regions will typically have few strong aerosol events such that approximately 20% of the retrievals can be used (see Table 4). In contrast, regions that are dominated by pollution and biomass burning will typically have AOD values greater than 0.4 throughout the year and thus there are more retrievals. Over marine regions, aerosol events are denoted by AOD values greater than twice the overall mean AOD to ensure the aerosol event was caused by long range transport rather than a local event. Level 1.5 data can also be used though the criteria involves restricting retrievals to periods when the solar zenith angle (SZA) greater than 50° in addition to the AOD criteria. Again this will certainly lead to issues of data loss. Though filtering by AOD will likely upwardly bias results, the conclusions of this dissertation are not greatly affected by using these criteria.

### **Aircraft Instruments**

The NASA DC-8 aircraft platform measured aerosol properties remotely and in-situ during ten flights (Figure 5) with a total of 85 hours over the central Pacific Ocean between Hawaii and Alaska during the 2006 INTEX-B field campaign (Logan et al. 2010). The instruments onboard the DC-8 aircraft used in this study included the

Differential Absorption Lidar (DIAL), nephelometer, and particle soot absorption photometer (PSAP).

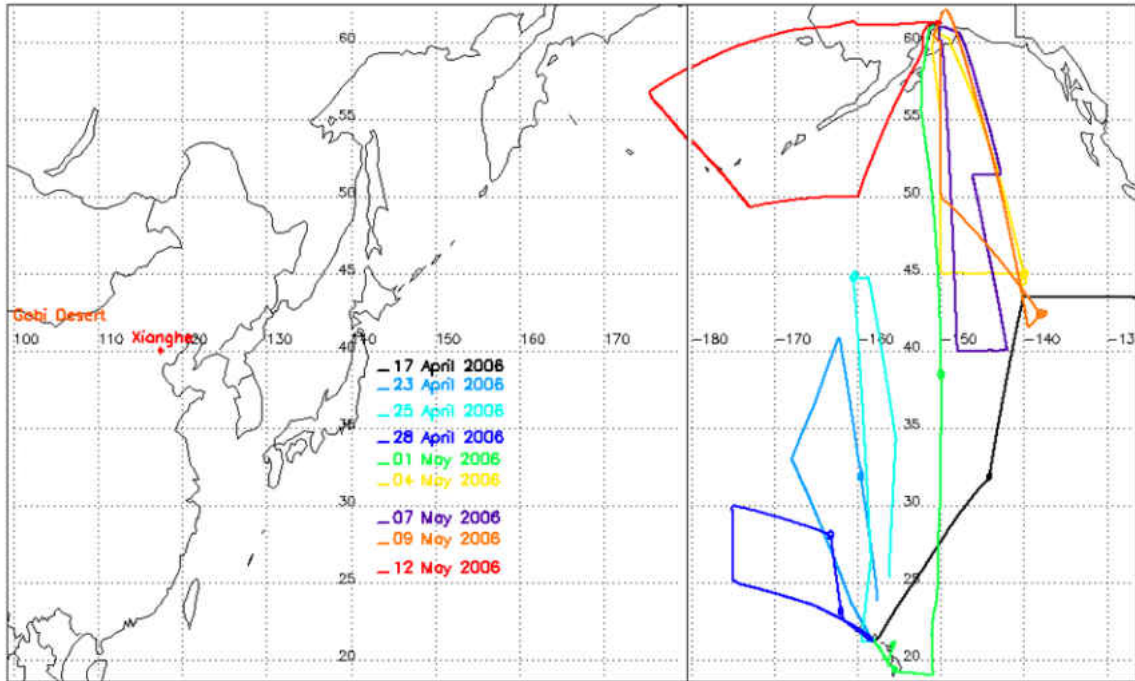


Figure 5. NASA DC-8 flight tracks during the 2006 INTEX-B field campaign from the Logan et al. (2010) study.

**Differential absorption LIDAR.** The differential absorption LIDAR (DIAL) platform, developed by the NASA Langley Research Center, remotely retrieved column integrated aerosol backscattering in both visible ( $\lambda=588$  nm) and near infrared ( $\lambda=1064$  nm) wavelengths (Browell et al. 1998). The vertical resolution of the DIAL measurement system was 30 m, a horizontal resolution of 2.3 km and a 10 s temporal resolution along the DC-8 flight track. The equation to calculate the aerosol scattering ratio,  $R_\lambda(z)$  at a given wavelength ( $\lambda$ ) is given by

$$R_\lambda(z) = \frac{\beta_1(z) + \beta_2(z)}{\beta_2(z)}, \quad (4)$$

where  $\beta_1(z)$  and  $\beta_2(z)$  are the backscattering coefficients by aerosols and air molecules at altitude  $z$ , respectively. Typical scattering ratios  $R_\lambda(z)$  are close to 1 for regions free of aerosol, and greater than 1 for the dust plumes. Note that larger sized cloud particles usually have a high scattering ratio ( $\sim 50$ ) at both wavelengths because the backscattering coefficient is proportional to sixth power of particle size ( $\sim r^6/\lambda^4$ ).

**Nephelometer.** Aerosol integrated light scattering coefficients ( $\sigma_{sp}$ ) at three wavelengths in the visible spectrum (450, 550, and 700 nm) were measured in situ by the TSI Model 3563 nephelometer onboard the DC-8 aircraft. For fine mode aerosols,  $\sigma_{sp}$  decreases with wavelength from 450 to 700 nm ( $\sigma_{sp450} > \sigma_{sp700}$ ), but for coarse mode aerosols the aerosol scattering coefficients are nearly independent of wavelength. Therefore, for fine mode aerosols, the slope of this relationship can be approximated by the nephelometer derived Angström exponent ( $AE_{neph}$ ). The equation for calculating  $AE_{neph}$  is given by

$$AE_{neph} = - [\log(\sigma_{sp\lambda_1}/\sigma_{sp\lambda_2}) / \log(\lambda_1/\lambda_2)], \quad (5)$$

where  $\sigma_{sp}$  is used as a proxy for in situ AOD at two given wavelengths  $\lambda_1$  and  $\lambda_2$ . AOD is proportional to the aerosol scattering ratio  $\beta_\lambda$ , therefore, the ratio of  $\sigma_{sp\lambda_1}$  and  $\sigma_{sp\lambda_2}$  is proportional to the ratio of  $\beta_{\lambda_1}$  and  $\beta_{\lambda_2}$ . The same criteria for AE (derived in the previous section) will be used for  $AE_{neph}$ .

Correction factors designed by Anderson and Ogren (1998) were applied to the nephelometer data prior to use in this study. First, the measurements were corrected by calibrating the instrument with gas particles since they undergo Rayleigh scattering and do not show the near-forward-scattering biases as do particles close to or greater than 1  $\mu\text{m}$  (Anderson and Ogren 1998). Second, the nephelometer measurements were

corrected to 0° - 180° from its original detection angles of 7° - 170°. The temporal resolution of sampling is 1 minute but the data are averaged at one hour intervals in order to limit instrument noise (Jefferson 2011).

**Particle soot absorption photometer.** The Radiance Research (Model PSAP) particle soot absorption photometer (PSAP) is a filter-based instrument that can measure the in situ aerosol absorption coefficient ( $\sigma_{ap}$ ) at 1 minute intervals in real time (Bond et al. 1999; Anderson et al. 1999; Bond et al. 2005; Virkkula et al. 2005; Virkkula 2010). The PSAP utilizes slightly different wavelengths (470, 528, and 660 nm) than the nephelometer. The  $\sigma_{ap}$  retrievals are calibrated and quality assured as reported in the Bond et al. (1999), Anderson et al. (1999), and Virkkula et al. (2010) studies. The hourly averaged nephelometer and PSAP measurements of  $\sigma_{sp}$  and  $\sigma_{ap}$  at 450 nm and 470 nm, respectively (e.g., Corrigan et al. 2006) are used to calculate the single scattering co-albedo parameter,  $\omega_{obs}$ , by the following equation

$$\omega_{obs} = \sigma_{ap} / (\sigma_{sp} + \sigma_{ap}). \quad (6)$$

### **Atmospheric Radiation Measurement Mobile Facility**

The Atmospheric Radiation Measurement (ARM) mobile facility in the Azores (AMF-Azores) was operational for a 19-month period during the Clouds, Aerosol, and Precipitation in the Marine Boundary Layer (CAP-MBL) campaign (Rémillard et al. 2012; Dong et al. 2014; Wood et al. 2014). The Azores is a collection of islands located in the eastern remote Atlantic Ocean where marine boundary layer (MBL) clouds (e.g., shallow cumulus, stratocumulus, and stratus) are present throughout the year due to semi-permanent weather patterns (Rémillard et al. 2012; Dong et al. 2014; Wood et al. 2014). This region is also influenced by mid-latitude, tropical, and extratropical cyclones. As a

result, aerosols from North and Central America, Africa, and the surrounding ocean observed passing over this area can provide a great opportunity to investigate the AIE on MBL clouds (Figure 6) (Osborne and Haywood 2005; Fiahlo et al. 2005; Owen et al. 2006; Val Martin et al. 2006; Rémillard et al. 2012; Wood et al. 2014).

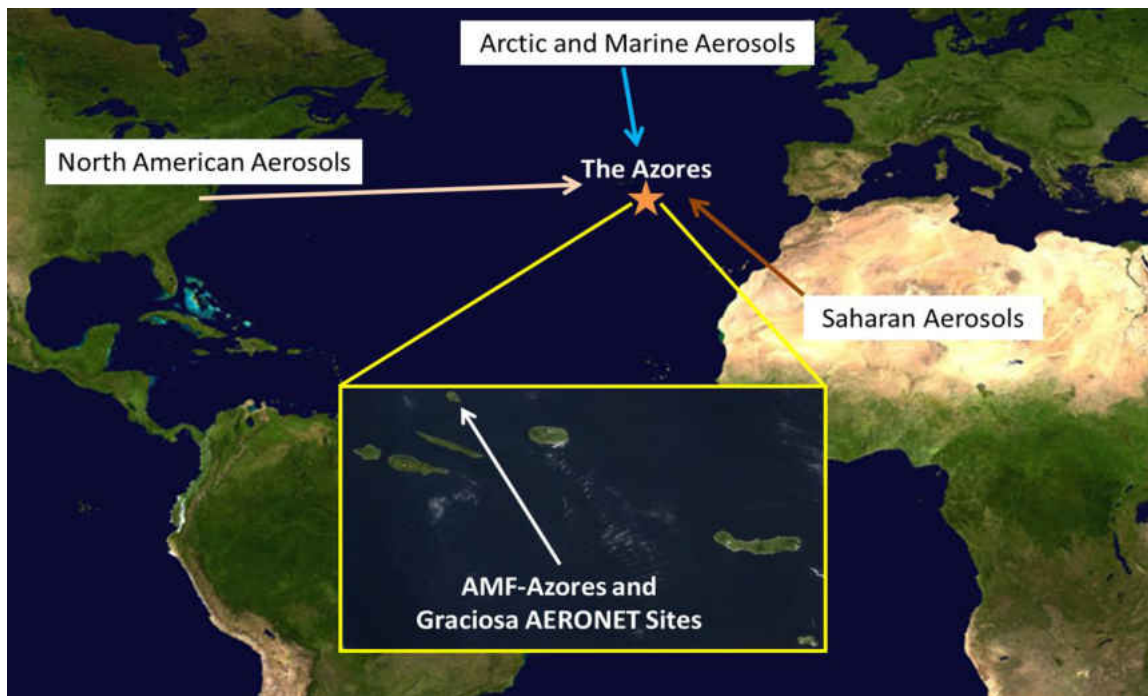


Figure 6. The AMF-Azores and Graciosa AERONET sites used during the Clouds, Aerosol, and Precipitation in the Marine Boundary Layer (CAP-MBL) campaign are located on Graciosa Island. The Azores is typically dominated by clean air masses but with periodic episodes of polluted air masses from North America, Europe, and the Saharan desert. Large image is provided by NASA World Wind software (<http://worldwind.arc.nasa.gov/index.html>) and the smaller inset image is provided by NASA Worldview EOSDIS (<https://earthdata.nasa.gov/labs/worldview/>).

The AMF-Azores site continuously sampled cloud, precipitation, and aerosol properties during this period. This site has an AERONET facility (Graciosa site: 39.1°N, 28.03°W) in addition to a TSI-3563 nephelometer, Radiance Model PSAP, and an optical particle counter that measures cloud condensation nuclei.

Aerosols that are advected over the Azores have varying abilities to activate as CCN. This study uses in situ measurements from a single-column Data Management

Team (DMT) Model 1 counter at seven supersaturations (Jefferson 2011). The  $N_{CCN}$  for this study was calculated using hourly-averaged measurements from an optical particle counter at 0.2% supersaturation (Jefferson 2010; Wood et al. 2014). Note that since  $N_{CCN}$  increases with increasing supersaturation (e.g., Hudson and Noble 2013; Wood et al. 2014),  $N_{CCN}$  at 0.2% supersaturation is used in this dissertation in a similar manner to the Dong et al. (2014) and Logan et al. (2014) studies.

### **CALIPSO Satellite Observations**

The Cloud-Aerosol Lidar and Infrared Pathfinder Satellite Observations (CALIPSO) platform became operational in June 2006 as part of the NASA A-Train constellation of satellites (Winker et al. 2007). This satellite, which orbits at an altitude of 705 km in a polar orbit, carries several sensors designed to retrieve cloud and aerosol properties. One of the sensors, the Cloud-Aerosol Lidar with Orthogonal Polarization (CALIOP), is a nadir-pointing dual-wavelength polarization-sensitive lidar that operates at 532 and 1064 nm to provide vertical profiles of aerosols and clouds (Winker et al. 2007).

CALIPSO is used in a similar manner as the DIAL in identifying the altitudes of various aerosol layers. In addition, products from the CALIPSO Vertical Feature Mask (VFM; Version 3) are used to provide vertical profiles of 532 nm total attenuated backscatter, 1064 nm attenuated backscatter, and depolarization ratio. The cloud and aerosol mask provided by the VFM, which identifies clear air, cloud type, and aerosol type (Liu 2005), offers a horizontal resolution of 333 m, with a vertical resolution of 30 m below 8.2 km and 60 m above (Winker et al. 2007). Fine grid spacing and high sensitivity allow CALIOP to detect aerosol layers and optically thin clouds. However,

the lidar signals are attenuated by optically thick clouds (Kato et al. 2010), which affects retrievals of cloud and aerosol layers beneath the level of attenuation (Figure 7).

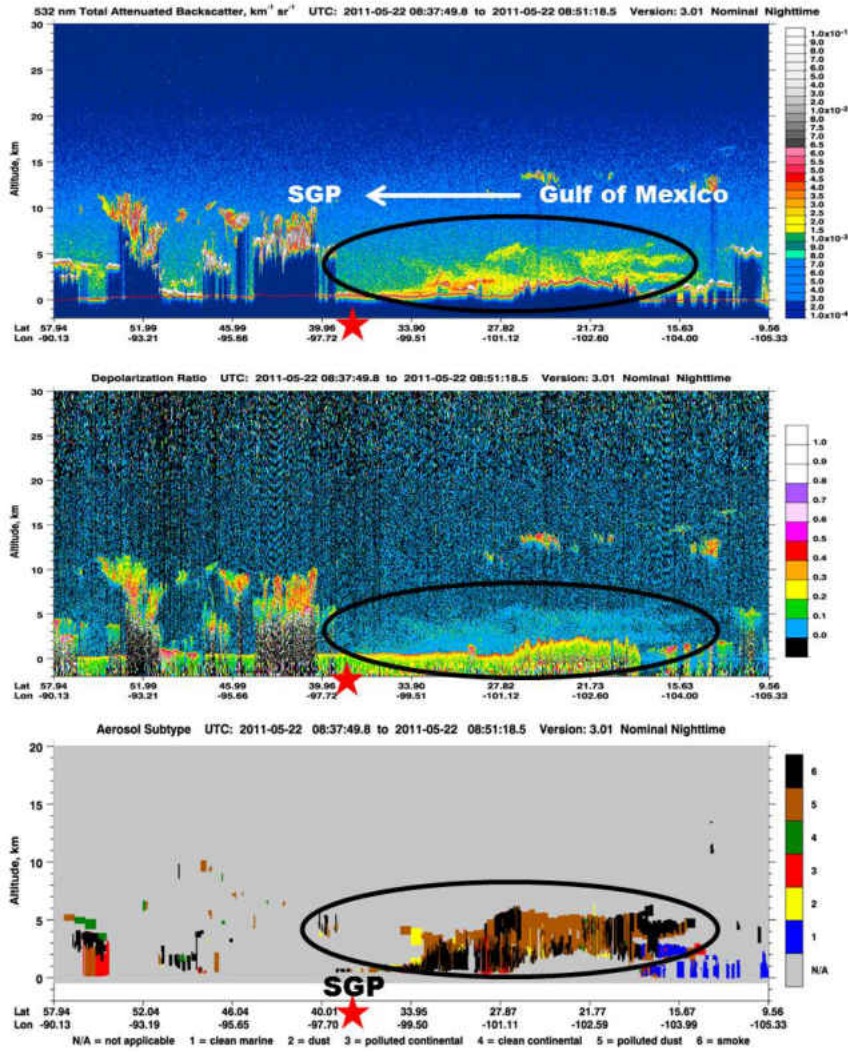


Figure 7. Example of a biomass burning smoke plume captured over the Atmospheric Radiation Measurement-Southern Great Plains (ARM-SGP) facility as observed by CALIPSO. Curtain plots of (a) 532 nm backscatter, (b) depolarization ratio, and (c) vertical feature mask (VFM) of a biomass burning smoke plume (black pixels) spanning the Gulf of Mexico to the ARM-SGP facility. Signal attenuation can be seen in the cloud layers (red or grey) around 10 km while aerosol layers (yellow) do not attenuate. Smoke is often misidentified as polluted dust in the VFM due to similarities in absorptive properties between the aerosol types (Kim et al. 2013).

## MODIS Satellite Observations

The Moderate Resolution Imaging Spectrometer (MODIS) platform is onboard the Terra and Aqua satellites and their products are used in this dissertation to investigate the spatial and temporal coverage of aerosol events. For example, Figure 8 shows a MODIS-Terra image of the biomass smoke plume observed by CALIPSO in Figure 7. MODIS-Terra crosses the Equator from north to south in the morning (1030 UTC) while MODIS-Aqua crosses the Equator from south to north in the afternoon (1330 UTC) and is part of the A-Train constellation of satellites which includes CALIPSO. Both satellite platforms can yield full global coverage within two days. The satellite datasets used in this study are the Terra Edition2B and Aqua Edition1B Clouds and the Earth's Radiant Energy System (CERES) Single Scanner Footprint (SSF) products and include the "Rev1" calibration adjustment to the CERES shortwave (SW) record to account for optics contamination during the first few years on orbit (Matthews et al. 2005). The CERES instruments on the Terra and Aqua satellites measure radiances that are converted to broadband fluxes using Angular Distribution Models (ADMs) sampled and optimized for each satellite orbit. Estimated uncertainties in the solar-reflected ( $SW_{\text{toa}}^{\uparrow}$ ) single field-of-view instantaneous radiative fluxes at TOA are  $13 \text{ W m}^{-2}$  (Chambers et al. 2002; Loeb et al. 2003). The SSF combines the CERES broadband flux measurements at a 20 km resolution with coincident, sub-sampled 1 km MODIS cloud and aerosol retrievals (Wielicki et al. 1996; Ignatov et al. 2005). These datasets include the MODIS-retrieved visible (550 nm) AOD (MOD04 on Terra; MYD04 on Aqua) and CERES-derived TOA albedo. The MOD04 product uses sophisticated cloud screening and aerosol retrieval algorithms developed by the MODIS cloud and aerosol groups with

uncertainties of  $0.03 \pm 0.05$  AOD over ocean and  $0.05 \pm 0.15$  AOD over land (Tanré et al. 1997; Ackerman et al. 1998; Martins et al. 2002; Remer et al. 2005).

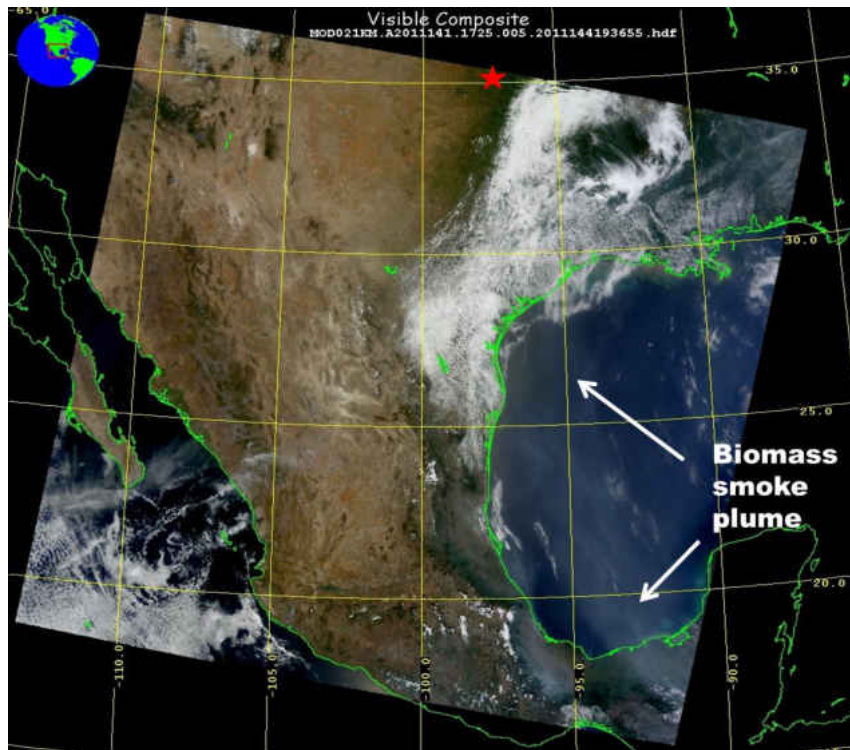


Figure 8. Moderate Resolution Imaging Spectroradiometer (MODIS) Terra image of the biomass smoke plume from Fig. 7 that spanned the Gulf of Mexico and was observed by the ARM-SGP facility (red star).

### Dissertation Study Regions

The locations of the selected AERONET sites used in this dissertation are shown in Figure 9. Four sites (red rectangles) representing single aerosol mode regions include: NASA Goddard ( $38.99^{\circ}\text{N}$ ,  $76.84^{\circ}\text{W}$ ), Mexico City ( $19.34^{\circ}\text{N}$ ,  $99.18^{\circ}\text{W}$ ), Alta Floresta ( $9.87^{\circ}\text{S}$ ,  $56.10^{\circ}\text{W}$ ), and Solar Village ( $24.91^{\circ}\text{N}$ ,  $46.40^{\circ}\text{E}$ ). The sites representing complex aerosol source regions in Asia include: Xianghe ( $39.75^{\circ}\text{N}$ ,  $116.96^{\circ}\text{E}$ ), Taihu ( $31.4^{\circ}\text{N}$ ,  $120.21^{\circ}\text{E}$ ), and SACOL ( $35.95^{\circ}\text{N}$ ,  $104.14^{\circ}\text{E}$ ) in China, and Mukdahan, Thailand ( $16.61^{\circ}\text{N}$ ,  $104.68^{\circ}\text{E}$ ). Xianghe is located in a mixture region that is influenced by

pollution, biomass burning and mineral dust particles (Eck et al. 2005; Eck et al. 2010; Logan et al. 2010).

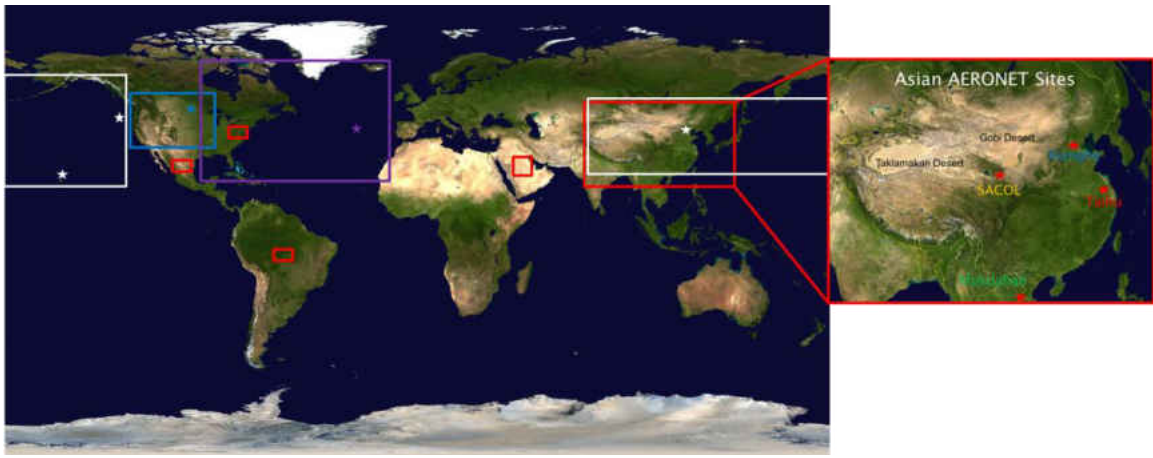


Figure 9. Combination of AERONET sites (stars) and study regions (boxes) for Asian aerosol properties and transport (white and red), North American aerosol properties and transport (blue), and aerosol impacts on marine CCN.

Taihu is located in a region heavily influenced by airflow from large urban centers (e.g., Shanghai and Hangzhou) and industry in each cardinal direction and to a lesser extent, the influences of the Gobi and Taklamakan Deserts (Xin et al. 2007). SACOL, the Semi-Arid Climate and Environment Observatory of Lanzhou University, is situated in central China (Gansu province) within the reaches of the Loess Plateau (downwind of Gobi and Taklamakan Deserts) (Xin et al. 2007; Huang et al. 2008b). The site is just southeast of Lanzhou City, a large metropolitan and industrial center (~3.5 million inhabitants). Mukdahan is located in extreme eastern Thailand near the Laotian border where wildfires as well as fires from crop and vegetation burning are prominent during the dry season (September-May) (Gautam et al. 2012).

### **CHAPTER III**

#### **THEORETICAL DATABASE COMPARISON STUDY**

Asian dust events typically occur during the spring season but have been known to occur at any time of the year (Tsunematsu et al. 2005; Li et al. 2007a,b; Logan et al. 2010). Strong low pressure systems that create dry convection facilitate favorable conditions for surface winds to loft loose desert sand and soil into the mid-troposphere (~ 5 km or 500 hPa level) where it can be transported for thousands of kilometers (Uematsu et al. 1983; Jordan et al. 2003; Li et al. 2007b; Logan et al. 2010; Ling et al. 2011). Continuing urbanization and industrialization in Asia causes concern since anthropogenic carbonaceous particles such as black carbon (BC), organic carbon (OC), and biomass burning aerosols along with sulfates and nitrates have been known to mix and condense onto mineral dust, thus altering the optical properties of the particles (Yao et al. 2002; Jordan et al. 2003; Sun et al. 2005; Logan et al. 2013a). Due to the variety of scattering and absorbing aerosols generated as a result of these secondary reactions, the radiative balance of the atmosphere is altered by the aforementioned first aerosol effect while the second aerosol effect deals with influences on cloud physical properties (e.g. lifetime, brightness, droplet size distribution, and precipitation) (Li et al. 2007a; Rosenfeld et al. 2008; Li et al. 2011). Aerosol effects can also be locally detrimental as they create increased health risks especially for susceptible populations (Pope 2004).

Two Asian dust events during the winter (24-31 December 2007) and spring (15-21 March 2010) seasons provide a unique opportunity to compare the seasonal and

regional dependences of mineral dust absorptive properties. Both dust events passed over the same regions in northern, west-central, and eastern China before they exited the mainland, subsequently affecting the remote Pacific Ocean before dissipating (MODIS visible images not shown). However, the aerosol types in these regions have shown a diverse seasonal dependence (Sun et al. 2005; Wang et al. 2010; Logan et al. 2013a). For example, northern China usually has strongly absorbing aerosols in the winter due to BC and OC particle emissions from industrial and urban emissions (e.g. residential heating) while the spring season is dominated by emissions from the Gobi desert upwind of the area (Eck et al. 2005; Xin et al. 2007).

This study uses the parameters of volume size distribution ( $dV/d\ln R$ ), aerosol optical depth (AOD), absorption aerosol optical depth (AAOD), their respective spectral dependences: Angström exponent ( $AE_{AOD}$ ) and absorption Angström exponent ( $AAE_{AOD}$ ), and the spectral single scattering albedo,  $[\omega_o(\lambda)]$ . The  $dV/d\ln R$  parameter illustrates the relative contributions of fine and coarse mode aerosols. The AOD, AAOD,  $AE_{AOD}$ , and  $AAE_{AOD}$  parameters will illustrate the seasonal differences of the absorptive properties of the mineral dust that may be mixed with anthropogenic carbonaceous particles. Lastly, the single scattering properties from three selected ground-based Asian AERONET sites (SACOL, Xianghe, and Taihu) are compared to theoretically calculated ones from a mineral dust model.

### **Theoretical Mineral Dust Model**

Mineral dust particles are typically non-spherical in nature. In fact, their optical properties require special consideration since AERONET retrievals are primarily based on assumptions that atmospheric aerosols are homogeneous spherical particles

(Ackerman and Toon 1981; Dubovik et al. 2000; Meng et al. 2010). As pointed out by Dubovik et al. (2000), though there are shortcomings to using these assumptions in AERONET retrievals, it is still possible to gain useful information from the almucantar readings (Dubovik et al. 2000; Dubovik et al. 2006). This study employs the use of a mineral dust model that is comprised of a spectral database calculated from mathematical and geometric theory (Meng et al. 2010; Yi et al. 2011). The model contains theoretical calculations of the single scattering parameters of mineral dust aerosols by assuming a tri-axial ellipsoidal geometric shape which offers many advantages over calculations based on a combination of spherical (Mie Theory) and spheroidal particle shape assumptions (Meng et al. 2010; Yi et al. 2011).

The Meng et al. (2010) model uses a combination of Lorenz-Mie theory, the T-matrix method, discrete dipole approximation (DDA), and an improved geometric optics method (IGOM) to illustrate the optical properties of mineral dust-like aerosols. The results are compiled into a database that requires the knowledge of the particle aspect ratio (ratio of the semi-major to semi-minor axis assuming ellipsoidal geometry), size parameter (based on retrieved effective radius), and complex index of refraction. A more detailed discussion of the database as well as the methodology can be found in (Meng et al. 2010). The database contains information about aerosol extinction efficiency ( $Q_{\text{ext}}$ ), extinction ( $\sigma_{\text{ext}}$ ), scattering ( $\sigma_{\text{sp}}$ ) and absorption ( $\sigma_{\text{ap}}$ ) coefficients, and spectral single scattering albedo [ $\omega_0(\lambda)$ ].

We will consider the AERONET retrievals as truth and compare these retrievals with the theoretical calculations from the mineral dust model because the model will have inherent shortcomings when dealing with aerosol mixtures (e.g., external/internal

mixtures and pollution coating). Since AERONET retrievals are based on spheroidal assumptions (rather than ellipsoidal) it would be informative to investigate the agreement between the two retrieval mechanisms for validation purposes. This will be done by performing a comparison study using the AERONET retrieved effective radius and complex index of refraction ( $m_r + m_i$ ) as inputs of the mineral dust model.

### **Methodology**

The theoretical database is arranged in the following manner: two aspect ratios, one size parameter, and the complex index of refraction (real and imaginary parts) (Meng et al. 2010). The complex index of refraction is obtained directly from the AERONET retrievals with an uncertainty of up to 30% when  $AOD_{440} > 0.5$  (Dubovik et al. 2000). The size parameter ( $x$ ) at each wavelength ( $\lambda$ ) is calculated from the AERONET retrieved effective radius ( $r_e$ ) and is given by,

$$x = \frac{2\pi r_e}{\lambda}, \quad (7)$$

where  $\lambda$  is in discrete wavelengths of 440, 675, 870, and 1020 nm. In this way, a single value of  $\omega_0$  at each wavelength is obtained from the database to yield a theoretical spectral dependence to go along with the AERONET retrieved spectral dependence. The aspect ratios are assumed based on the best fit between the theoretical and observational  $\omega_0$  spectral dependence curve to within one standard deviation. We vary the effective radius and complex index of refraction while keeping one of these parameters constant in order to perform the comparison study.

### **Meteorological Conditions**

Figures 10a and 10b show the 850 hPa geopotential heights for the 24-31 December 2007 (winter case) and 15-21 March 2010 (spring case) time spans. The mean

synoptic patterns of both cases have similar trough (darker purple) locations over Northeastern China. However, the ridge (red and orange) locations differ by ten degrees of latitude with the winter case ridge position ( $43^{\circ}\text{N}$ ) being at a higher latitude than the spring case ( $33^{\circ}\text{N}$ ). The position of the ridge in relation to the trough is also different between the two cases suggesting different wind flow patterns (Sun et al. 2001; Sun et al. 2005). For example, there is more of a northwesterly flow over Xianghe than at Taihu and SACOL in the winter case but a west-northwesterly flow pattern is evident in the spring case at all three sites. From backward trajectory analysis (not shown) both storms had origins in the Loess Plateau (Western Gobi Desert) region but the wind patterns suggest that the dust from the eastern Gobi Desert may have impacted Xianghe more than SACOL and Taihu for the winter case. In contrast, the spring case wind pattern and subsequent track of the low pressure system advected dust from the Loess Plateau to all sites. The synoptic patterns for both cases illustrate how the absorptive properties of the mineral dust aerosols can change depending on the season which is discussed in the following section.

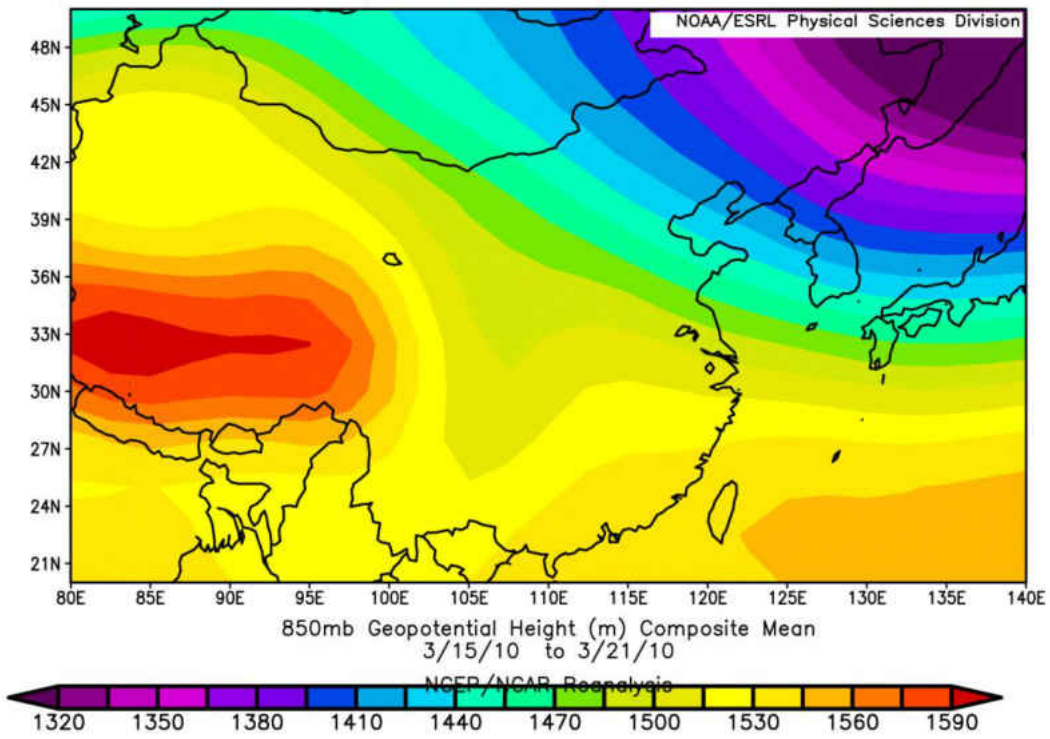
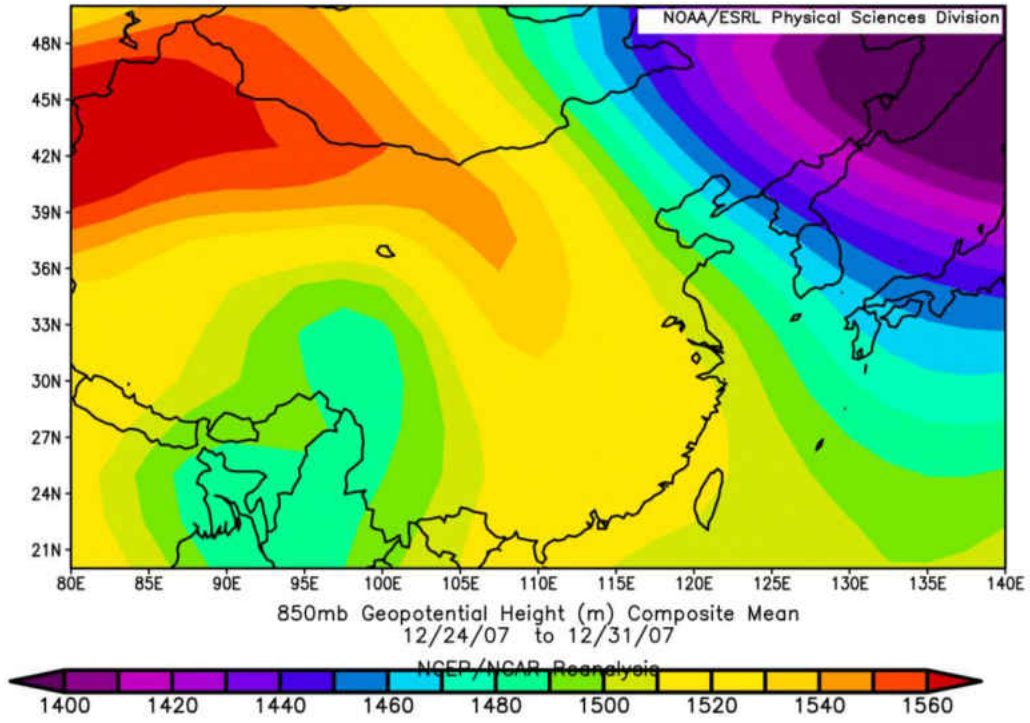


Figure 10. (a) 850 hPa geopotential heights showing the low pressure (purple) and high pressure systems (orange) and the inferred wind patterns as a result of their positions for

the winter and (b) spring cases. Image provided by the NOAA/ESRL Physical Sciences Division, Boulder Colorado from their Web site at <http://www.esrl.noaa.gov/psd/>.

### **Mineral Dust Properties Inferred From the Particle Volume Size Distribution, AOD, AAOD, AE<sub>AOD</sub>, and AAE<sub>AOD</sub> Parameters**

Figures 11a and 11b show the volume size distributions of the winter and spring cases, respectively. Since the amount of aerosol loading (AOD) exceeds 0.4 in all instances, the errors in  $dV/d\ln R$  retrievals are small ( $< 10\%$ ) (Dubovik et al. 2000; Dubovik et al. 2002). For the winter case, SACOL and Xianghe have similar bimodal distributions dominated by the coarse mode with weak fine mode contributions. There is a small fine mode contribution ( $r_{e-fine} \sim 0.085 \mu\text{m}$ ) at SACOL indicating pollution from the nearby city of Lanzhou (Xin et al. 2007). There is a smaller, yet discernible fine mode contribution at Xianghe ( $r_{e-fine} \sim 0.15$ ) which indicates anthropogenic influences from Beijing and surrounding areas (Eck et al. 2005). The coarse mode magnitude at Taihu is nearly half compared to the other sites but the fine mode contribution ( $r_{e-fine} \sim 0.45$ ) is likely due to industrial influences in the vicinity as well as urban influences from Shanghai (Yao et al. 2002). The spring case exhibits a strong mineral dust signature at all three sites as there is a more pronounced unimodal coarse mode contribution. The lack of a discernible fine mode peak suggests that mineral dust dominates the size distribution in this case though pollution particles may still be present in the atmosphere.

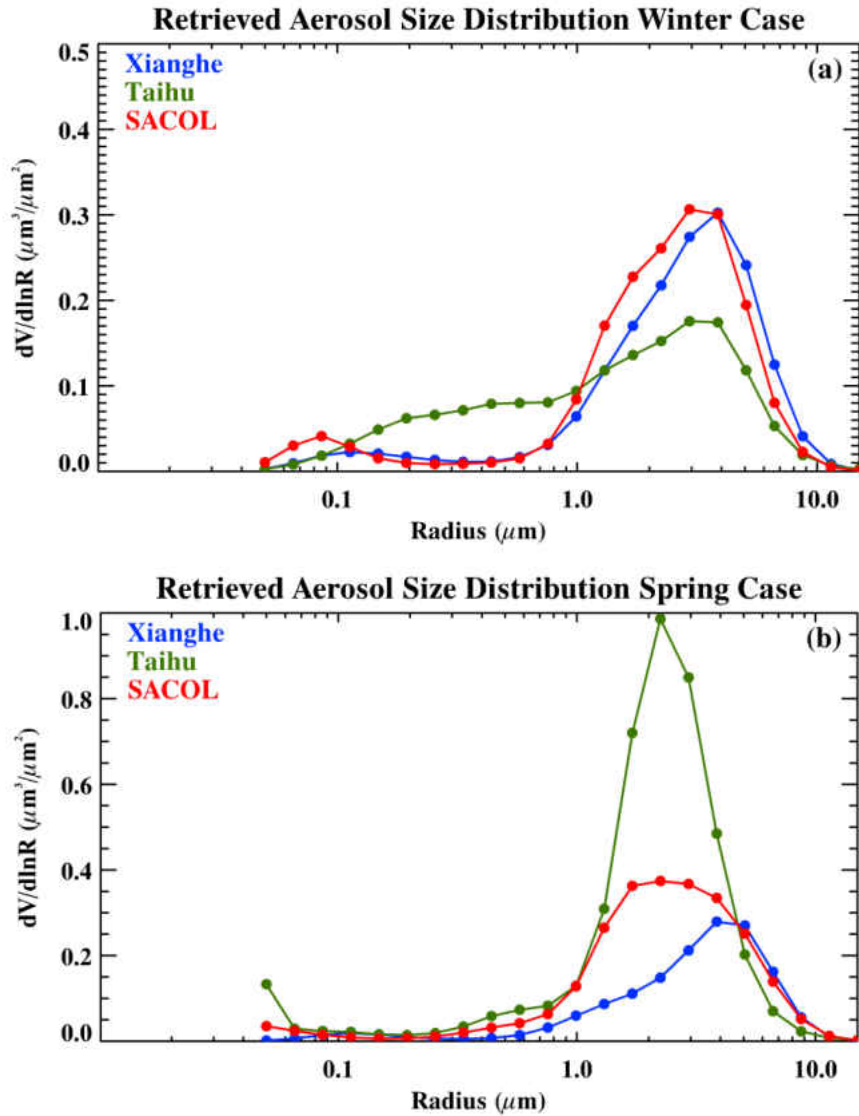


Figure 11. Particle volume size distributions of the (a) winter and (b) spring cases.

The spectral dependences of AOD for the winter and spring cases are shown in Figure 12. SACOL has the spectral dependence of all three sites for both the winter and spring cases indicating coarse mode particles ( $AE_{AOD}$  of 0.29 and 0.11, respectively). This is due to a close proximity to various mineral dust source regions (Taklamakan and Gobi Desert and the Loess Plateau) (Ling et al. 2011; Wang et al. 2010). However, the spectral dependence for the winter case is stronger suggesting a noticeable more of a fine

mode influence than in the spring case. At Xianghe, the stronger spectral dependence and higher  $AE_{AOD}$  values (0.42-0.48) suggest more of a fine mode influence for both cases than at SACOL. Taihu has the strongest spectral dependence in the winter case with  $AE_{AOD}$  of 0.62 indicating a mixture of coarse and fine modes due to an abundance of pollution particles resulting from stagnant winter season air patterns that allow for increased aerosol loading ( $AOD_{440} \sim 1.3$ ) (Yang et al. 2009). In the spring, there is much less spectral dependence at Taihu suggesting coarse mode particles dominate the aerosol extinctive properties similar to the SACOL case. It is interesting to note that the  $AE_{AOD}$  value of 0.15 at Taihu illustrates the overwhelmingly large magnitude of dust particles in the spring as compared with the winter case. Since all sites have  $AE_{AOD}$  values less than 0.62, it can be concluded that coarse mode particles dominated the aerosol size properties along with some influences from the fine mode (e.g., pollution).

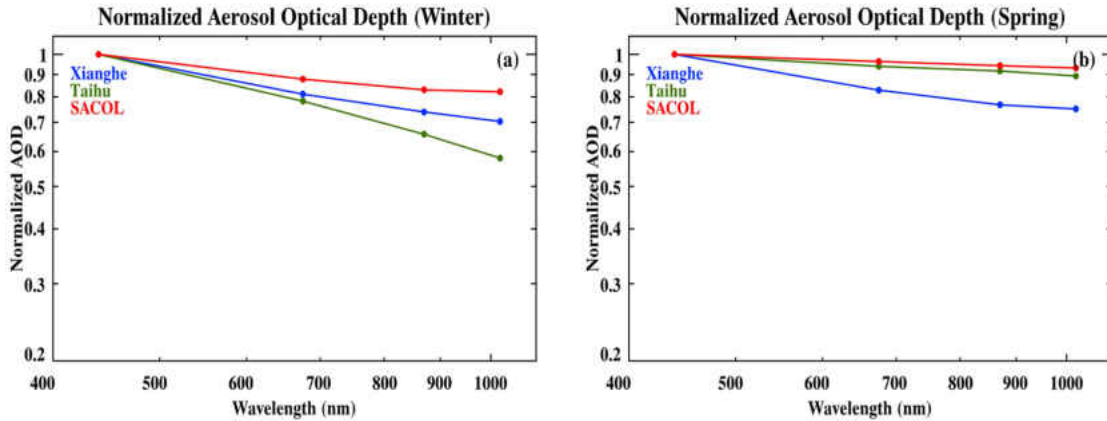


Figure 12. Spectral dependence of AOD for the (a) winter and (b) spring cases. The normalized AOD values at each wavelength are ratios to the  $AOD_{440}$  value in order to compare the spectral dependences across the three sites.

Figure 13 shows the spectral dependence of AAOD. The spectral dependence is slightly stronger for the winter case than for the spring case. The winter  $AAE_{AOD}$  value of 1.8 represents a typical value for dust due to the strong absorption in the visible and weak

absorption in the near IR wavelength (Yang et al. 2009), while the spring  $AAE_{AOD}$  value of 1.6 indicates a mineral dust influence with possible carbonaceous influences (Xin et al. 2007; Yang et al. 2009). For the winter cases, Taihu has a weaker spectral dependence than Xianghe and nearly identical to SACOL. The lower  $AAE_{AOD}$  of 1.3 indicates a strong BC influence given by a weaker spectral dependence across the visible and near IR. It should be noted that OC tends to strengthen the absorption in the visible leading to an even higher  $AAE_{AOD}$  value. For the spring case, Taihu has the strongest spectral dependence in both the visible and near IR indicating a robust mineral dust influence ( $AAE_{AOD} \sim 2.5$ ) (Bergstrom et al. 2007). The spring case at SACOL is more indicative of mineral dust influences with  $AAE_{AOD}$  of 1.7. Table 1 summarizes the AERONET retrieved parameters used in this study. The following section will discuss how well the theoretically calculated  $\omega_o(\lambda)$  at different wavelengths agree with AERONET retrievals at the three sites for the selected two cases.

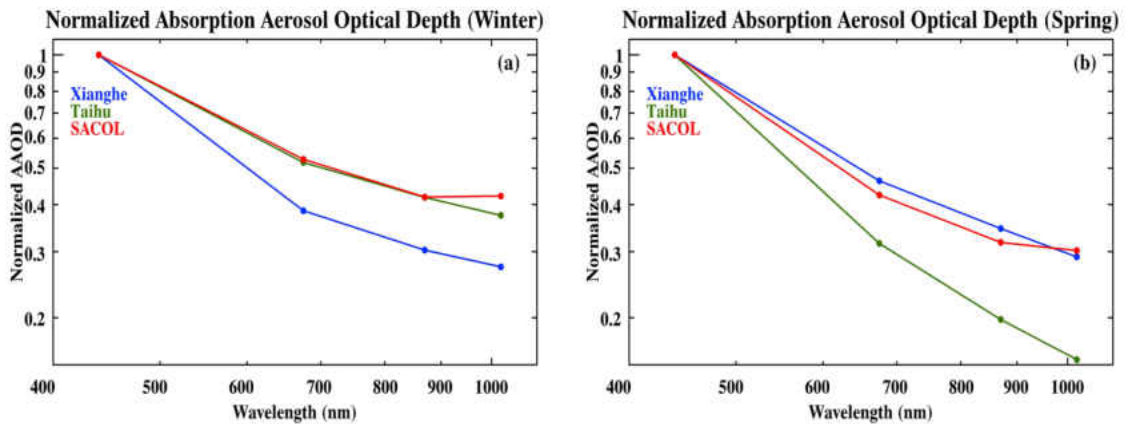


Figure 13. Same as Fig. 12 but for AAOD.

Table 1. Summary of the AERONET retrieved aerosol optical properties for the winter and spring cases.

<b>AERONET Site</b>	<b>AOD<sub>440</sub></b>	<b>AE<sub>AOD</sub></b>	<b>AAE<sub>AOD</sub></b>	<b>m<sub>r</sub></b>	<b>m<sub>i</sub></b>	<b>r<sub>eff</sub></b>
SACOL (winter)	0.6	0.29	1.3	1.46	0.003	0.77
SACOL (spring)	0.8	0.11	1.7	1.57	0.004	0.97
Xianghe (winter)	0.6	0.48	1.8	1.60	0.005	1.07
Xianghe (spring)	0.5	0.42	1.6	1.60	0.004	1.25
Taihu (winter)	1.3	0.62	1.3	1.53	0.022	0.59
Taihu (spring)	1.4	0.15	2.5	1.53	0.004	0.80

Table 2. Summary of the theoretical model parameters used in this study.

	<b>Aspect Ratio</b>	<b><math>m_r</math></b>	<b><math>m_i</math></b>	<b><math>r_{eff}</math> (<math>\mu m</math>)</b>
SACOL (Winter Case)	1.5:1.8	1.50	0.005	0.7
		1.50	0.005	0.8
		1.50	0.005	0.9
		1.50	0.005	1.0
SACOL (Spring Case)	1.5:1.8	1.60	0.005	0.7
		1.60	0.005	0.8
		1.60	0.005	0.9
		1.60	0.005	1.0
SACOL (Winter Case)	1.5:1.8	1.40	0.001	0.8
		1.40	0.005	0.8
		1.40	0.010	0.8
		1.50	0.001	0.8
		1.50	0.005	0.8
		1.50	0.010	0.8
		1.60	0.001	0.8
		1.60	0.005	0.8
SACOL (Spring Case)	1.5:1.8	1.40	0.001	1.0
		1.40	0.005	1.0
		1.40	0.010	1.0
		1.50	0.001	1.0
		1.50	0.005	1.0
		1.50	0.010	1.0
		1.60	0.001	1.0
		1.60	0.005	1.0
		1.60	0.010	1.0

Table 2. cont.

		1.60	0.005	1.0
Xianghe (Both Cases)	1.8:2.1	1.60	0.005	1.1
		1.60	0.005	1.2
		1.60	0.005	1.3
		1.60	0.001	1.0
Xianghe (Both Cases)	1.8:2.1	1.60	0.005	1.0
		1.60	0.010	1.0
		1.50	0.020	0.5
Taihu (Winter Case)	1.5:1.8	1.50	0.020	0.6
		1.50	0.020	0.7
		1.50	0.020	0.8
		1.50	0.020	0.9
		1.50	0.005	0.5
Taihu (Spring Case)	1.2:1.5	1.50	0.005	0.6
		1.50	0.005	0.7
		1.50	0.005	0.8
		1.50	0.005	0.9
		1.50	0.010	0.6
Taihu (Winter Case)	1.5:1.8	1.50	0.020	0.6
		1.50	0.050	0.6
		1.50	0.001	0.8
Taihu (Spring Case)	1.2:1.5	1.50	0.005	0.8
		1.50	0.010	0.8

### Comparisons of $\omega_o(\lambda)$ Between Theoretical Calculations and AERONET Retrievals

Figures 14 and 15 present the comparisons of  $\omega_o(\lambda)$  values at wavelengths of 440-1020 nm retrieved from three AERONET sites to those calculated by the mineral dust model for the winter and spring cases. The size parameter in Eq. (7) is calculated from the AERONET retrieved effective radius for each wavelength. Each size parameter corresponds to a set of  $\omega_o(\lambda)$  values that are input into a matrix contained in the theoretical database. It should be noted that the database itself contains nearly 3200 files that are categorized by aspect ratio (1:1-3:3) and complex index of refraction (1.1-2.1 +

0.005-0.5). In order to demonstrate the spectral dependences of  $\omega_o$  to the index of refraction and aerosol particle size, the index of refraction is held constant while the effective radius varies in Figure 14 and vice versa in Figure 15. Although the model results are summarized in Table 2, we focus on the following key discussion points at the SACOL, Xianghe and Taihu sites.

At the SACOL site, the model calculated  $\omega_o(\lambda)$  agrees well with AERONET retrievals in the visible but overestimates in the longer wavelengths for the winter case (red) (Figure 14a). The spring case has slightly better agreement in the longer wavelengths (675 and 870 nm) but poor agreement otherwise. A possible explanation is due to the fact that two different real indices of refraction ( $m_r$  of 1.46 and 1.57 for winter and spring, respectively) are used which decreases the sensitivity of the modeled results because the optical properties of aerosol mixtures are poorly taken into account using these criteria. The Xianghe site has nearly the same indices of refraction for both the winter and spring cases with only one theoretical calculation (Figure 14b) where the model calculation and observation agree to within one standard deviation suggesting more sensitivity of a variable effective radius. This is likely due the aerosols having similar optical properties during both dust events (i.e., similar source regions and carbonaceous influences).

At Taihu, there is seldom any agreement between theory and observation for the winter case suggesting that using a fixed  $m_i$  cannot account for the enhanced absorption from the large amount of carbonaceous aerosols present in this region (Figure 14c). In contrast, the spring case shows good agreement especially in the near IR due to the strong mineral dust influence that dominates the aerosol absorptive properties during this

episode. It is interesting to note that the stronger absorption in the winter case has  $m_i$  of nearly five times higher than the spring case (more absorbing pollution aerosols during winter season). In addition to varying the effective radius and holding the index of refraction constant, we now vary the index of refraction and hold the effective radius constant.

When we vary the index of refraction in the model calculations, it is obvious that there is better agreement between the calculations and observations. However, more variability is observed. This is especially evident at the SACOL and Taihu sites which exhibited different indices of refraction for the winter and spring cases (Figure 15). The calculated  $\omega_o(\lambda)$  values at SACOL are still higher than the observed ones for the winter case, however, they are within one standard deviation (Figure 15a). There is also better agreement in the spring case as well. The Xianghe winter and spring cases do not drastically change because there are no big differences in particle size and index of refraction between the two cases (Figure 15b). At the Taihu site, it is evident that varying the index of refraction better accounts for the wide variety of absorbing aerosols in a mineral dust/carbonaceous mixture in both the winter and spring cases (Figure 15c).

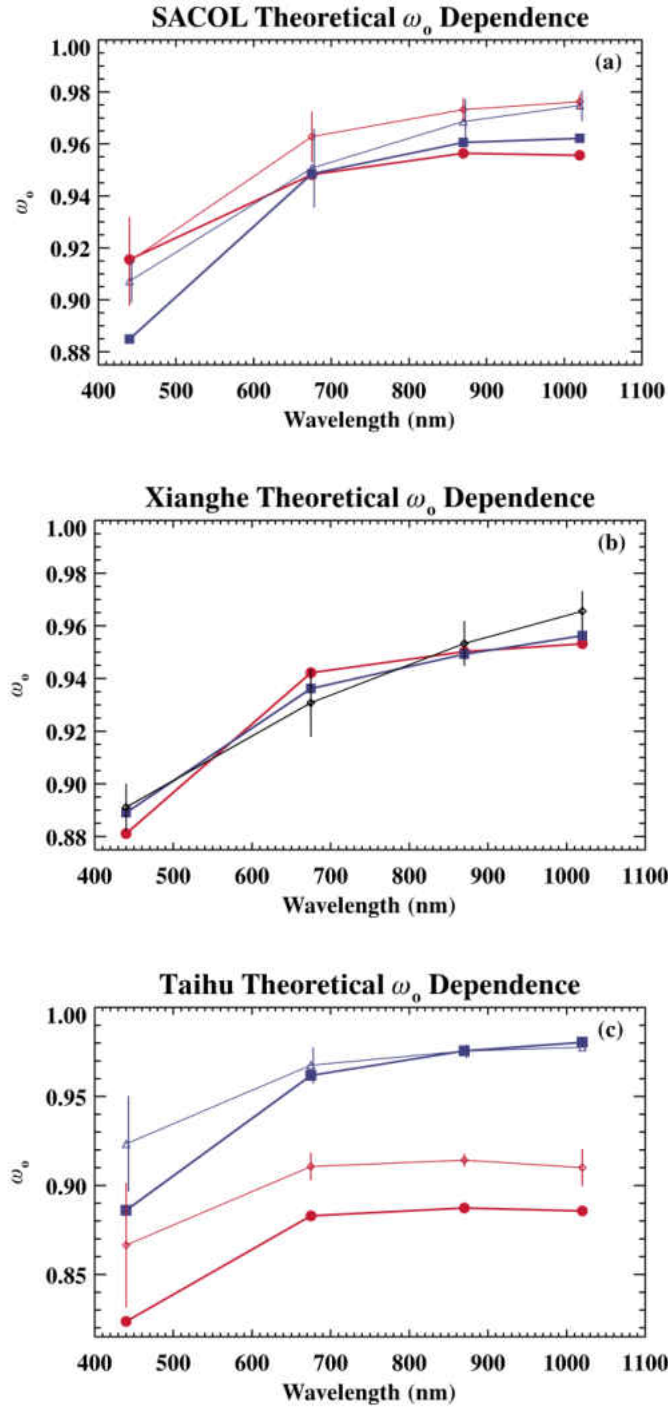


Figure 14. Comparison between the observed (solid) and theoretically calculated (dashed)  $\omega_0$  for the winter (red circle) and spring (blue box) cases at (a) SACOL, (b) Xianghe, and (c) Taihu. The measured complex index of refraction and the effective radii were used as inputs of the model calculation where the complex index of refraction is held constant while the effective radius varies. The vertical lines represent error bars of  $\pm 1\sigma$ .

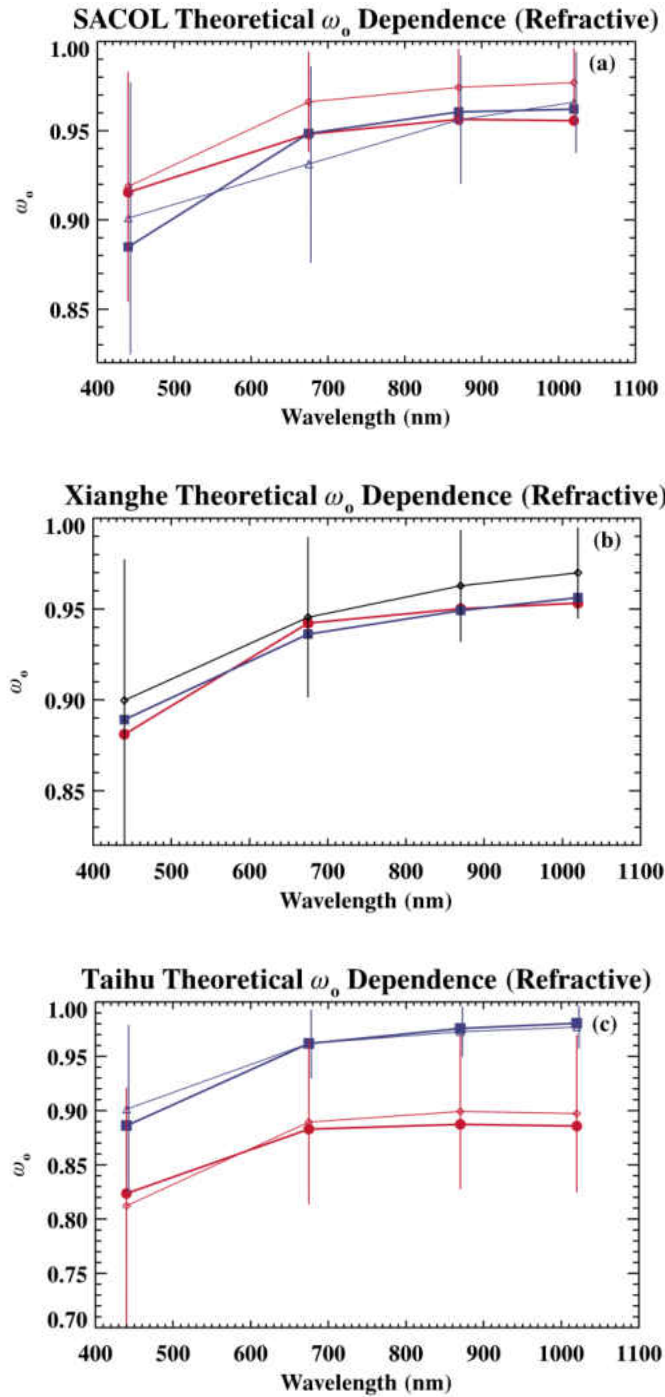


Figure 15. Same as Fig. 14 but in this case the effective radius is held constant while the index of refraction varies.

## Aerosol Radiative Effect

To quantitatively estimate the impact of the dust events on the surface and Top-Of-Atmosphere (TOA) radiation budgets, we use the method developed by Dubovik et al. (2006) to calculate shortwave (SW) aerosol radiative effects (ARE). It is defined as the difference between the net bottom and top of the atmosphere (BOA and TOA) fluxes when dust aerosols are present, ( $F_{\text{BOA}}^{\downarrow}$  and  $F_{\text{TOA}}^{\uparrow}$ ), and the nearby clean-sky daily SW fluxes ( $F_{\text{BOA}}^{\downarrow 0}$  and  $F_{\text{TOA}}^{\uparrow 0}$ ), and is given by

$$\Delta\text{ARE}_{\text{BOA}} = F_{\text{BOA}}^{\downarrow} - F_{\text{BOA}}^{\downarrow 0} \quad (8a)$$

and

$$\Delta\text{ARE}_{\text{TOA}} = F_{\text{TOA}}^{\uparrow} - F_{\text{TOA}}^{\uparrow 0}, \quad (8b)$$

respectively. This is a simulated product that uses a combination of sky radiance measurements and radiative transfer theory (Dubovik et al. 2000; Holben et al. 2006). The criteria for selecting the clean days are: (a)  $\text{AOD}_{440} \leq 0.3$  and (b) clean sky occurrence before and after the dust events. It should be noted here that clean sky conditions will typically have  $\text{AOD}_{440}$  values less than 0.05. However, there were no values that were less than 0.2 during the study period.

We note that there is a sharp increase in  $\Delta\text{ARE}$  during the dust events with  $\Delta\text{ARE}_{\text{BOA}} > \Delta\text{ARE}_{\text{TOA}}$ , which suggests a stronger aerosol cooling effect at the surface than at the TOA. The strongest ARE is observed at the Taihu site where the  $\Delta\text{ARE}$  values exceed  $-155 \pm 52 \text{ W m}^{-2}$  for the BOA and  $-60 \pm 15 \text{ W m}^{-2}$  for the TOA spring case. This is due to dust mixing with carbonaceous aerosols (local pollution) leading to an overall enhanced absorption (Ge et al. 2010). This is consistent with the Qiu et al.

(2013), Ge et al. (2010), and García et al. (2012) studies that used Shouxian ARM Mobile Facility (AMF), Zhangye AMF, and AERONET data, respectively.

Table 3. Summary of the AERONET calculated BOA and TOA aerosol radiative effect (ARE) values.

AERONET Site	BOA ARE Values ( $\text{W m}^{-2}$ )		
	<sup>a</sup> Clear Sky (before)	Dust Event	Clear Sky (after)
SACOL (winter)	-52.9	-101.1	-60.6
SACOL (spring)	-48.5	-136.7	-52.5
Xianghe (winter)	-64.2	-106.4	-39.8
Xianghe (spring)	-40.7	-83.0	-42.1
Taihu (winter)	-45.5	-177.3	-60.0
Taihu (spring)	-66.9	-155.3	-40.8
AERONET Site	TOA ARE Values ( $\text{W m}^{-2}$ )		
	Clear Sky (before)	Dust Event	Clear Sky (after)
SACOL (winter)	-17.0	-40.9	-13.1
SACOL (spring)	-4.5	-40.9	-8.5
Xianghe (winter)	-15.3	-46.0	-8.6
Xianghe (spring)	-17.1	-29.7	-9.1
Taihu (winter)	-19.0	-21.0	-17.2
Taihu (spring)	-27.3	-60.4	-26.5

<sup>a</sup> The clear-sky values were taken just before and after the dust event where  $\text{AOD}_{440} < 0.3$  and the ARE values for both clear-sky and dust events are calculated against the modeled fluxes without aerosol using Eq. 8. Note that the Taihu site has the highest mean clear-sky ARE due to persistent haze from numerous nearby urban and industrial influences (i.e. very few “clear day” instances).

The optical properties of mineral dust from two dust events are analyzed and compared to theoretical calculations in this section. For the winter case, the aerosol properties at SACOL, Xianghe, and Taihu are shown to be a mixture of carbonaceous particles (from local sources) and mineral dust as demonstrated by their  $AE_{AOD}$  values of 0.29, 0.48, and 0.62, respectively. In contrast, for the spring case their aerosol properties are primarily mineral dust dominant with  $AE_{AOD}$  of 0.11, 0.42, and 0.15, respectively. Carbonaceous particles are shown to influence the absorptive properties of the mineral dust in the winter case especially at SACOL and Taihu but less at Xianghe where the  $AAE_{AOD}$  values are 1.3, 1.3, and 1.8, respectively. During the spring, higher  $AAE_{AOD}$  values of 1.7 (SACOL) and 2.5 (Taihu) suggest that mineral dust dominates the absorptive properties of the aerosols. The lower  $AAE_{AOD}$  value of 1.6 at Xianghe indicates dust with some carbonaceous influences similar to SACOL and Taihu in the winter case.

A theoretical model based on geometric and mathematical calculations is used to compare with the AERONET retrieved aerosol parameters. The AERONET inversion algorithms employ a spheroidal particle shape assumption while the model assumes a tri-axial ellipsoidal shape. Though particle shape as well as size is important, the particle absorptive behavior should also be taken into account especially when mixtures of particle types are present. The winter cases at SACOL and Taihu show poor agreement between theory and observation when the effective radius is varied while holding the index of refraction constant. This is due to the wide variety of mineral dust and carbonaceous aerosols particles in the mixture that likely have different indices of

refraction. Xianghe has similar indices of refraction for both winter and spring cases leading to good agreement between model and observation results.

The spring cases exhibited better agreement than the winter cases because mineral dust was more dominant during the spring season at all three sites. Better agreement between theory and observation at all three sites is observed when the index of refraction is varied while holding the effective radius constant. This suggests the model is more sensitive to the particle absorptive properties rather than the size, especially when dealing with retrieving aerosol properties of mineral dust and carbonaceous particle mixtures. In light of these results it should be mentioned that when the index of refraction is held constant while the effective radius varies, there is less variability in the model than when the opposite is done. When aerosols have both similar size and composition (e.g. the Xianghe site) the model and observation results have sufficient agreement such that both scenarios can be used.

## CHAPTER IV

### METHODOLOGY

#### Aerosol Classification at Four Selected Single Mode Aerosol Dominated Sites

The Chung et al. (2012) study used spectral dependence of AERONET retrieved AOD and AAOD to partition aerosols according to type (e.g., pollution, mineral dust, and biomass burning) (Figure 16). They paid special attention to the role of carbonaceous aerosols and their inherent radiative forcing which is typically ignored in many climate models (Chung et al. 2012).

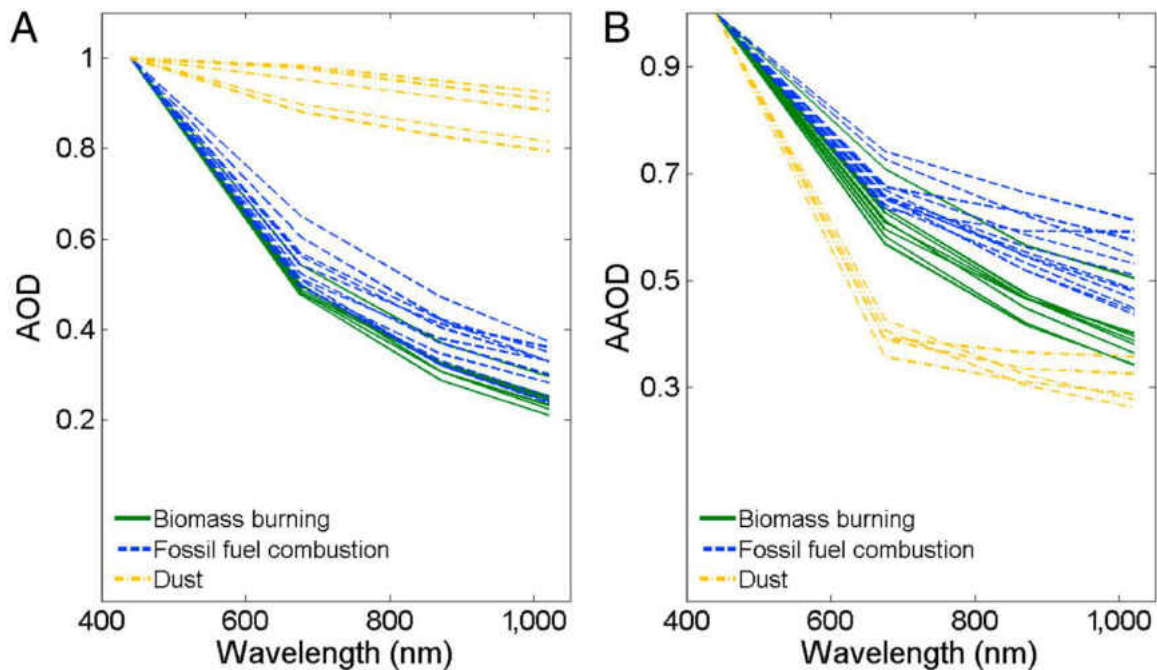


Figure 16. AERONET retrieved (a) AOD and (b) AAOD spectral dependences for single mode dominated sites from the Chung et al. (2012) study.

Asian aerosols are typically comprised of complex mixtures of these particles, therefore making it extremely difficult to study their behavior. Thus, it is necessary to investigate aerosol properties in regions dominated by single mode aerosol types since this will aid in serving as a baseline for analyzing the aerosol properties in Asia. The AERONET retrieved spectral dependences of AOD, AAOD, and  $\omega_{\text{obs}}$  (Figure 17) from four sites investigated in the Logan et al. (2013a) study reflect aerosol source regions dominated by weakly absorbing pollution [Mexico City (19.34°N, 99.18°W)], strongly absorbing mineral dust [Solar Village (24.91°N, 46.40°E)], and biomass burning particles [Alta Floresta (9.87°S, 56.10°W)].

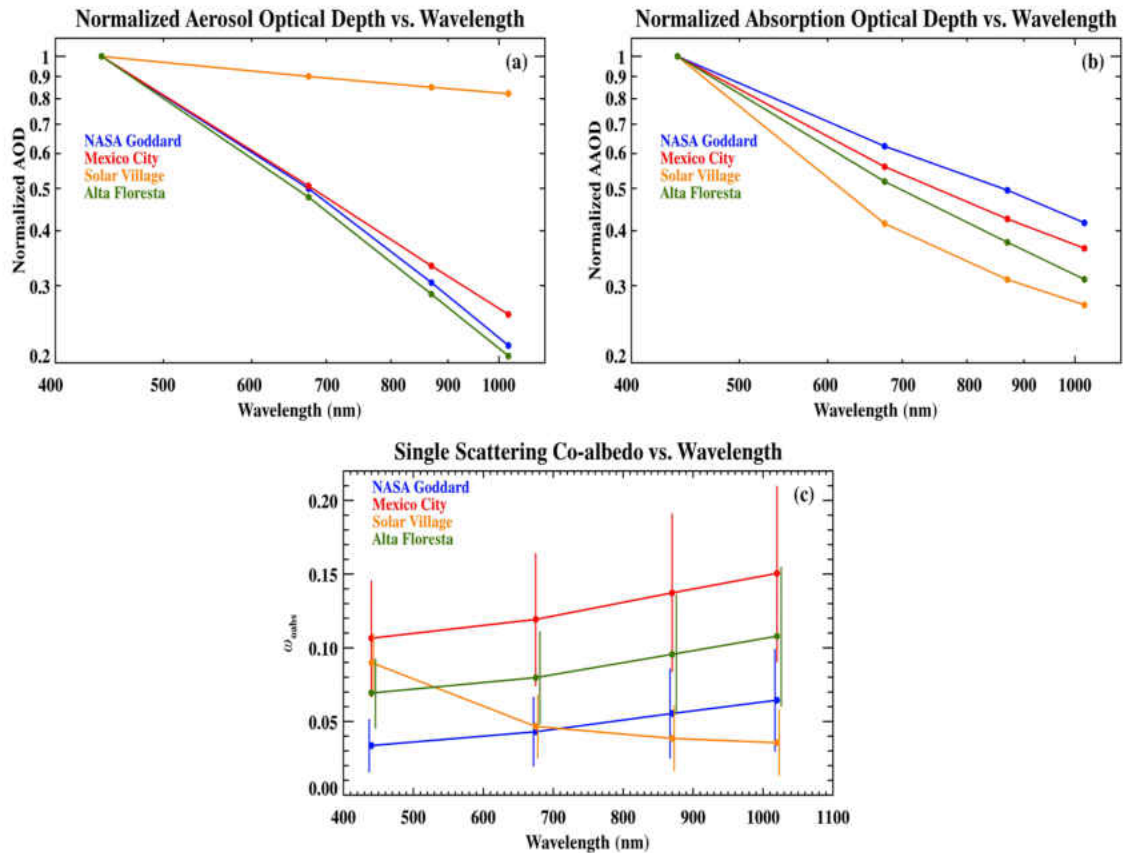


Figure 17. Log-log relationship of the mean extinction aerosol optical depth (AOD) spectral dependence for all aerosol cases at each single mode aerosol site. The AOD values are given as ratios to  $\text{AOD}_{440}$  after Chung et al. (2012) to show the degree of spectral dependence from the visible to near IR wavelengths. (b) Same as (a) but for absorption aerosol optical depth (AAOD). (c) Spectral dependence of the single scattering co-albedo ( $\omega_{\text{obs}}$ ) with error bars denoting  $\pm 1\sigma$ .

As illustrated in Figure 17a, Solar Village has the weakest AOD spectral dependence of all four sites indicating coarse mode particles. Alta Floresta has the strongest spectral dependence which suggests fine mode particle dominance. NASA Goddard and Mexico City have spectral dependences between the other two sites but exhibit strong fine mode dominance.

In terms of absorption (Figure 17b), the four sites have spectral AAOD dependences similar to what is presented in Figure 16b with NASA Goddard and Mexico City having the weakest AAOD dependence and Solar Village having the strongest

dependence. Carbonaceous pollution and mineral dust aerosols tend to strongly absorb in the UV and visible (440-675 nm) and weakly absorb in the near IR (> 675 nm). Note that Mexico City has a stronger spectral dependence than NASA Goddard. This is likely attributed to a higher fraction of strongly absorbing carbonaceous particles from the larger urban/industrial influences in and around central Mexico than the eastern United States. Alta Floresta has an intermediate AAOD spectral dependence which is likely indicative of carbonaceous particles consisting of BC and OC mixtures (Reid et al. 1999; Andreae and Gelencsér 2006; Lack and Cappa 2010).

Figure 17c offers an alternative perspective of the aerosol absorptive properties at the four sites. We propose that the spectral dependence of the single scattering co-albedo ( $\omega_{\text{obs}}$ ) can be used to better separate the different aerosol types by comparing the relative amount of absorption in the visible to the absorption in the near IR. The  $\omega_{\text{obs}}$  parameter demonstrates the absorptive nature due to the internal composition of the particles rather than particle loading since it is basically a ratio of AAOD to AOD. At NASA Goddard, Mexico City, and Alta Floresta,  $\omega_{\text{obs}}$  increases with increasing wavelength due to carbonaceous influences. Mexico City has the strongest spectral  $\omega_{\text{obs}}$  dependence likely due to a higher amount of BC and strongly absorbing OC influences. The spectral dependence at Alta Floresta indicates biomass particles that have similar BC and OC influences. NASA Goddard shows a weaker spectral dependence due to more sulfate and weakly absorbing OC content. However, there are BC influences that led to an increase of absorption with wavelength. In contrast to the other sites, Solar Village has a strong decrease in absorption in the visible that levels off in the near IR. The iron oxide content of the mineral dust is largely responsible for this decrease in the visible and the size of

the dust particles (more scattering) is responsible for the continued decrease in the near IR.

The absorptive characteristics of the aerosols at each site become less ambiguous with  $\omega_{\text{oabs}}$  as opposed to AAOD in that more information about aerosols can be inferred by the  $\omega_{\text{oabs}}$  spectral dependence. Therefore, it should follow that  $\omega_{\text{oabs}}$  can be used to infer the internal (or physico-chemical) nature since each aerosol region exhibits a unique spectral dependence reflecting either a pure aerosol type or a combination of aerosol types in the case of mixtures. Hence, this parameter along with the Angström exponent ( $AE_{\text{AOD}}$ ) can provide useful information for analyzing the seasonal and regional variability of aerosol types.

#### **Aerosol Classification Method Involving $AE_{\text{AOD}}$ and $\omega_{\text{oabs}}$**

As demonstrated in the previous section, the spectral dependence of  $\omega_{\text{oabs}}$  provides more information than AAOD regarding the physico-chemical properties of the aerosol types discussed in this study in addition to the  $AE_{\text{AOD}}$  parameter representing particle size. Thus, these two parameters are combined to illustrate an innovative classification method that is first tested at the single mode aerosol sites which will aid in serving as a baseline for analyzing the aerosol properties. The method will then be applied over more complex aerosol source regions in Asia, North America, and the remote Atlantic Ocean (Chapter V).

Figure 18 presents the results of classification method on the four single mode aerosol dominated AERONET sites. A frequency analysis using all aerosol cases from the sites was performed and it was determined that a  $\omega_{\text{oabs}440}$  value of 0.07 denotes the demarcation line between strongly and weakly absorbing aerosols (results not shown).

For the two pollution sites, the aerosol particles are dominated by fine mode ( $AE_{AOD} > 0.75$ ). Therefore we define Region I as having weakly absorbing particle dominance (most of  $\omega_{\text{obs}}$  values  $< 0.07$ ) and Region II as having strongly absorbing particle dominance (most of  $\omega_{\text{obs}440}$  values  $> 0.07$ ). Note that Mexico City has large  $\omega_{\text{obs}}$  variability with the majority of the aerosol cases located at Region II. Region III represents coarse mode, strongly absorbing mineral dust aerosol cases ( $AE_{AOD} < 0.75$ ). Region IV represents coarse mode, weakly absorbing aerosols that are primarily observed at the Solar Village site (desert).

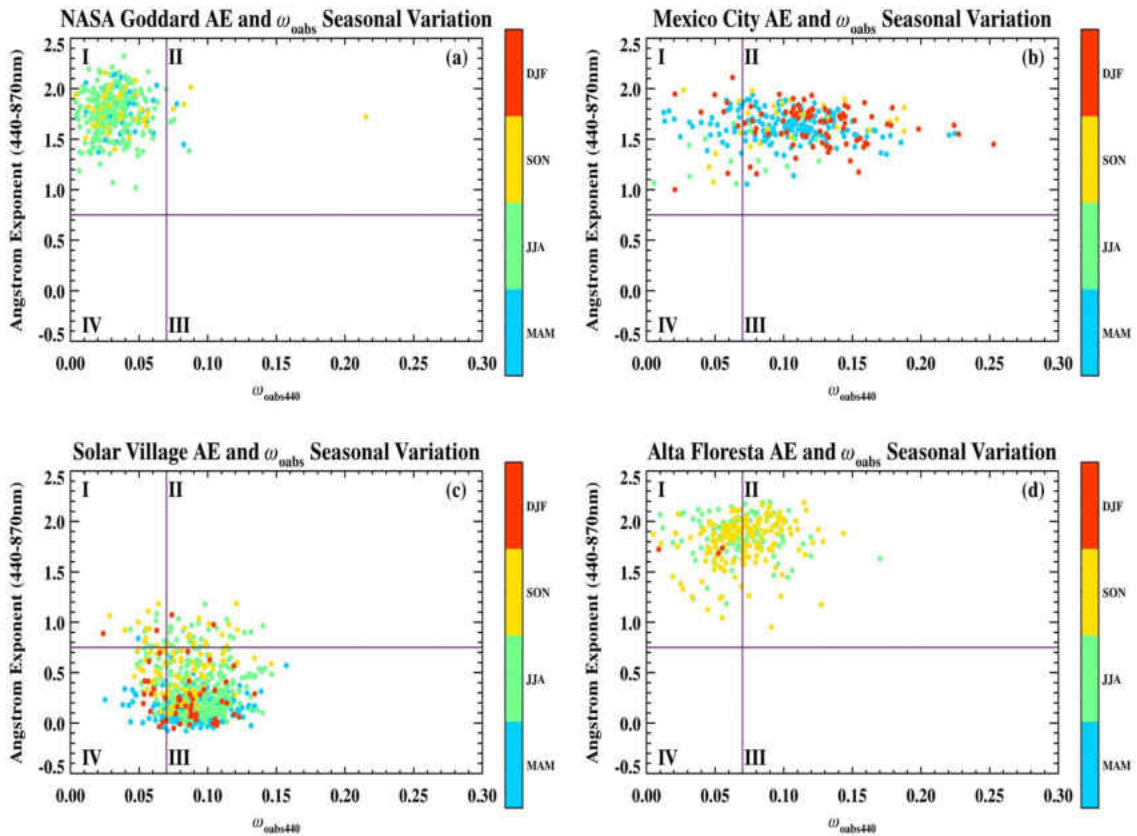


Figure 18. Classification of four AERONET sites representing weakly absorbing (NASA Goddard) and strongly absorbing (Mexico City) pollution, mineral dust (Solar Village) and biomass burning (Alta Floresta) aerosol types. The time period for each site is 1993-2011 (NASA Goddard), 1999-2009 (Mexico City), 1999-2010 (Solar Village) and 1993-2010 (Mexico City). A threshold of  $AE_{AOD}=0.75$  is used to define the fine ( $> 0.75$ ) and coarse ( $< 0.75$ ) mode aerosols, while weakly ( $\omega_{\text{obs}440} < 0.07$ ) and strongly ( $\omega_{\text{obs}440} >$

0.07) absorbing aerosols are set at  $\omega_{\text{obs440}} = 0.07$ . Solar Village is near Riyadh, Saudi Arabia, which is dominated primarily by mineral dust aerosols but can be occasionally influenced by urban aerosols. It should be noted that winter, spring, and summer cases are presented at the Alta Floresta site (southern hemisphere).

### **Aerosol Transport**

Aerosols such as pollution, mineral dust, and biomass smoke can affect downwind regions that are several hundreds to thousands of kilometers from their source regions. These impacts include decreases in incoming solar radiation, alterations in cloud properties, and human health concerns. Ongoing urban/industrialization in Asia, mineral dust storms, and biomass burning processes all strongly contribute to these effects. Thus, there continues to be a strong need to investigate how the properties of aerosols evolve and impact distant locations during transport.

The National Aeronautics and Space Administration (NASA) led a field experiment known as the Intercontinental Chemical Transport Experiment – Phase B (INTEX-B)<sup>1</sup> during the spring of 2006 over the eastern Pacific Ocean (Singh et al. 2006). The major goals of INTEX-B were to (a) quantify the transpacific transport and evolution of Asian dust and (b) assess its implications for regional climate using aircraft in situ measurements. The Logan et al. (2010) study investigated the optical properties of the Asian dust plumes during transport over the remote Pacific where the DC-8 aircraft conducted intensive investigations of the plumes using DIAL and nephelometer observations. Terra/Aqua satellite measurements were also used to outline the transpacific transport process during the spring season (March-May) of 2006. Based on

---

<sup>1</sup> INTEX-B, the second phase of the main field experiment called INTEX-North America (INTEX-NA), was a two-part field experiment with the first half of INTEX-B conducted over Mexico, but for this paper, INTEX-B here only refers to the second half of the campaign over the eastern Pacific Ocean.

available data, three scientific issues concerning Asian dust were examined: (1) aerosol properties along with surface and Top-Of-Atmosphere (TOA) radiation budgets, (2) aerosol properties as functions of both their points of origin and destination, and (3) the major transport pathway based on the satellite (Terra/Aqua) measured AOD.

The Logan et al. (2013c) study investigated biomass smoke transport from wildfire source regions in the western United States to the Northern Great Plains using AERONET retrieved aerosol data, CALIPSO satellite products, and particle trajectory model data. Similar to quantifying Asian aerosol properties during transport in the INTEX-B study (Logan et al. 2010), biomass smoke aerosols also vary during transport in terms of their radiative and chemical properties. The carbonaceous content (BC and OC) of biomass smoke aerosols depend on their mode of generation. The high temperature, flaming combustion mode generates smoke particles that are strongly absorbing due to their high BC content. However, the low temperature smoldering combustion mode generates particles that are weakly absorbing with less BC and more OC compounds. During transport, the carbonaceous compounds undergo chemical processes (e.g., photolysis and oxidation) that weaken the absorption of biomass smoke. Hence, it is evident that these particles can greatly influence the aerosol direct effect since strongly absorbing biomass smoke can warm the atmospheric layer in which they reside. In contrast, weakly absorbing biomass smoke can reflect more solar radiation back to space.

The long range transport of aerosols can also impact cloud formation processes downwind of the aerosol source regions. The Logan et al. (2014) study investigated aerosol influences on marine boundary layer (MBL) CCN. Using multiplatform aerosol

and CCN data from the 2009-2010 Clouds, Aerosols, and Precipitation in the Marine Boundary Layer (CAP-MBL) field campaign conducted over Graciosa Island, Azores, several aerosol types and their probable source regions are identified by the aerosol classification method developed in this dissertation. As a result, the effects of the aerosol types on  $N_{CCN}$  can be quantified.

## CHAPTER V

### RESULTS AND DISCUSSIONS

#### **SQ1: What Are the Seasonal and Regional Variations of Aerosol Physico-chemical Properties at Four Selected Asian Locations?**

This dissertation employs the AERONET retrieved particle volume size distribution along with four aerosol parameters:  $AOD_{440}$ ,  $AAOD_{440}$ ,  $AE_{AOD}$ , and  $AAE_{AOD}$  in order to infer the regional and seasonal variation of aerosol types at four selected sites in Asia. First, the annual and seasonal size distributions along with the monthly means of the aerosol parameters are analyzed and discussed. The annual and seasonal means as well as their standard deviations are summarized in Table 4. These two subsections will lay a foundation for the feasibility of using the  $AE_{AOD}$  and  $\omega_{obs}$  parameters in the aerosol classification method in the final subsection.

#### **Annual and Seasonal Aerosol Size Distributions**

Figure 19 shows the annual and seasonal averaged particle volume size distributions from the four selected AERONET sites. As illustrated in Figure 19a both the Xianghe and Taihu sites show a bimodal distribution with a fine mode peak at  $0.16 \mu\text{m}$  and coarse mode peak near  $3 \mu\text{m}$ . Note that Xianghe has a larger coarse than fine mode volume while the opposite is true for Taihu. The SACOL site is bimodal with a large coarse mode peak at  $2.1 \mu\text{m}$ . Mukdahan is a near mirror image of SACOL having a large fine mode peak at  $0.2 \mu\text{m}$ .

Though Figure 19a shows the annual mean variations of aerosol size distribution, the seasonal variations of particle volume size distribution illustrates any possible periodic dependence of aerosol generation.

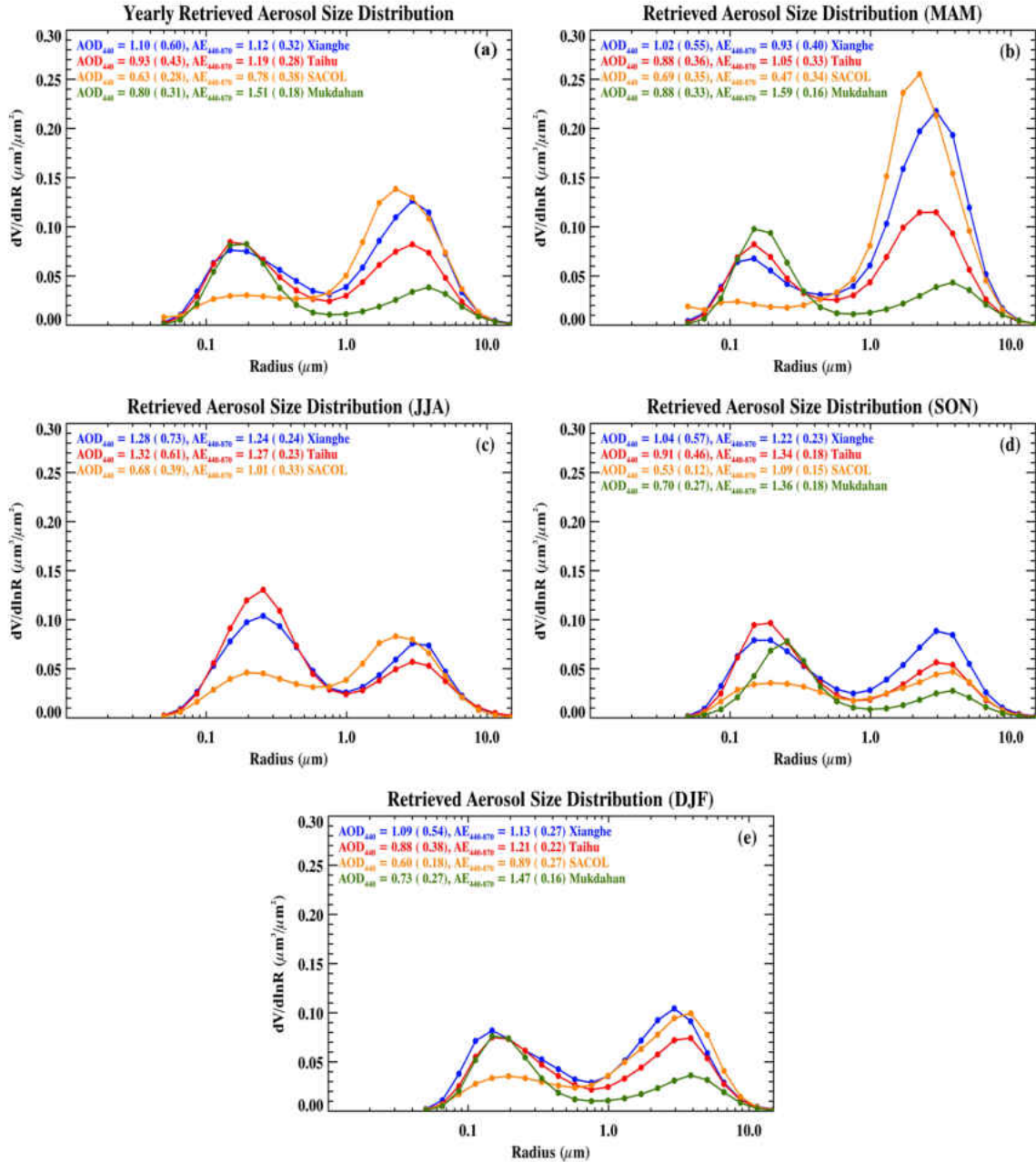


Figure 19. Aerosol volume size distributions over the four selected AERONET sites. (a) Annual and (b-e) seasonal means (standard deviation) of aerosol optical depth (AOD) and Angström exponent ( $AE_{AOD}$ ). Note that there is no summer observation data at Mukdahan due to few retrievals ( $< 3$ ) during that season (wet monsoon).

Figures 19b-e suggest that the Xianghe, Taihu and SACOL sites had coarse mode dominance during the spring season likely due to mineral dust influences from both the Gobi and Taklamakan Deserts (Eck et al. 2005; Huang et al. 2008a, b; Eck et al. 2010). During the summer season, there is a change in aerosol size dominance from coarse to fine mode. The wet monsoon begins during the early summer season which in turn enables southerly winds to transport pollution and biomass aerosols as well as moisture from the lower latitudes of southern and eastern Asia northward (Eck et al. 2005; Gautam et al. 2012). The increased humidity creates an abundance of suspended water droplets capable of facilitating gas to particle processes which can lead to a larger concentration of fine mode aerosols (Yao et al. 2002; Eck et al. 2005; Li et al. 2007a; Pathak et al. 2009; Jin et al. 2011). SACOL also has a slightly larger fine mode during the summer season than during the spring, which is likely due to local pollution and biomass burning aerosol generation (Xin et al. 2007; Huang et al. 2008b). Mukdahan appears to be influenced by biomass burning activity throughout the dry season from numerous wildfires and ongoing agricultural activities (Gautam et al. 2012). It should be noted that due to wet monsoon activity the Taihu and Mukdahan sites have only limited observations of aerosols, especially during the summer months (Eck et al. 2005; Gautam et al. 2012).

During the autumn months (SON), there is a smaller fine mode volume contribution than the summer season at the Xianghe, Taihu and SACOL sites. This likely reflects decreased humidity as well as diminished aerosol loading (as given by lower  $AOD_{440}$ ) (Eck et al. 2005). At Taihu, the fine mode volume contribution is the highest of all four sites due to influences from local urban/industrial pollution (Shanghai) and biomass burning aerosols (Xin et al. 2007; Eck et al. 2010; Kondo et al. 2011). At the

Mukdahan site, the fine mode  $r_{\text{eff}}$  shifts from 0.16 to 0.25  $\mu\text{m}$  due to crop burning and other agricultural processes during this season (Gautam et al. 2012).

The winter months (DJF) show equal coarse and fine mode aerosol contributions at Taihu while at the Xianghe site, the coarse and fine modes are similar in magnitude as in the autumn months. Late winter dust activity (mineral dust and loose soil from bare farmlands) may also be responsible for the increased coarse mode influence at both Xianghe and SACOL (Huang et al. 2008b). Though the volume size distribution is useful in discerning aerosol influences according to size, the other aerosol parameters discussed in the following section will further illustrate aerosol influences according to type and composition.

### **Seasonal Variation of Aerosol Optical Depth**

In Figure 20a, Xianghe and Taihu both have summer maxima and late autumn/winter minima in  $\text{AOD}_{440}$  with more variability at Xianghe indicating more aerosol sources (Xin et al. 2007; Yang et al. 2008; Yang et al. 2009; Pan et al. 2010). The increased variability seen at Taihu in the summer/early autumn is due to biomass aerosol intrusions (Xin et al. 2007). SACOL has maxima in April and June where the spring maximum can be attributed to strong dust activity beginning in early spring lasting through May, while the summer maximum (and maximum variability) corresponds to industrial influences from Lanzhou and biomass burning aerosols from neighboring regions (Xin et al. 2007; Huang et al. 2008b). At Mukdahan, biomass burning activity is at a maximum during March with a second maximum in the autumn months after the rainy season (Gautam et al. 2012).

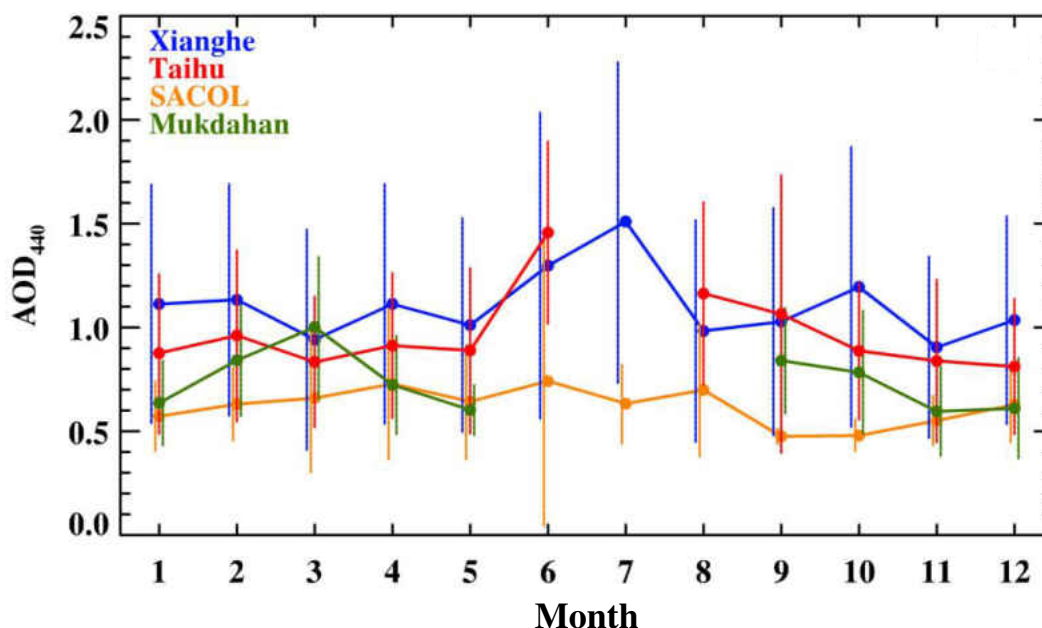


Figure 20. Monthly means of the aerosol optical depth (AOD) parameter at the 440 nm wavelength. Note that the missing monthly means at Taihu and Mukdahan are due to limited observations of aerosols during prolonged wet periods (summer season). The error bars represent  $\pm 1\sigma$ .

### Seasonal Variation of Absorption Aerosol Optical Depth

From Figure 21, Xianghe had both the largest AAOD<sub>440</sub> variability (0.045-0.14) and maximum AAOD<sub>440</sub> value (0.14). The summer minima and winter maxima at Xianghe and Taihu indicate that the different particles over these two sites were weakly absorbing during the summer months and strongly absorbing during the winter months. SACOL has near constant AAOD<sub>440</sub> values with a first maximum in the spring and a lesser second maximum in the autumn suggesting mineral dust episodes. Mukdahan had higher AAOD<sub>440</sub> values during the pre-monsoon months that shifted to lower values after the rainy season.

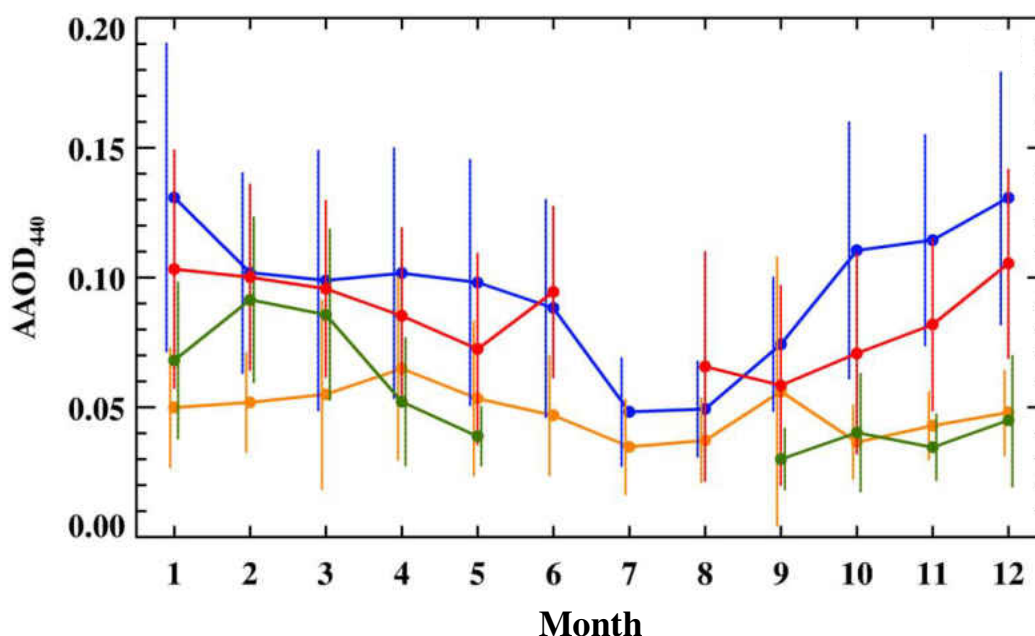


Figure 21. Same as Fig. 20 but for absorption aerosol optical depth (AAOD).

### Seasonal Variation of Angström Exponent

Figure 22 illustrates the seasonal variation in  $AE_{AOD}$  where Xianghe, Taihu, and SACOL had spring minima due to coarse mode, mineral dust particle influence with a more prolonged dust influence period at SACOL. The increase in  $AE_{AOD}$  during the summer months is due to fine mode pollution and moisture influences at Xianghe and Taihu while at SACOL ambient mineral dust mixes with local pollution from Lanzhou City. This is given by the increase in the volume fine mode while with volume coarse mode remains dominant (Figure 19c) thereby keeping the mean  $AE_{AOD}$  lower than the other sites (Clarke et al. 2004; Zheng et al. 2005; Xin et al. 2007). The monthly mean  $AE_{AOD}$  values at Mukdahan are higher than those at the other three sites due to biomass burning particles being the dominant aerosol type (Gautam et al. 2012).

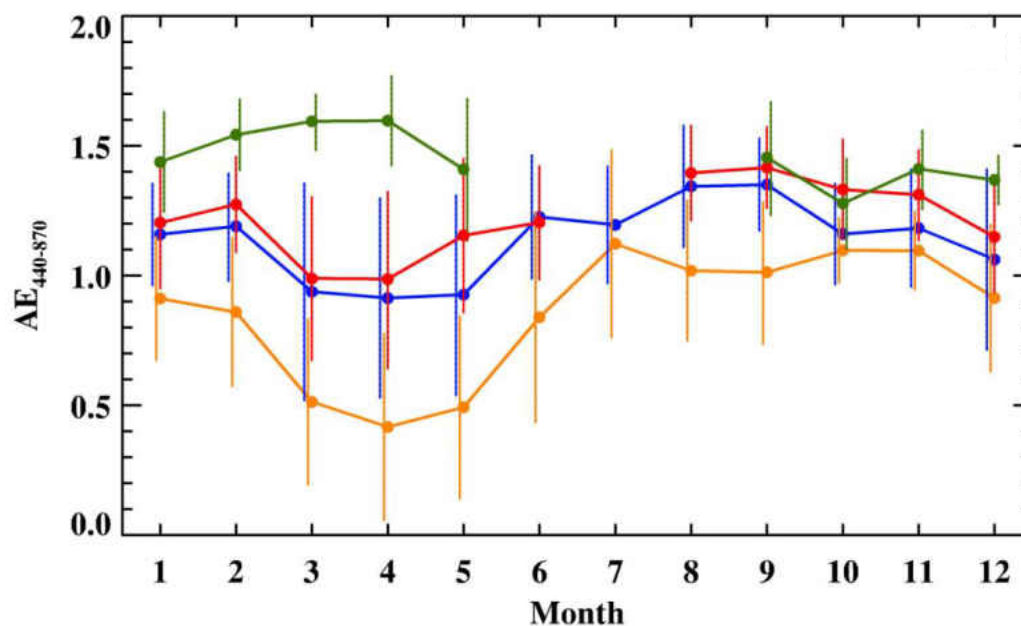


Figure 22. Same as Fig. 20 but for the Angström exponent with a spectral range of 440-870 nm.

### Seasonal Variation of Absorption Angström Exponent

Figure 23 shows the seasonal variation in  $AAE_{AOD}$ . Both Xianghe and Taihu had similar  $AAE_{AOD}$  trends throughout the year except for late spring. The  $AAE_{AOD}$  values reach a maximum nearly a month earlier at Taihu because the dust storm season typically diminishes by early May making it unlikely for mineral dust particles to greatly influence aerosol profiles in areas farther downwind of the Gobi and Taklamakan Deserts. It is more likely the maximum at Taihu in April is due to aerosols that are dominated by OC from industrial sources (Xin et al. 2007). During the summer, lower  $AAE_{AOD}$  values are exhibited at Xianghe and Taihu due to influences from sulfates and other carbonaceous aerosols with weak spectral AOD dependences (Yang et al. 2009; Russell et al. 2010). In the winter season, Xianghe has slightly higher  $AAE_{AOD}$  values than Taihu due to

carbonaceous aerosols generated from a combination of residential coal burning and industry (Zheng et al. 2005; Yang et al. 2009).

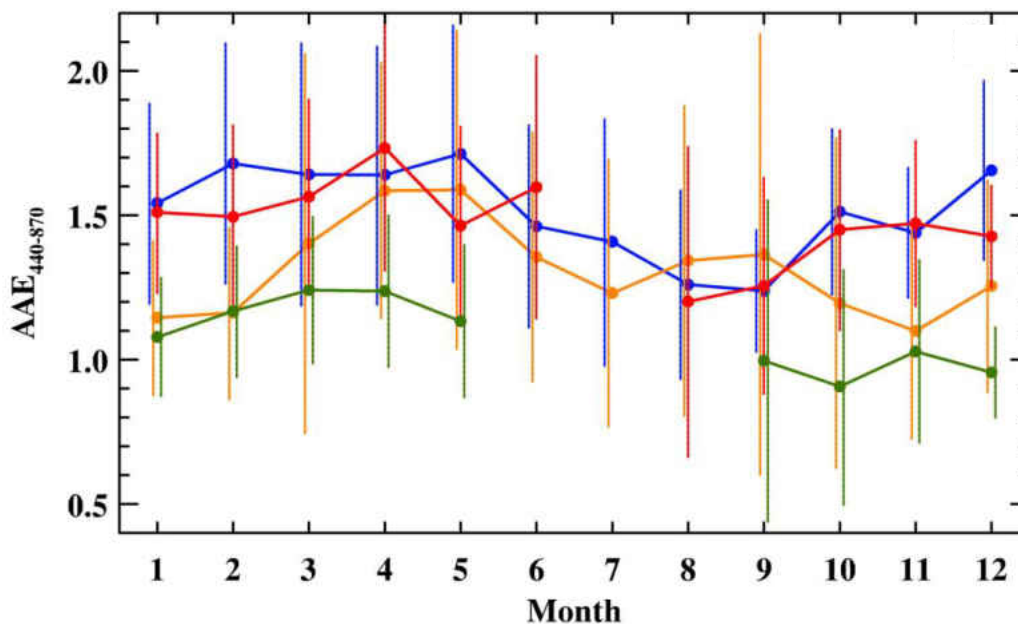


Figure 23. Same as Fig. 20 but for the absorption Angström exponent.

At SACOL, the monthly mean  $AAE_{AOD}$  values typically reflect local urban and industrial pollution from Lanzhou City but increase significantly from the winter to the spring, and reach a maximum in April-May due to the strong dust activity in this region of Asia (Xin et al. 2007; Huang et al. 2008a, b; Yang et al. 2009). At Mukdahan, the monthly mean  $AAE_{AOD}$  values are lower than those from the other three sites, suggesting that the biomass particles exhibit a weaker spectral dependence due to carbonaceous aerosols with more BC content than the other sites (Yang et al. 2009; Gautam et al. 2012).

The volume size distribution and the other parameters are useful in identifying regional and seasonal aerosol influences and characteristics. The  $AE_{AOD}$  and  $\omega_{oabs}$  parameters are explored as a means of further supporting our results by using aerosol

cases from regions dominated by pollution (absorbing and scattering dominant), mineral dust, and biomass particles. The four Asian sites are then shown as approximate combinations of the selected regions.

### **Spectral Dependences of AOD, AAOD, and $\omega_{\text{obs}}$**

The spectral dependence of AERONET retrieved AOD and AAOD is used to partition aerosol types according to composition (e.g., mineral dust and carbonaceous aerosols) at four selected Asian sites: SACOL (mineral dust region), Xianghe (mixed dust and urban/industrial aerosol region), Taihu (urban/industrial pollution region), and Mukdahan (biomass burning smoke region). Special attention is paid to the role of carbonaceous aerosols (BC and OC) prevalent in the pollution and biomass smoke aerosols with a strong emphasis on their absorptive properties and inherent radiative forcing which is typically ignored in many climate models (Chung et al. 2012). In Figures 24a and 24b, the AOD and AAOD values at all wavelengths are normalized to their 440 nm values in order to illustrate the relative mean extinctive and absorptive properties of all aerosol retrievals (Chung et al. 2012; Logan et al. 2013a). As illustrated in Figure 24a, SACOL has the weakest AOD spectral dependence of all four sites indicating coarse mode particles. Mukdahan has the strongest spectral dependence which suggests fine mode particle dominance. Xianghe and Taihu have an AOD spectral dependence between the other two sites due influences from both coarse and fine mode particles with Xianghe having more of a coarse mode influence (closer proximity to desert regions) while Taihu has more a fine mode influence (more sources of urban/industrial aerosols).

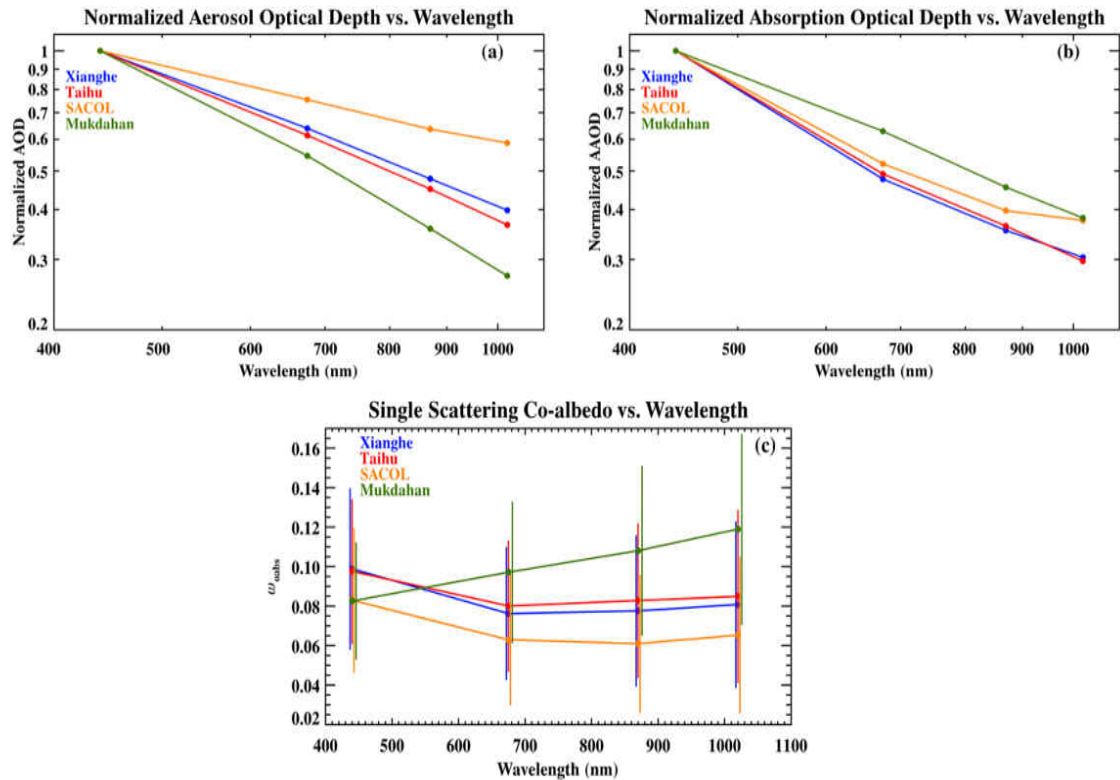


Figure 24. (a) Log-log relationship of the mean extinction aerosol optical depth spectral dependence for all aerosols cases at each AERONET site: 2001-2010 (Xianghe), 2005-2010 (Taihu), 2006-2011 (SACOL), and 2003-2009 (Mukdahan). The AOD values are given as ratios to  $AOD_{440}$  after the Chung et al. (2012) study to show the degree of spectral dependence from the visible to near IR. (b) Same as (a) but for absorption aerosol optical depth. (c) Spectral dependence of the single scattering co-albedo ( $\omega_{\text{obs}}$ ) with error bars denoting  $\pm 1\sigma$ .

In terms of absorption (Figure 24b), Mukdahan has a near linear AAOD spectral dependence which is likely indicative of biomass burning aerosols generated from different combustion phases with BC dominating the overall absorption (Reid et al. 1999; Andreae and Gelencsér 2006; Lack and Cappa 2010). Xianghe and Taihu have a stronger AAOD spectral dependence in the visible that weakens in the near IR suggesting OC dominant carbonaceous aerosols. SACOL has a similar spectral dependence in the visible which becomes negligible in the near IR primarily indicating mineral dust particles with varying amounts of iron oxides (Koven and Fung 2006; Chung et al. 2012).

Figure 24c shows that the carbonaceous biomass particles at Mukdahan tend to have a nearly linear increase in absorption with wavelength which is indicative of more influence of BC though there are likely OC influences as well (Bergstrom et al. 2007; Gautam et al. 2012). In contrast, the SACOL site has strong absorption in the visible but becomes weak in the near IR because dust particles are typically in the coarse mode and tend to scatter in the near IR region (Bergstrom et al. 2007). The Xianghe and Taihu sites nearly mirror one another with strong absorption in the visible but an increase in absorption with wavelength in the near IR again indicating the influences of absorbing carbonaceous particles, similar to Mukdahan.

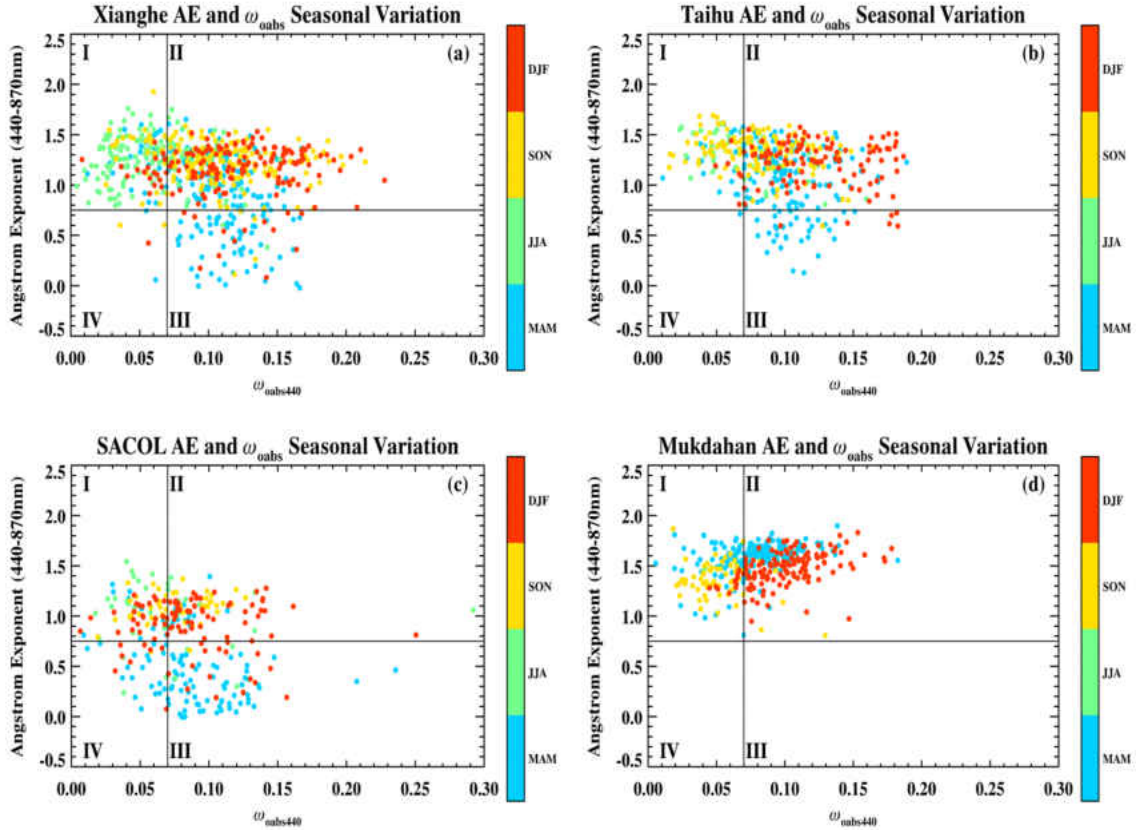


Figure 25.  $AE_{\text{AOD}}$  and  $\omega_{\text{obs}}$  classification of the aerosol physico-chemical properties over the four selected AERONET sites. The data are color-coded according to season to show correlations between aerosol composition/type and time of year.

### Aerosol Classification Method Involving $AE_{\text{AOD}}$ and $\omega_{\text{obs}}$

A probability distribution analysis of  $\omega_{\text{obs}}$  is used to illustrate the frequency of occurrence and seasonality of strongly absorbing ( $\omega_{\text{obs}} > 0.07$ ) and weakly absorbing ( $\omega_{\text{obs}} < 0.07$ ) aerosol cases. Figures 25a and 25b detail three seasonal groups of aerosols at Xianghe and Taihu. There is a noticeable seasonal dependence at Xianghe with nearly 55% of the fine mode, weakly absorbing cases occurring during the summer (Region I) and 90% of all fine mode strongly absorbing cases occurring in the autumn and winter seasons (Region II). The coarse mode, strongly absorbing aerosols are observed during the spring season primarily in Region III. Similarly at Taihu, 48% of the fine mode,

weakly absorbing cases in Region I occur during the early autumn while 75% of the fine mode, strongly absorbing cases occur during the late autumn and winter (Region II). Nearly 22% of the spring season aerosols are coarse mode, strongly absorbing.

At SACOL, all four regions contain aerosol cases with the majority of the spring season cases located in Regions III and IV (similar to the Solar Village site). The majority of the winter and autumn season aerosols are in Region II while the summer cases are in Region I. The mean  $AE_{AOD}$  and  $\omega_{\text{obs}440}$  values are lower in comparison to Xianghe and Taihu. This is due to the fact that SACOL is located within a dust region with fewer cities and outside aerosol influences, while Xianghe and Taihu are surrounded by many large cities and industry (Eck et al. 2005; Xin et al. 2007; Bi et al. 2009; Yang et al. 2009). This is also evident in Figures 26 and 27 where both the  $AE_{AOD}$  and  $AAE_{AOD}$  values for this site were lower than those at Xianghe and Taihu.

Comparing the Region I and II results at Mukdahan with Xianghe and Taihu, note that biomass burning aerosols present higher overall  $AE_{AOD}$  values (Figure 22). The variability in  $\omega_{\text{obs}440}$  is likely due to a wide variety of OC and BC particles generated by different smoldering or flaming combustion modes (Reid et al. 1999; Clarke et al. 2004; Zheng et al. 2005; Yang et al. 2009; Gautam et al. 2012). There is also a noticeable seasonal dependence where 90% of the winter cases are located at Region II while the most of autumn cases (88%) are generally in Region I. The spring season has the largest variability in  $\omega_{\text{obs}440}$  presumably due to aerosol influences from both controlled agricultural burning and natural wildfires from nearby forests (Gautam et al. 2012).

The large variability in  $AE_{AOD}$  and  $\omega_{\text{obs}440}$  classified in this method can be challenging. A great deal of overlap is evident which is likely attributed to inter-seasonal

shifts in aerosol type due to episodic changes in fuel type and meteorological patterns (Clarke et al. 2004; Eck et al. 2005). The overlap can also be attributed to inhomogeneous aerosol layers passing over the AERONET sites that add to the variability. At other AERONET sites affected by multiple aerosol sources (e.g., North America and the Azores), a priori knowledge of the regional and seasonal climatology will aid in using this method.

Table 4. Summary of statistical data from the four AERONET sites. Yearly means of  $r_{\text{eff}}$  are calculated from the seasonal mean values due to an uneven distribution of seasonal data.

		Xianghe		Taihu		SACOL		Mukdahan	
		For $\omega_0$ ; AOD <sub>440</sub> > 0.4		For $\omega_0$ ; AOD <sub>440</sub> > 0.4		For $\omega_0$ ; AOD <sub>440</sub> > 0.4		For $\omega_0$ ; AOD <sub>440</sub> > 0.4	
		mean ( $\sigma$ )	N <sup>a</sup>	mean ( $\sigma$ )	N	mean ( $\sigma$ )	N	mean ( $\sigma$ )	N
Year	AOD <sub>440</sub>	1.10 (0.60)	688	0.93 (0.43)	435	0.63 (0.28)	292	0.80 (0.31)	394
	AAOD <sub>440</sub>	0.10 (0.05)		0.09 (0.04)		0.05 (0.03)		0.07 (0.03)	
	AE <sub>AOD</sub>	1.12 (0.32)		1.19 (0.28)		0.78 (0.38)		1.51 (0.18)	
	AAE <sub>AOD</sub>	1.53 (0.39)		1.49 (0.37)		1.32 (0.49)		1.14 (0.29)	
	$r_{\text{eff}}$ (fine mode)	0.17		0.17		0.16		0.18	
	$r_{\text{eff}}$ (coarse mode)	2.26		2.19		2.05		2.51	
Spring	AOD <sub>440</sub>	1.02 (0.55)	198	0.88 (0.36)	162	0.69 (0.34)	108	0.87 (0.33)	191
	AAOD <sub>440</sub>	0.10 (0.05)		0.08 (0.04)		0.06 (0.03)		0.07 (0.03)	
	AE <sub>AOD</sub>	0.93 (0.40)		1.05 (0.33)		0.47 (0.34)		1.58 (0.15)	
	AAE <sub>AOD</sub>	1.67 (0.45)		1.58 (0.38)		1.52 (0.56)		1.24 (0.26)	
	$r_{\text{eff}}$ (fine mode)	0.15 (0.03)		0.15 (0.03)		0.13 (0.04)		0.16 (0.02)	
	$r_{\text{eff}}$ (coarse mode)	2.15 (0.28)		1.92 (0.25)		1.82 (0.23)		2.47 (0.42)	
Summer	AOD <sub>440</sub>	1.28 (0.73)	147	1.32 (0.61)	36	0.68 (0.39)	36	<sup>b</sup> n/a	n/a
	AAOD <sub>440</sub>	0.06 (0.04)		0.08 (0.04)		0.04 (0.02)		n/a	
	AE <sub>AOD</sub>	1.24 (0.24)		1.27 (0.23)		1.01 (0.33)		n/a	
	AAE <sub>AOD</sub>	1.39 (0.38)		1.37 (0.57)		1.30 (0.48)		n/a	
	$r_{\text{eff}}$ (fine mode)	0.20 (0.05)		0.21 (0.04)		0.19 (0.05)		n/a	
	$r_{\text{eff}}$ (coarse mode)	2.43 (0.26)		2.49 (0.34)		2.01 (0.44)		n/a	
Autumn	AOD <sub>440</sub>	1.04 (0.57)	180	0.91 (0.46)	126	0.53 (0.12)	48	0.70 (0.27)	63
	AAOD <sub>440</sub>	0.10 (0.04)		0.07 (0.04)		0.04 (0.01)		0.04 (0.02)	
	AE <sub>AOD</sub>	1.22 (0.23)		1.34 (0.18)		1.09 (0.15)		1.36 (0.18)	
	AAE <sub>AOD</sub>	1.41 (0.28)		1.41 (0.34)		1.18 (0.48)		0.97 (0.39)	
	$r_{\text{eff}}$ (fine mode)	0.17 (0.04)		0.18 (0.03)		0.19 (0.03)		0.21 (0.02)	
	$r_{\text{eff}}$ (coarse mode)	2.30 (0.22)		2.33 (0.27)		2.24 (0.35)		2.58 (0.37)	
Winter	AOD <sub>440</sub>	1.09 (0.54)	163	0.88 (0.38)	111	0.60 (0.17)	100	0.73 (0.27)	140
	AAOD <sub>440</sub>	0.12 (0.05)		0.10 (0.04)		0.05 (0.02)		0.07 (0.03)	
	AE <sub>AOD</sub>	1.14 (0.26)		1.21 (0.22)		0.89 (0.27)		1.47 (0.16)	
	AAE <sub>AOD</sub>	1.62 (0.36)		1.47 (0.26)		1.19 (0.32)		1.09 (0.22)	
	$r_{\text{eff}}$ (fine mode)	0.17 (0.04)		0.18 (0.04)		0.18 (0.04)		0.17 (0.02)	
	$r_{\text{eff}}$ (coarse mode)	2.18 (0.24)		2.31 (0.24)		2.23 (0.34)		2.51 (0.43)	

<sup>a</sup> Number of AERONET observations.

<sup>b</sup> Only one data point for this season.

## SQ2: How Do These Aerosol Properties Change During Transpacific and Intra-continental Long Range Transport?

This question is answered based upon the studies of Asian dust/pollution transport across the Pacific ocean during the INTEX-B campaign (Logan et al. 2010) and biomass burning transport over the North America during the summer of 2012 (Logan et al.

2013c). These studies show how aerosol physical and chemical properties change over distances ranging from several hundreds to thousands of kilometers.

### **Asian Aerosol Transport**

As shown in Figures 26 and 27, aerosol loading is greatest closest to the source region and declines in magnitude during transport to the sink region. Figure 27 shows the averaged AOD values retrieved from MODIS observations on Terra and Aqua from 7 April 2006 to 15 May 2006. The major pathways of aerosol plumes as observed from both Terra and Aqua are quite consistent, but the absolute values are slightly different over the land regions.

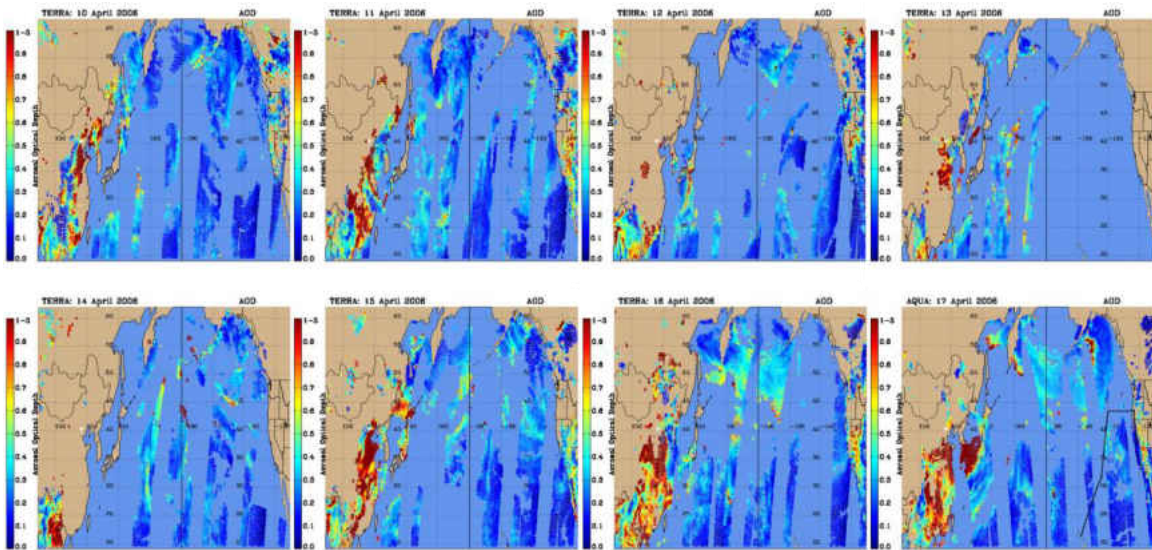


Figure 26. Transpacific transport of Asian aerosol plume (10 April 2006) intercepted by DC-8 aircraft over the eastern remote Pacific Ocean on 17 April 2006. Courtesy of Obrecht (2008) M. S. Thesis.

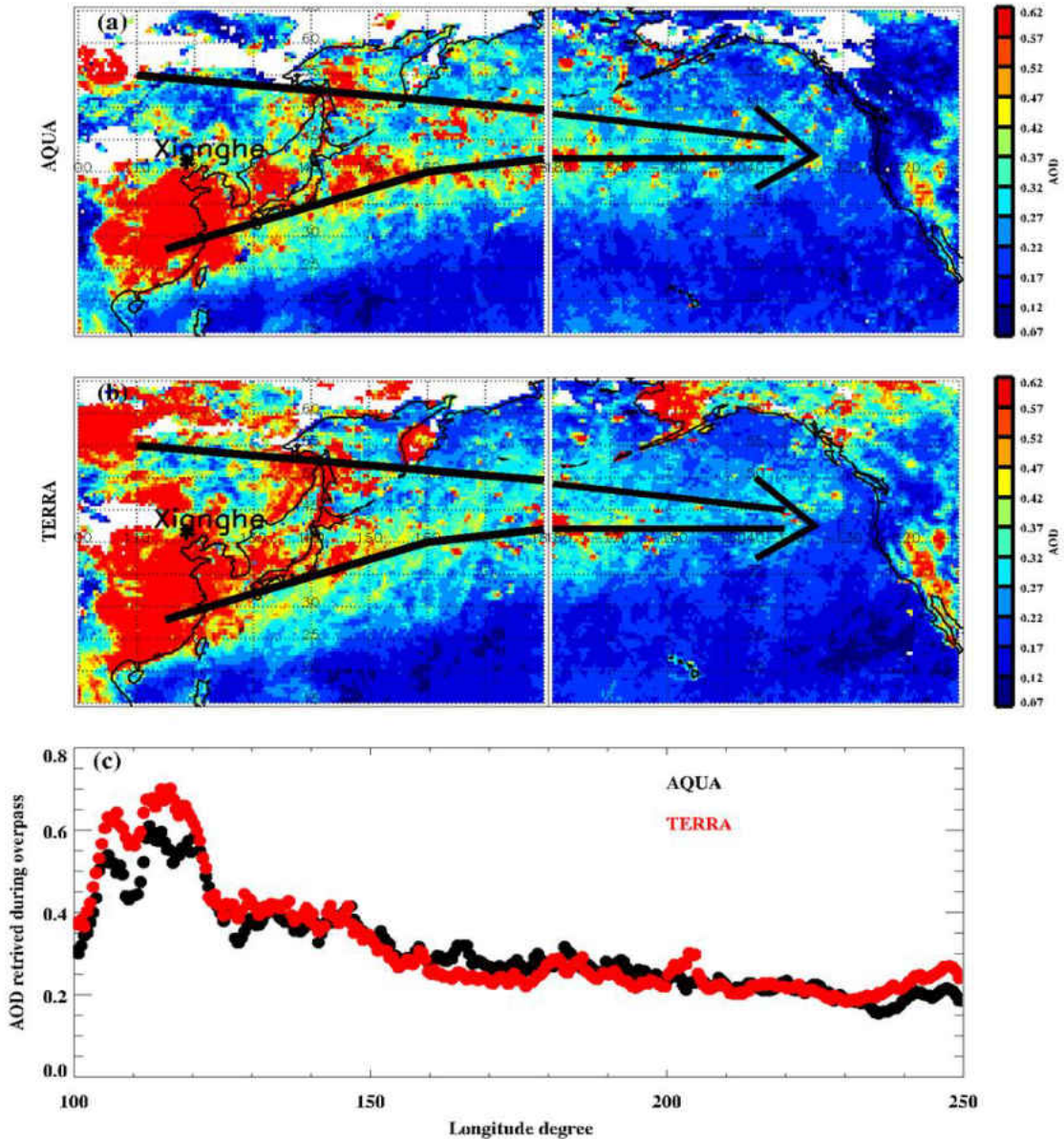


Figure 27. Averaged MODIS AOD values with  $0.5^\circ \times 0.5^\circ$  grid box during INTEX-B IOP the period 17 April-15 May 2006 on (a) Aqua and (b) Terra, and (c) their overall transpacific transport zonal trend.

As illustrated in Figure 27a and 27b, there are two dust plumes: the pollution plume (bottom arrow) and the dust plume (top arrow) originated from two different source regions. Note that there is a large gap in both Terra and Aqua (white, no retrievals from MODIS) over Mongolia, which may represent very high AOD which cannot be

retrieved by the current MODIS aerosol retrieval algorithm. Both plumes originated from two different regions which have two different paths that finally meet over the remote Pacific. This study qualitatively demonstrated the plume pathway trend using the Terra/Aqua observations, but did not quantitatively address the absolute difference of their AOD retrievals, which is beyond the scope of this research effort. Transpacific transport during INTEX-B appears to have a steady northeasterly direction as barely any aerosols are found below 35°N latitude once they reach the eastern Remote Pacific. Though there are indications of meridional flow in certain individual cases, the general flow across the Pacific for the aerosols is zonal.

Plume characteristics are given by the AOD values from both the Terra and Aqua retrievals. As the aerosols are transported across the Pacific Ocean, they are prone to both wet and dry deposition as well as dispersion over time. Figure 27c shows a steady decline in aerosol optical properties over time along their transport pathway. The concentration of fine mode aerosols generally decreases in the absence of dust but when mixed with dust, heterogeneous chemical reactions can occur which may cause a slow degradation of the total aerosol layer (Leitch et al. 2009). For example, the AOD values peak over the east coast of China, then drop significantly over the East China Sea, and eventually level off to the values close to 0.2 as they approach the remote Pacific. The major plume transport pathway can be seen clearly by following the retrieved AOD values: the plumes with very high AOD values when they exited the Asian land, transported slightly northeast, turned slightly eastward after passing through the middle of the Pacific until reaching near the 145°W longitude, then turned northeast toward the west coast of Canada.

The dust plumes shown in Figure 27 were also observed by DC-8 aircraft over the remote Pacific. Figure 28 shows the time period and altitudes of aerosol scattering ratios at 1064 nm measured by DIAL onboard DC-8 aircraft.

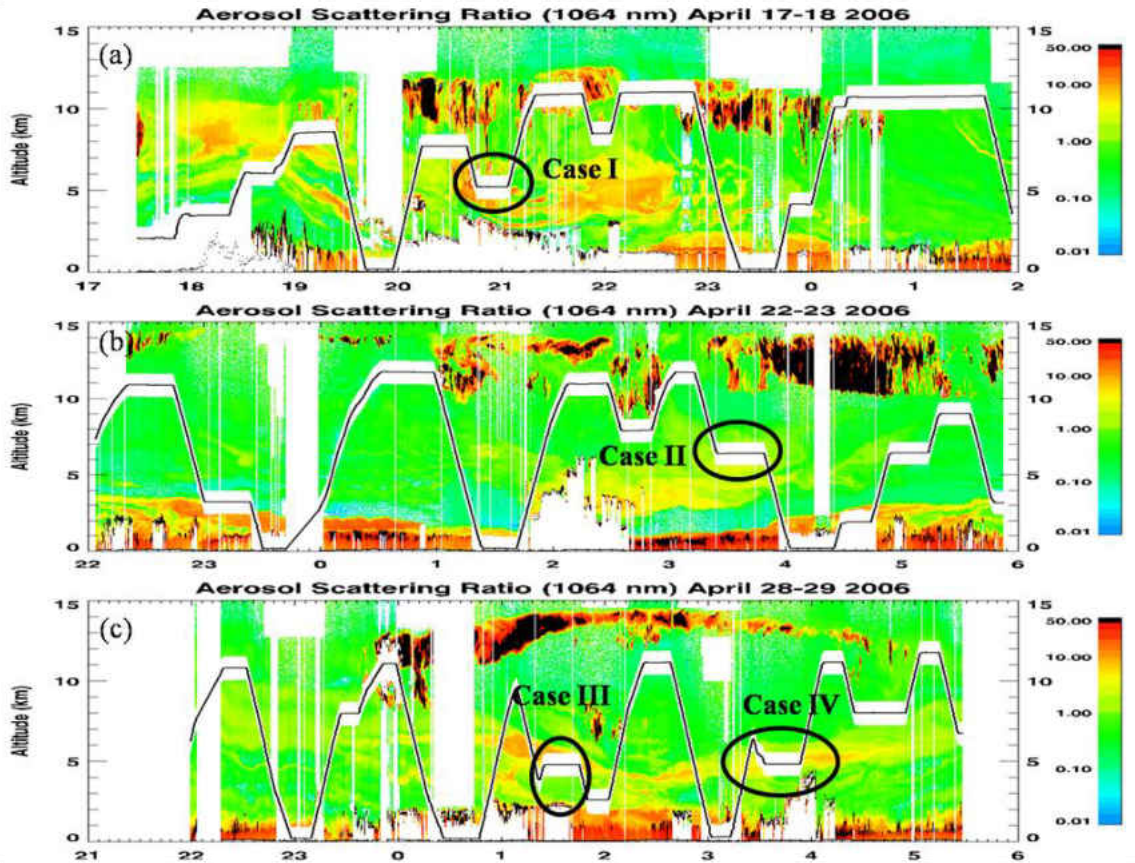


Figure 28. Aerosol scattering ratios observed by Differential Absorption LIDAR (DIAL) onboard the DC-8 aircraft during the INTEX-B field campaign over the remote Pacific Ocean. The four selected dust events used in this study: (a) Case I, (b) Case II, and (c) Cases III and IV.

Four cases are identified by the following criteria: (a) aerosol scattering ratios must be between 5 and 20 and (b) plumes must be above the marine boundary layer ( $> 2$  km) (Figure 28). Scattering ratios approaching 50 typically denote cloud layers and attenuation of the LIDAR signal can clearly be seen. Conversely, lower scattering ratios ( $< 1$ ) can denote clear air or ultrafine particulate matter and may not accurately represent Asian aerosols. However, it is difficult to quantitatively analyze the dust plumes by using

the DIAL measurements only, especially for discerning the fine and coarse mode aerosols in the dust plumes. Therefore, it is necessary to use the nephelometer data to do further analysis.

The scattering coefficient ( $\sigma_{sp}$ ), Angström exponent ( $AE_{neph}$ ), and spectral curvature ( $\delta\alpha$ ) parameters are used as proxies for aerosol loading, size, and mode dominance, respectively. Gobbi et al. (2007) proposed a method involving both  $\delta\alpha$  and  $AE_{neph}$  to track mixtures of pollution with dust. Spectral curvature is defined as the change in  $AE_{neph}$  over a spectral range of 450-700 nm and is useful in separating fine mode aerosols ( $\delta\alpha < 0$ ) from mixtures of fine and coarse modes ( $\delta\alpha \sim 0$ ). It is given by the equation

$$\delta\alpha = AE_{neph450-500} - AE_{neph500-700}. \quad (9)$$

Gobbi et al. (2007) demonstrated that  $\delta\alpha$  can be very close to zero under the conditions of low concentrations of fine mode aerosols. Under conditions of high concentrations of fine mode aerosols,  $\delta\alpha$  can be much less than zero. During periods of high humidity, particles can undergo hygroscopic growth which may artificially inflate  $\delta\alpha$  values to near zero though the fine mode will generally dominate the overall physical properties of the aerosol plume more than the coarse mode. A summary of the  $AE_{neph}$  and  $\delta\alpha$  parameters are included in Table 5.

For the 17 April 2006 dust event (Case I), the spectral data show a weak spectral dependence of  $\sigma_{sp}$  values at three different wavelengths (450, 550, and 700 nm) (Figure 29a) until a peak at 2100 UTC appears where the spectral dependence increases suddenly. Immediately after the peak, the dependence becomes negligible. Figure 29b shows that the mean (and standard deviation)  $AE_{neph}$  is  $0.46 \pm 0.63$ , suggests that an abundance of

coarse mode particles existed in the plume. Though the mean  $\delta\alpha$  is strongly negative (-0.49) the large standard deviation (1.61) suggests a large variability in aerosol size likely due to the presence of fine mode aerosols. Note that there is a noticeable cluster of data points very close to -0.2 on the  $\delta\alpha$  axis.

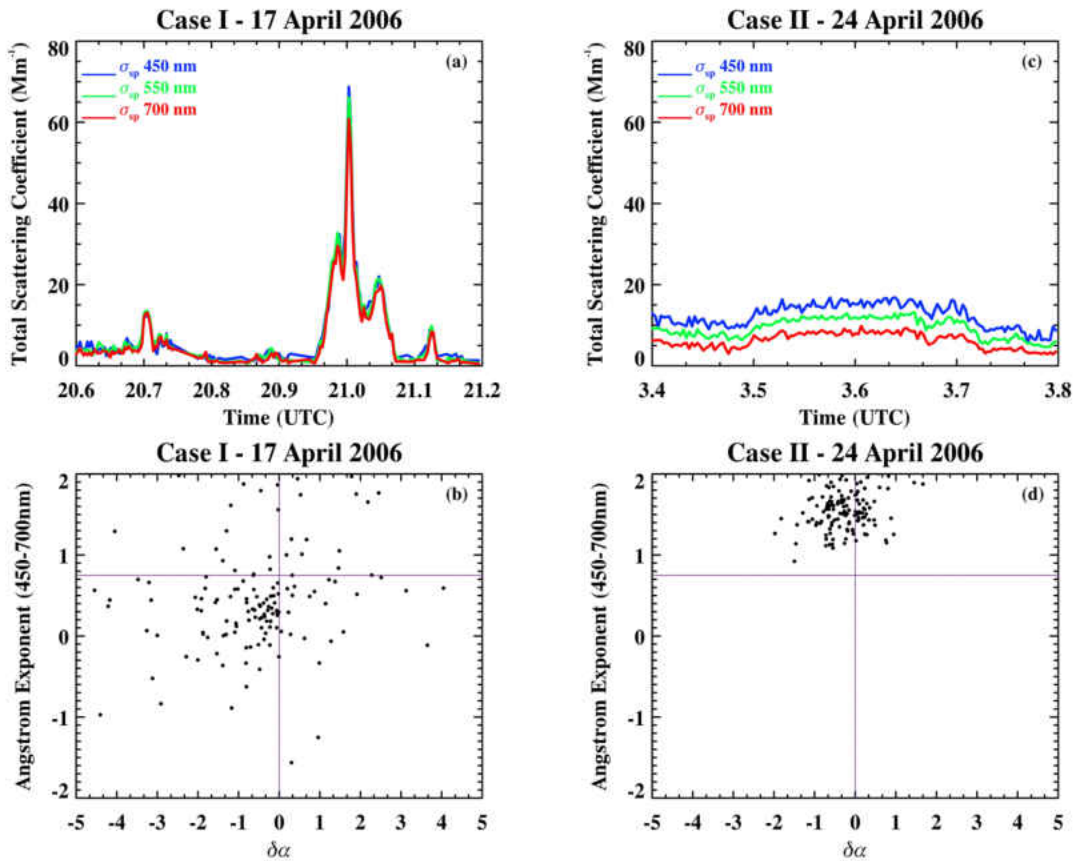


Figure 29. (a,b) Case I and (c,d) Case II. The scattering coefficients ( $\sigma_{sp}$ ) are measured by the DC-8 nephelometer at three wavelengths (450, 550, and 700 nm). The Angström exponent ( $AE_{neph}$ ) and spectral curvature ( $\delta\alpha$ ) are derived from  $\sigma_{sp}$ .

The 24 April 2006 dust event (Case II, Figure 29c) shows a strong  $\sigma_{sp}$  spectral dependence. The  $\sigma_{sp}$  at the shorter wavelengths (450 and 550 nm) are consistently larger than those at the longest wavelength (700 nm) because the backward scattering coefficients decrease with increasing the wavelength with the presence of fine mode aerosols in the plume. The mean  $AE_{neph}$  (Figure 29d) is  $1.53 \pm 0.23$  and the  $\delta\alpha$  values lie

primarily in the negative range with a mean value of  $-0.31 \pm 0.63$ , which indicates a strong influence of Asian pollution in this case.

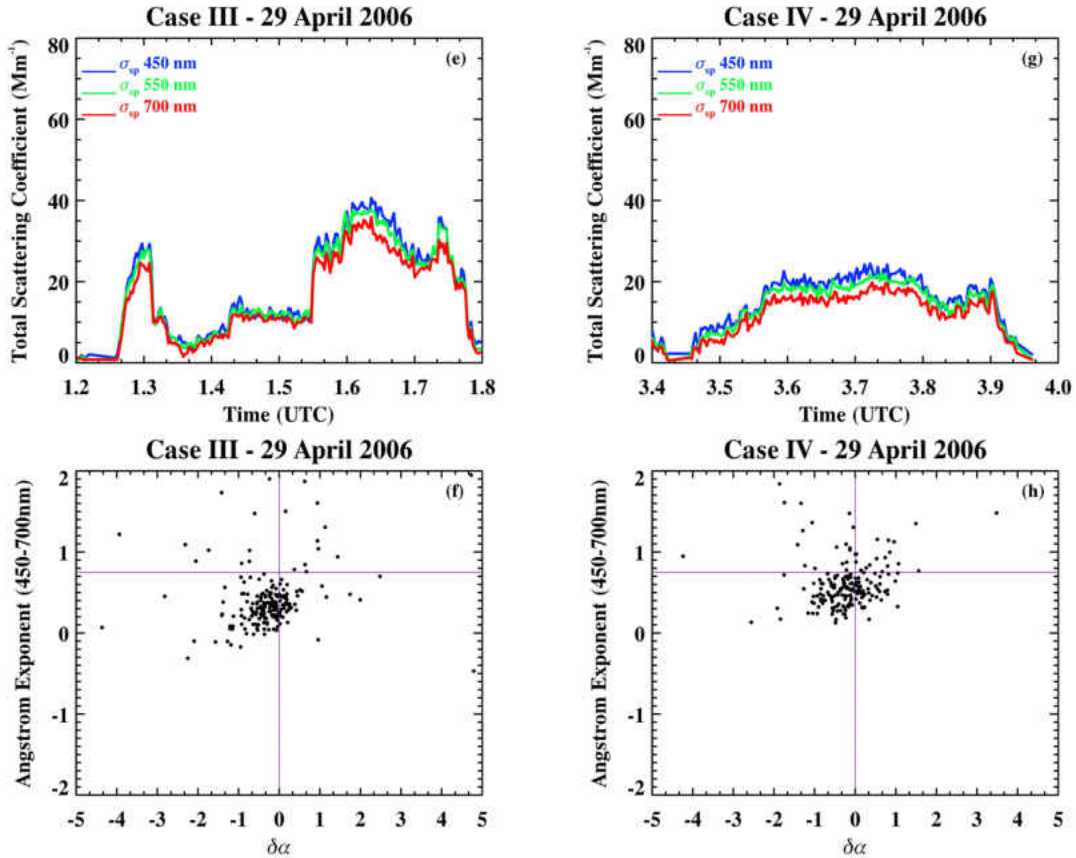


Figure 29 continued. (e,f) Case III and (g,h) Case IV.

The 29 April 2006 dust events (Cases III and IV) were observed at different time periods (Figure 28c). For Case III, the  $\sigma_{sp}$  values are nearly the same during the period 1.3-1.54 UTC (Figure 29e) which is similar to Case I. Subsequently, the spectral dependence increased for the duration of the sampling period (1.54-1.77 UTC) in a similar fashion to Case II. The mean  $AE_{neph}$  values were  $0.40 \pm 0.36$  for Case III and  $0.60 \pm 0.29$  for Case IV. Note that these values were less than Case II. Case III and Case IV mean  $\delta\alpha$  values were  $-0.25 \pm 0.97$  and  $-0.23 \pm 0.89$ , respectively. The large variability likely indicated a mixture of coarse and fine mode aerosols within both dust events. Case

IV had a strong spectral dependence throughout the time interval though not as strong in magnitude as Case II (Figure 29g). Case IV had a larger  $AE_{\text{neph}}$  mean value as compared to Case III (Figure 29h) which suggests a stronger fine mode aerosol influence but again, not as much as Case II.

Table 5. A summary of the physical and optical properties of the four selected Asian dust events intercepted by the DC-8 aircraft. Nephelometer measurements provided  $AE_{\text{neph}}$  and  $\delta\alpha$  while the plume remarks summarize the probable aerosol plume characteristics. The standard deviations are included to show the variability of particle size.

Case	Mean ( $\sigma$ ) $AE_{\text{neph}}$	Mean ( $\sigma$ ) $\delta\alpha$	Aerosol plume remarks
I	0.46 (0.63)	-0.49 (1.61)	strong dust plume
II	1.53 (0.23)	-0.31 (0.63)	strong pollution plume
III	0.40 (0.36)	-0.25 (0.97)	mixture of strong dust and pollution
IV	0.60 (0.29)	-0.23 (0.89)	mixture of strong dust and pollution

To further track these four cases back to their origin regions, the HYSPLIT backward trajectory model was used at three different altitudes: 3 km, 5 km, and 7 km (Draxler et al. 2003). According to Qiu and Sun (1994), aerosol particles can be transported eastward from China to the Pacific Ocean in the 2 to 7 km height range, and this is the reason to choose these three altitudes in this study. Figure 22 shows the back-trajectory analysis of the selected four cases (using the 5 km (blue) trajectory line as a proxy for plume altitude). Key points describing the similarities and differences from the model output include: (a) for Cases I and III, the dust plumes originated from the Gobi desert, and (b) for Cases II and IV, the dust plumes originated from the Taklamakan desert. The transport time of dust plumes for the four cases are around 7.5, 8, 5, and 7 days, respectively, to reach the remote Pacific regions where the dust plumes were

observed by the DC-8 aircraft. However, the transport time was only approximated because the measurements were not taken at the same location. From previous studies, the dust plumes normally take, on average, seven to ten days to move out of the Gobi desert area to the United States. Therefore, the model outputs are 240 hours in duration in order to explore all possible sources of the air masses.

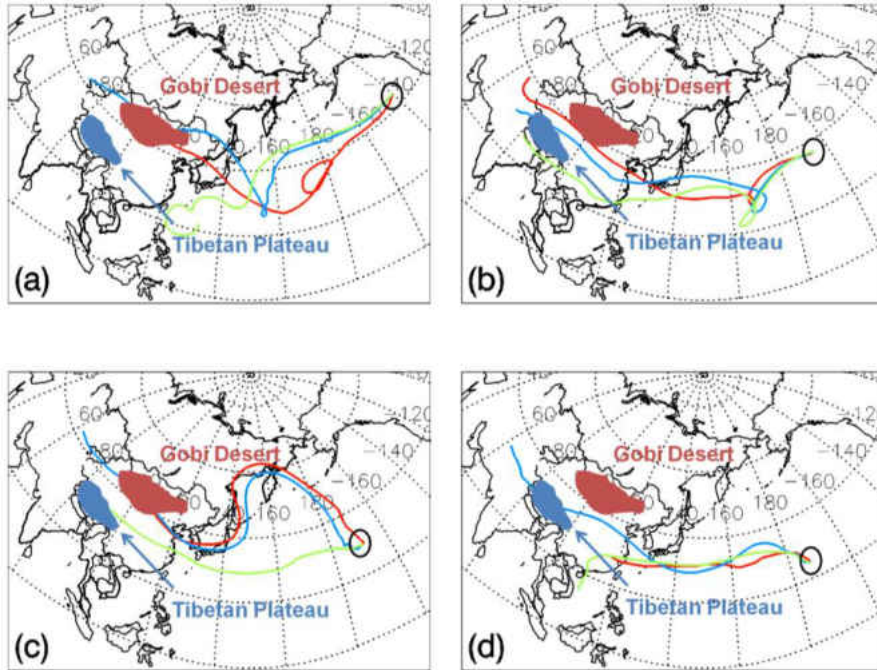


Figure 30. The NOAA HYSPLIT backward trajectories of dust plumes intercepted by DC-8 aircraft (denoted by black circles) over the remote Pacific Ocean for (a) Case I (2100 UTC 17 April 2006), (b) Case II (0300 UTC 24 April 2006), (c) Case III (0200 UTC 29 April 2006), and (d) Case IV (0400 UTC 29 April 2006). The heights of the dust plumes used in the analysis, 3000 m (red line), 5000 m (blue line), and 7000 m (green line), represent the range of heights of the dust plume intercepted by the DC-8 aircraft.

For Case I, the center height of the dust plumes is around 5 km, ranging from 3 to 7 km (Figure 28a). From the back trajectory analysis, the blue and red lines (Figure 30a) likely originated from the Gobi desert area and did not pass over many highly polluted areas. Whereas for Case II, the dust and pollution plume was located around 5-7 km and sampled by DC-8 at roughly 7 km (Figures 28b and 30b). The back trajectory showed

that the green and blue lines likely originated from the Taklamakan desert and passed through several highly polluted areas. Therefore, the outputs of the back trajectory model did support the findings from DC-8 measurements in Cases I (coarse mode) and II (fine mode).

For Cases III and IV, the green and blue lines likely originated from central China, and the data suggested a possible scenario of air masses containing dust plumes that were lifted above the boundary layer and passed through many urban areas (Figures 30c and 30d). Trajectories that cross paths over either the Gobi or Taklamakan Deserts are also scrutinized in order to see how pollution and dust can co-mingle at various points during their transpacific transport. By using  $\sigma_{sp}$ ,  $AE_{neph}$ ,  $\delta\alpha$ , and HYSPLIT trajectory analysis, the Logan et al. (2010) study was able to conclude that Asian aerosol plumes were dominated by dust, pollution, and complex mixtures during transport. An additional study investigates biomass burning aerosol properties during transport using ground-based AERONET retrievals in North America.

### **Biomass Burning Aerosol Transport over the Northern Great Plains**

Dry conditions during an exceptionally mild winter and warm spring led to an outbreak of wildfires in many areas of North America including the intermountain west and Pacific states in the United States. Over 5 million acres nationwide had been burned in the first nine months of 2012 (<http://www.nifc.gov/fireInfo/nfn.htm>). As a result of the fires, numerous smoke plumes were observed several hundreds to thousands of kilometers away from their combustion sources and also affected the air quality in the areas along the transport route (EPA, [www.airnow.gov](http://www.airnow.gov)). In late June, biomass smoke plumes were observed in the northern Great Plains region by the newly installed Grand

Forks Aerosol Robotic Network (AERONET) site. Before the installation of this site (October 2011), there were few active ground-based observation stations between the intermountain west and the eastern United States.

**Biomass smoke plume transport.** Figure 31 shows a time series of hourly AERONET retrieved  $AOD_{440}$  over the Grand Forks AERONET site (47.91°N, 97.32°W) during the warm season of 2012. Each peak in  $AOD_{440}$  is followed by a sharp decrease which denotes the passage of a cold front (shift in wind direction from southerly to westerly) or low pressure system that removed much of the smoke from the area (i.e., clouds or precipitation). This pattern repeated itself throughout the summer and early autumn until the fires were eventually extinguished. This study selects six instances where  $AOD_{440}$  is greater than 0.4 to represent a strong biomass burning event. In addition,  $AAOD$  and  $\omega_{\text{obs}}$  values are usually retrieved under this condition ( $AOD_{440} > 0.4$ ).

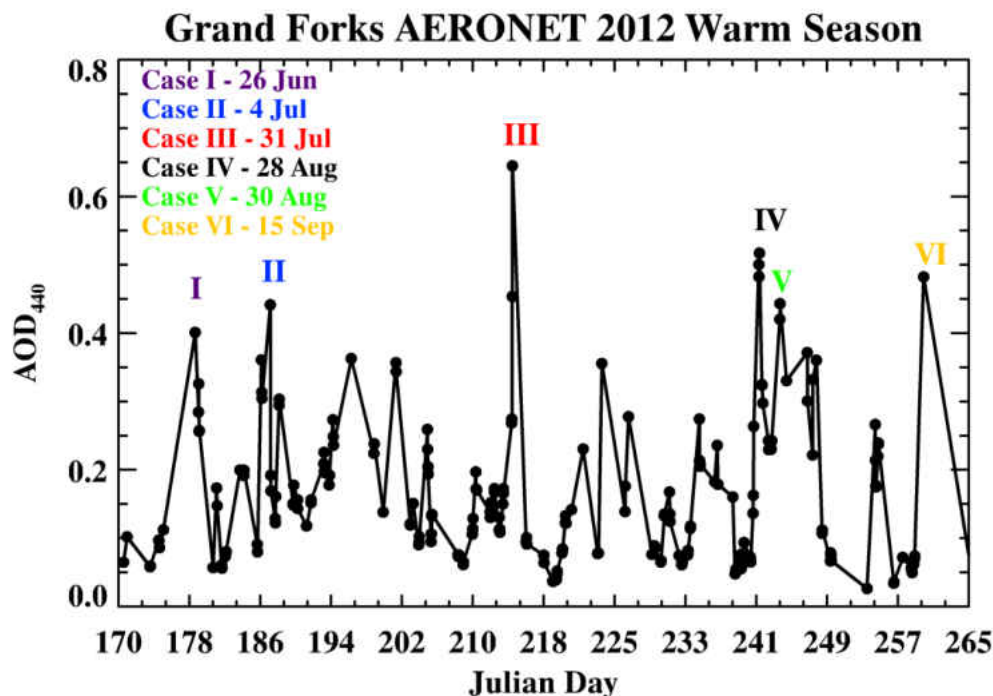


Figure 31. Aerosol loading of smoke plumes as evidenced by the periodic increase and decrease of the hourly aerosol optical depth (AOD) observed by the newly installed Grand Forks AERONET site (47.91°N, 97.32°W). Each case is color coded and this convention is used in the subsequent figures.

To identify the source regions of the six selected cases in Figure 31, the HYSPLIT backward trajectory model was used to track the origins of the smoke plumes (Figure 32). The locations of major fires along their trajectory routes were also displayed. In general, the backward trajectories revealed source regions in three parts of the United States: the intermountain west states (Colorado and Wyoming), northern Rockies (Montana and Idaho), and the Pacific states (Washington, Oregon, and California). Note that fires located outside of the trajectory path generated smoke plumes which were eventually advected in the general direction of the Grand Forks AERONET site.

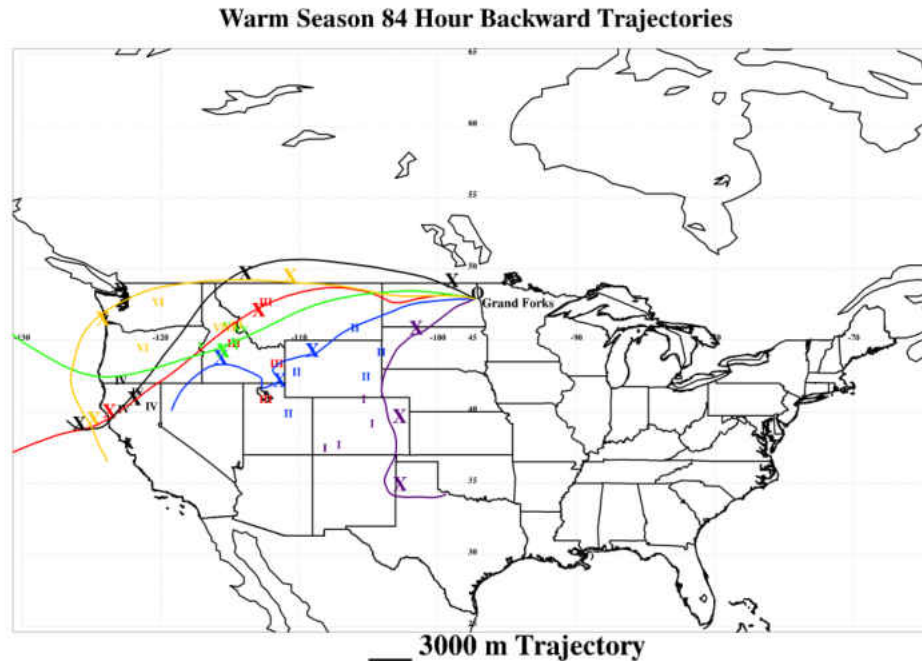


Figure 32. HYSPLIT backward trajectories of the six cases (with the same color code as Fig. 30). The “X” characters represent a 24 hour time segment of the backward trajectory that was initialized at the time of maximum aerosol loading ( $AOD_{440}$  maximum). The locations of the wildfires (Roman numerals color coded by case) are identified by MODIS Aqua/Terra satellite fire products (<http://earthdata.nasa.gov/data/near-real-time-data/data/hazards-and-disasters/fires>).

Based on archived meteorological observations and model data, high pressure ridges were determined as the primary processes responsible for transporting the smoke plumes ([www.esrl.noaa.gov/psd/data/composites/day/](http://www.esrl.noaa.gov/psd/data/composites/day/)). The trajectories are marked every 24 hours in order to show the temporal movement of the smoke plumes from the source regions to Grand Forks. Cases II, III, and V had the fastest transport times ( $\leq 1$  day). Case VI had a transport time of nearly 36 hours while Cases I and IV had the slowest transport times that approached 3 days. Note that any smoke plumes within the periphery of the ridge traveled faster than those smoke plumes that were closer to the center of the high pressure.

Figure 33 is generated by the Navy Aerosol Analysis and Prediction System (NAAPS) model. Figures 33a, b, and c show the locations of the wildfire source regions for Cases III, V, and VI while Figures 33d, e, and f show evidence of the smoke plumes over Grand Forks. Note that northern and eastern transport from the source regions is evident in these case examples. Case III exhibited vastly different optical properties from the other cases and will be further discussed in the next section.

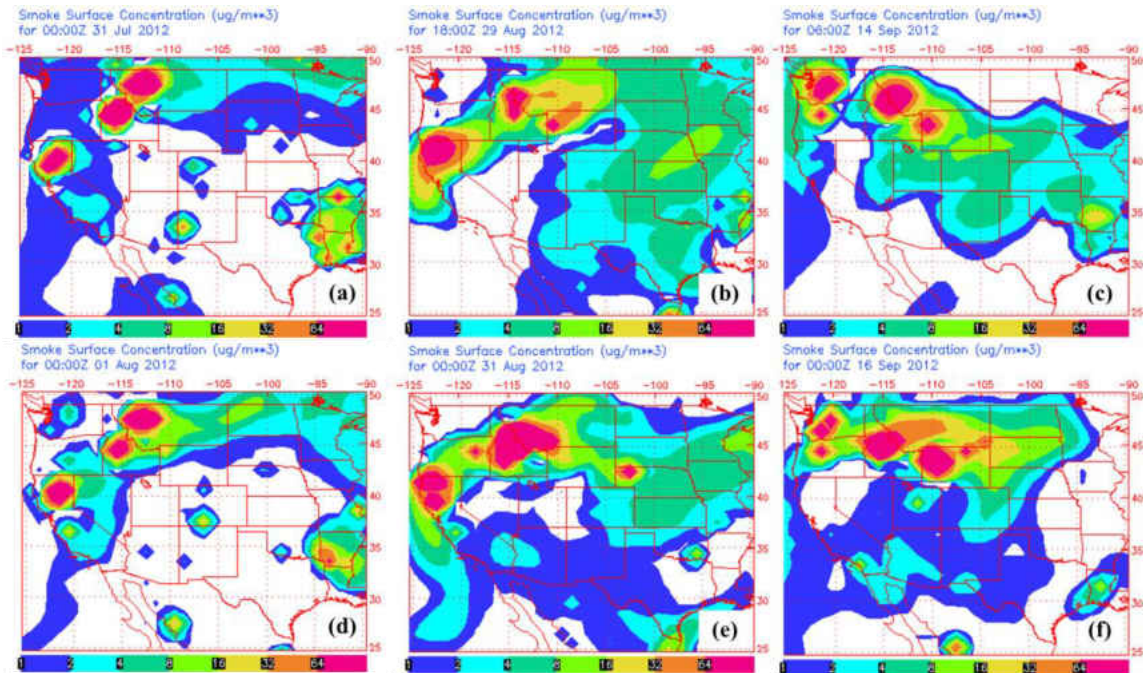


Figure 33. Navy Aerosol Analysis and Prediction System (NAAPS) model output (<http://www.nrlmry.navy.mil/aerosol/>) showing the locations of the wildfire source regions (dark red regions) for Cases (a) III, (b) V, and (c) VI while (d), (e), and (f) show the smoke plumes for the respective cases over Grand Forks (black circle). A transport pathway can clearly be seen from the hotspots to Grand Forks with decreasing smoke concentration.

**Biomass smoke plume optical properties.** Figure 34a shows the daily mean particle volume size distribution ( $dV/d\ln R$ ) for the six cases. The fine mode dominated the  $dV/d\ln R$  for all cases. Case II had the strongest fine mode influence while Case VI had the strongest coarse mode influence. It is likely that the smoke aerosols had

undergone some degree of coagulation and/or hygroscopic growth during transport since all cases exhibited a bimodal distribution. In Figure 34b, the AOD spectral variations fit the general range of biomass burning aerosols (Chung et al. 2012; Logan et al. 2013a). For example, Case V had the strongest AOD spectral dependence and therefore the highest AE value (1.98) while Cases I and VI had the weakest dependence with lower values of 1.54 and 1.55, respectively.

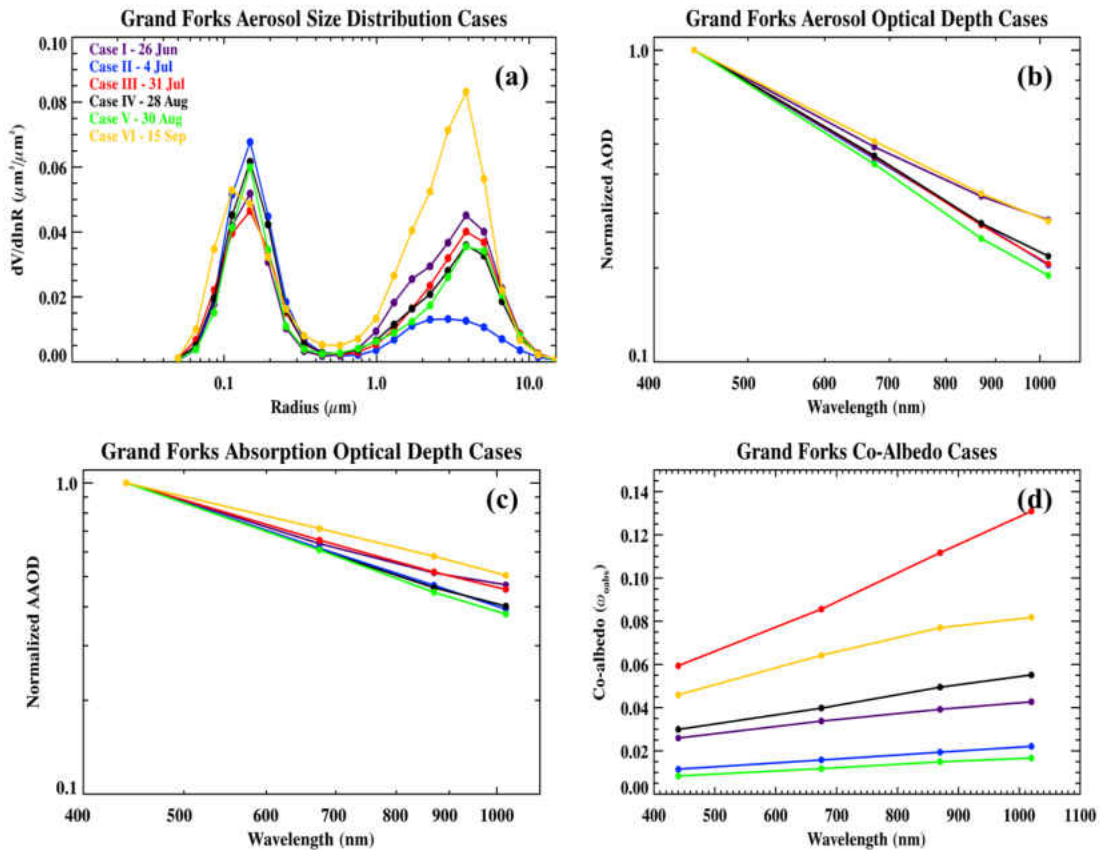


Figure 34. Daily mean AERONET retrieved (a) particle volume size distributions and the spectral dependences of (b) AOD, (c) AAOD, and (d)  $\omega_{\text{obs}}$  for the six selected cases.

**Biomass smoke plume physico-chemical properties.** Figures 34c and 34d show the daily mean spectral dependences of AAOD and  $\omega_{\text{obs}}$ . All cases had a normalized AAOD dependence of 0.4-0.5 which is typical for biomass burning aerosols (Chung et al. 2012; Logan et al. 2013a). Similar to Figure 34b, Case VI had the weakest AAOD

spectral dependence while Case V had the strongest. Case VI was previously identified as having a strong coarse mode influence. The larger particles tended to scatter more than they absorb (especially at the longer wavelengths), thus the weaker AAOD spectral dependence. Cases I and III had relatively weak spectral dependences that could also be attributed to their strong coarse mode contributions. Conversely, Cases II, IV, and V had the stronger AAOD spectral dependences since the fine mode particles in turn exhibited more absorption at the longer wavelengths due to their smaller size.

Black carbon (BC) is responsible for much of the absorption across all wavelengths (visible to near IR) in the smoke particles and mixtures of BC and organic carbon (OC) can be inferred by the spectral dependence in  $\omega_{\text{obs}}$ . Figure 34d shows that Case V had the lowest overall  $\omega_{\text{obs}}$  values, suggesting that though the fine mode particles have a large degree of extrinsic absorption, the mixture of carbonaceous compounds is weakly absorbing. However, the slight increase in spectral  $\omega_{\text{obs}}$  with wavelength can be attributed to BC particle influences. Since this plume arrived at Grand Forks within 24 hours, the weak spectral dependence may be a result of smoke plumes that were generated from the low temperature “smoldering phase” (Reid et al. 1998; Martins et al. 1998b; Saleh et al. 2013). Case II consisted of a smoke plume with the strongest fine mode influence and had nearly the same  $\omega_{\text{obs}}$  values as Case V but with a smaller coarse mode influences. This suggested that a smaller amount of coagulation and/or hygroscopic growth may have occurred during transport for Case II.

Case III had the highest spectral  $\omega_{\text{obs}}$  values which increase with wavelength denoting strongly absorbing carbonaceous influences. The plume was generated by a fresh wildfire which would explain the large amount of absorption from BC particles

within the smoke (Martins et al. 1998b; Saleh et al. 2013). Case VI had the second highest spectral  $\omega_{\text{obs}}$  values that increase with increasing wavelength denoting strongly absorbing BC in addition to having a strong coarse mode influence. This is likely a result of the combination of fresh smoke from the Pacific Northwest wildfires (WA and OR) and smoke from ongoing fires in central Idaho (since early August).

Cases I and IV had smoke plumes that took the longest time to advect from their source regions to Grand Forks (~3 days). Both cases featured moderate overall  $\omega_{\text{obs}}$  spectral dependences with Case I having a slightly lower absorption. This also correlated with the stronger coarse mode influence than Case IV possibly indicating that more coagulation may have taken place during transport in Case I than Case IV. It should be noted that given the time it took for the smoke plumes to reach Grand Forks, some conversion of strongly to weakly absorbing organic carbon may have taken place in both cases. A summary of the aerosol optical properties and transport times for the six cases are in Table 6.

These results suggested that the observed AAOD and  $\omega_{\text{obs}}$  values at Grand Forks did depend on the transport pathways of biomass smoke from their source regions to Grand Forks because these smoke particles likely experienced physico-chemical interactions during transport. However, we do note that relating the exact contributions of black and organic carbon (BC and OC) constituents to the spectral dependences of AAOD and  $\omega_{\text{obs}}$  can be difficult if not impossible to determine solely from AERONET or any platform that does not involve chemical spectroscopy (e.g., thermal denuder, mass spectrometer, etc.). This issue is complicated even further by the fact that smoke particles from the flaming combustion phase can have vastly different physico-chemical

properties than particles from the smoldering phase. However, previous studies have reported the relative black and organic carbon proportions of smoke plumes from moments after pyrolysis to hours and days during transport and concluded: (a) absorption of the smoke particles does decrease over time and (b) the flaming combustion phase produces more strongly absorbing organic compounds than the smoldering phase (Martins et al. 1998a, b; Reid et al. 1998; Lewis et al. 2008; Mack et al. 2010; Corr et al. 2012; Saleh et al. 2013).

Table 6. A summary of the mean AOD, AE, and AAE values for the six cases. Daily AERONET data is used except for the maximum AOD<sub>440</sub> values. The number of almucantar retrievals is represented by N.

2012 Warm Season Cases	Mean AOD <sub>440</sub>	Maximum AOD <sub>440</sub> <sup>a</sup>	N <sup>a</sup>	AE	AAE	$\omega_{\text{oabs440}}$ <sup>b</sup>	Transport Time
I 26 June	0.31	0.40	5	1.54	1.16	0.97	~ 3 days
II 4 July	0.27	0.44	3	1.82	1.15	0.99	< 1 day
III 31 July	0.41	0.64	4	1.81	1.07	0.94	< 1 day
IV 28 August	0.41	0.52	6	1.83	1.13	0.97	~ 3 days
V 30 August	0.43	0.44	2	1.98	1.14	0.99	< 1 day
VI 15 September	0.48	0.48	1	1.55	0.79	0.95	1.5 days

<sup>a</sup> Retrieved from AERONET hourly data.

<sup>b</sup> There are 3 or fewer  $\omega_{\text{oabs}}$  almucantar retrievals for each case.

**Biomass smoke plume radiative properties.** Aerosol Radiative Forcing (ARF) is related to the amount of shortwave flux absorbed at the surface (SFC) during both clean and aerosol laden periods and is given by the equation:

$$\text{ARF}_{\text{SFC}} = \Delta F_{\text{a}} - \Delta F_{\text{c}}, \quad (10)$$

where  $\Delta F_{\text{a}}$  and  $\Delta F_{\text{c}}$  represent the difference in broadband shortwave flux (downward and upward) calculated with and without aerosols, respectively (e.g., García et al. 2012). The  $\Delta F_{\text{c}}$  values are typically greater than  $-10 \text{ W m}^{-2}$ , whereas most of the  $\Delta F_{\text{a}}$  values denoting aerosol laden conditions are much less than  $-10 \text{ W m}^{-2}$ . The strongly negative ARF values generally associate with high  $\text{AOD}_{440}$  values.

Table 7 lists the  $\Delta F_{\text{a}}$  values for the six selected cases, the  $\Delta F_{\text{c}}$  values prior to and after the passage of the observed smoke haze events, and their corresponding ARF values. Cases III, IV, and VI had ARF values of  $-44.3$ ,  $-42.8$ , and  $-39.3 \text{ W m}^{-2}$ , respectively. These were the most negative values throughout the entire warm season for all smoke events ( $\text{AOD}_{440} > 0.2$ ) as observed by the Grand Forks AERONET facility. Note that these three cases also had the highest spectral  $\omega_{\text{oabs}}$  dependence of the six cases. This suggests a correlation between the absorptive capacities of these aerosols in that the carbonaceous compounds strongly absorb incoming shortwave radiation which can lead to more of a cooling effect at the surface.

The sensitivity of ARF to AOD or aerosol radiative forcing efficiency ( $\text{ARF}_{\text{eff}}$ ) is an important parameter in discerning the radiative impacts of specific aerosol types on the atmosphere (Ge et al. 2010; García et al. 2012; Logan et al. 2013b). It is the ratio ARF to AOD and can be calculated at levels representing either the bottom or top of the atmosphere (Dubovik et al. 2006; García et al. 2012). The  $\text{ARF}_{\text{eff}}$  parameter does not

take into account aerosol loading such that the absorptive properties of aerosols become more evident (García et al. 2012). This study uses surface  $ARF_{eff}$  to quantify the large magnitude of ARF between the smoke plume height and at the surface (Li et al. 2007; García et al. 2012).

Table 7 summarizes the  $ARF_{eff}$  values for each case. All cases showed a general increase in  $ARF_{eff}$  as the smoke plumes passed over the AERONET site. Case III had the largest  $ARF_{eff}$  value of  $-117.6 \text{ W m}^{-2} \text{ AOD}^{-1}$ , indicating that the Case III aerosols had a pronounced warming effect aloft. Again, the spectral  $\omega_{obs}$  dependence supported this claim since Case III aerosols had a stronger spectral dependence than all other cases suggesting that these aerosols were likely a result of the high temperature flaming combustion phase. The other cases did not have the same relationship between  $ARF_{eff}$  and  $\omega_{obs}$  which suggested complex mixtures of carbonaceous aerosols generated by both flaming/smoldering combustion phases.

Table 7. Hourly retrievals of aerosol radiative forcing (ARF) and aerosol radiative forcing efficiencies (ARF<sub>eff</sub>) at the surface for the six selected cases. Clean Day represents mean  $\Delta F_c$  values corresponding to AOD<sub>440</sub> values less than 0.2 prior to and after the smoke event cases. Smoke Event values correspond to maximum AOD<sub>440</sub> values. Note that Cases IV and V represent a prolonged smoke event with different radiative properties.

Case	Clean Day $\Delta F_c$ (W m <sup>-2</sup> )	Smoke Event $\Delta F_a$ (W m <sup>-2</sup> )	ARF $\Delta F_a - \Delta F_c$	ARF <sub>eff</sub> (W m <sup>-2</sup> AOD <sup>-1</sup> )	Event Duration
I 26 June	-8.4	-38.2	-29.8	-140.3	6 days
II 4 July	-8.5	-37.7	-29.2	-128.9	2 days <sup>a</sup>
III 31 July	-7.0	-51.0	-44.3	-117.6	6 days
IV 28 August	-6.7	-49.5	-42.8	-140.7	9 days
V 30 August	-6.7	-39.8	-33.1	-135.1	7 days
VI 15 September	-6.9	-46.2	-39.3	-135.7	7 days

<sup>a</sup> Persistent light haze was observed for nearly two weeks from late June to mid-July.

### **SQ3: What Are the Impacts of Aerosol Properties On Marine Boundary Layer Cloud Condensation Nuclei Number Concentration?**

#### **Seasonal Aerosol Properties over the Azores**

Figures 35a, b, and c show the seasonal mean aerosol loading (AOD) and size ( $AE_{AOD}$ ) retrieved from AERONET in addition to surface (10 m) wind speed from AOS measurements. Mean AOD values during the winter were close to the yearly mean as there were few outside aerosol sources. However, the low  $AE_{AOD}$  values ( $< 0.75$ ) further demonstrated that coarse mode aerosols were dominant during this season due to the prevalence of low pressure systems over the Azores (Dong et al. 2014). In addition, the winter months had the highest mean surface wind speed ( $6.7 \text{ m s}^{-1}$ ) which resulted in a large amount of sea salt aerosol generation (Yoon et al. 2007). During the spring, strong surface wind speeds ( $5.5 \text{ m s}^{-1}$ ) continuously generated sea salt while continental fine mode aerosols began to assert their influences as illustrated in Figure 35b where  $AE_{AOD}$  values increased from 0.55 in March to 0.95 in May. The large standard deviations in both AOD and  $AE_{AOD}$  also suggested a large variability in aerosol loading, size, and composition primarily due to weather patterns of varying intensity and track (Yoon et al. 2007; Yu et al. 2009).

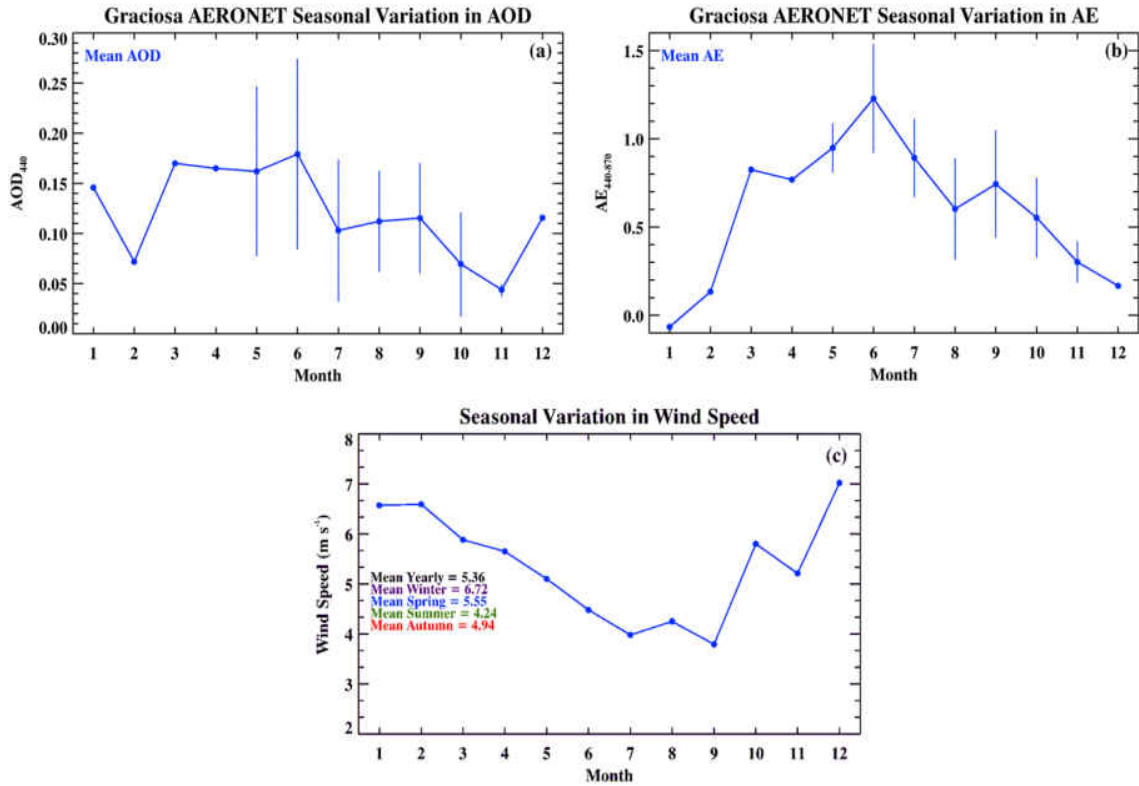


Figure 35. Monthly mean and standard deviation of Graciosa AERONET retrieved (a) AOD, (b) AE, and (c) AMF-Azores mean wind speeds during CAP-MBL. For (a) and (b), only the months with statistical significance ( $> 10$  hours of retrievals) are shown the monthly mean  $\pm 1\sigma$ .

Note that the maximum  $AE_{AOD}$  and diminished surface wind speed in June indicated that the fine mode continental aerosols contributed significantly to AOD. From July to September, nearly constant, lower values of AOD ( $\sim 0.12$ ), moderate  $AE_{AOD}$  ( $\sim 0.7$ ), and minimum surface wind speed ( $\sim 4 \text{ m s}^{-1}$ ) indicated a mixture of continental aerosols and sea salt with the lowest coarse mode influence to AOD occurring during this period. This was likely due to favorable weather patterns such as the Azores High (summer season) and mid-latitude cyclones that advected various continental aerosols over this region (Owen et al. 2006; Yu et al. 2009; Wood et al. 2014). With decreasing  $AE_{AOD}$  and increasing surface wind speed during the autumn months, the contribution of sea salt to AOD likely became more dominant from October to December.

Figure 36 shows the mean (standard deviation) yearly and seasonal aerosol particle volume ( $dV/d\ln R$ ) and number ( $dN/d\ln R$ ) size distributions, AOD, and  $AE_{AOD}$  during the CAP-MBL campaign. A low overall mean  $AOD_{440}$  of 0.12 denoted a clean environment over this region. The eastern Atlantic Ocean is typically dominated by coarse mode MBL sea salt, though influences from mineral dust aerosols cannot be ruled out due to episodic intrusions of western African aerosols. In terms of aerosol volume, a bimodal signal was prominent where the coarse mode influence ( $r \geq 1 \mu\text{m}$ ) dominated that of the fine mode ( $r < 1 \mu\text{m}$ ) throughout the year. In the case of the yearly number size distribution, the fine mode was nearly the same magnitude as the coarse mode due to continental aerosol influences during the spring and summer seasons. The coarse mode aerosols (e.g., sea salt) dominated the volume and number size distributions during the winter and spring months. However, weather patterns begin to advect continental aerosols during the spring months over the Azores region as evidenced by the larger fine mode number concentration.

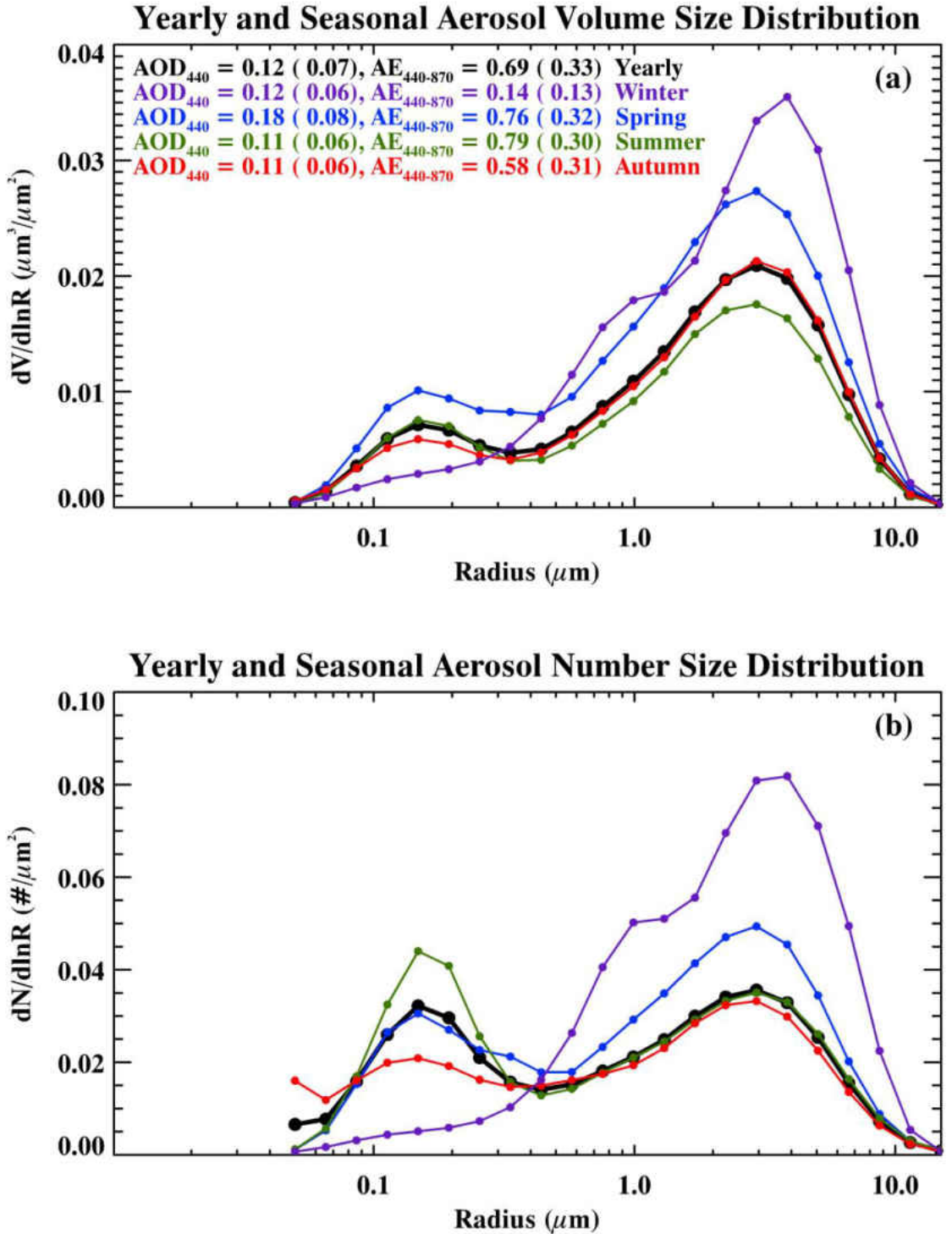


Figure 36. AERONET retrieved yearly and seasonal mean aerosol (a) volume and (b) number size distributions. The mean (standard deviation) aerosol optical depth (AOD) and Angström exponent ( $AE_{AOD}$ ) are also included.

Note that the summer season had the lowest coarse mode volume influence as well as the highest fine mode number contribution primarily due to a combination of the low surface winds and an influx of pollution aerosols from the Americas (Yoon et al. 2007). The fine mode (coarse mode) contribution decreased (increased) during the autumn months as supported by the decreasing trend in  $AE_{AOD}$  (Figure 35b). This is likely a result of maritime cyclones that create stronger winds at the surface thereby generating more sea salt over the Azores (Yoon et al. 2007; Wood et al. 2014).

### **Aerosol Properties of the Six Selected Cases and their Impacts on MBL $N_{CCN}$**

In addition to the yearly and seasonal means, six aerosol events have been selected from the warm season months (May-September) to investigate continental aerosol properties during transport as well as their influences on MBL  $N_{CCN}$ . The cases consist of mineral dust, pollution, biomass smoke, and volcanic ash particles that have aerosol loading at least greater than twice the overall mean AOD over the region ( $AOD_{440} \geq 0.25$ ). Figure 37 shows the volume and number size distributions as well as the AOD spectral dependences of the five selected cases (Cases I-V) plus an additional case (23 June 2010). Note that the 23 June 2010 case had no AOS observations and therefore only the AERONET retrievals for this event will be discussed in comparison with the other cases.

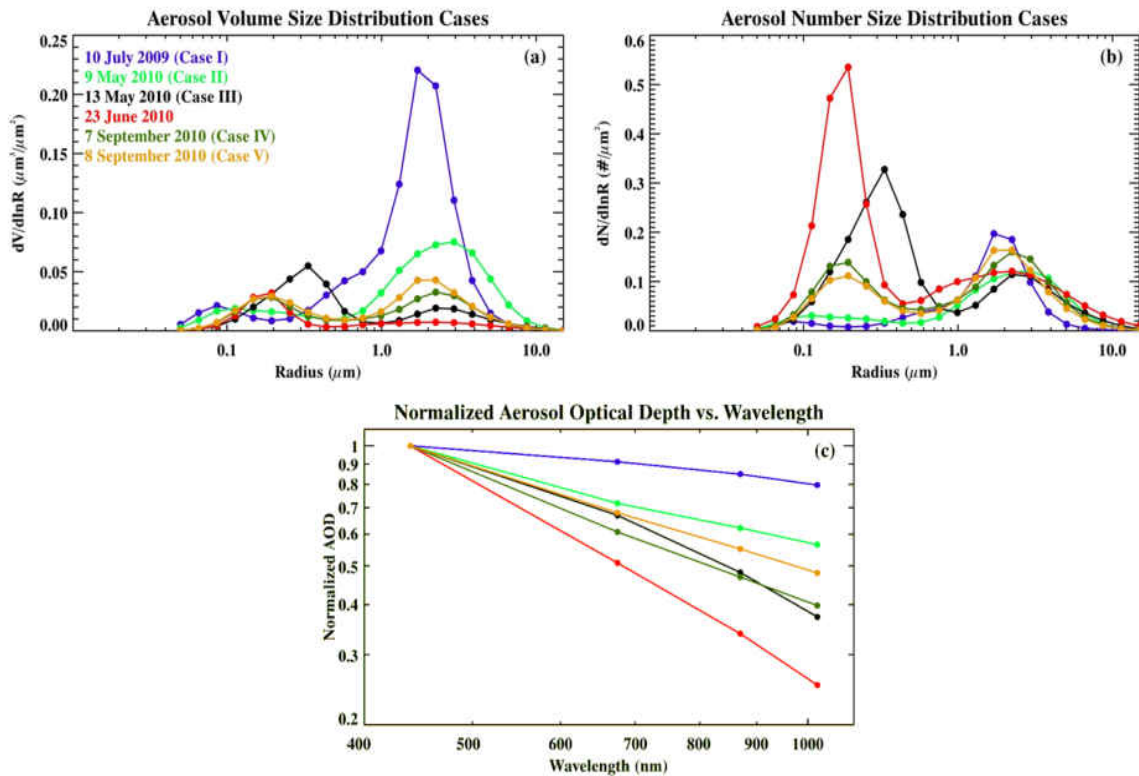


Figure 37. AERONET retrieved (a) volume and (b) number size distributions as well as the (c) spectral dependences for the five selected cases. The 23 June 2010 case (in red) is shown for comparison purposes and is briefly discussed in this study due to a lack of AMF-Azores Aerosol Observation System (AOS) measurements for this day.

Similar to Figure 36, all cases exhibited bimodal volume and number size distributions with strong coarse mode contributions for Cases I (10 July 2009) and II (9 May 2010). Case III (13 May 2010) and the 23 June 2010 case had the strongest fine mode contribution with little coarse mode influence. Cases IV (7 September 2010) and V (8 September 2010) had fine and coarse mode contributions that were nearly equal.

In terms of the aerosol optical properties of the selected cases, Case I had the weakest spectral AOD dependence of all cases with a low  $AE_{AOD}$  value of 0.25 denoting a strong coarse mode influence while the 23 June 2010 case had the strongest spectral dependence with an  $AE_{AOD}$  of 1.61 (strong fine mode influence). Case II had the second

lowest  $AE_{AOD}$  value of 0.71 followed by Case V with an  $AE_{AOD}$  of 0.89 indicating moderate coarse mode aerosol influences. In contrast, Cases III and IV had higher  $AE_{AOD}$  values of 1.08 and 1.13, respectively, indicating fine mode influences. However, without further information of their absorptive properties, it is difficult to classify the aerosols solely based on their size.

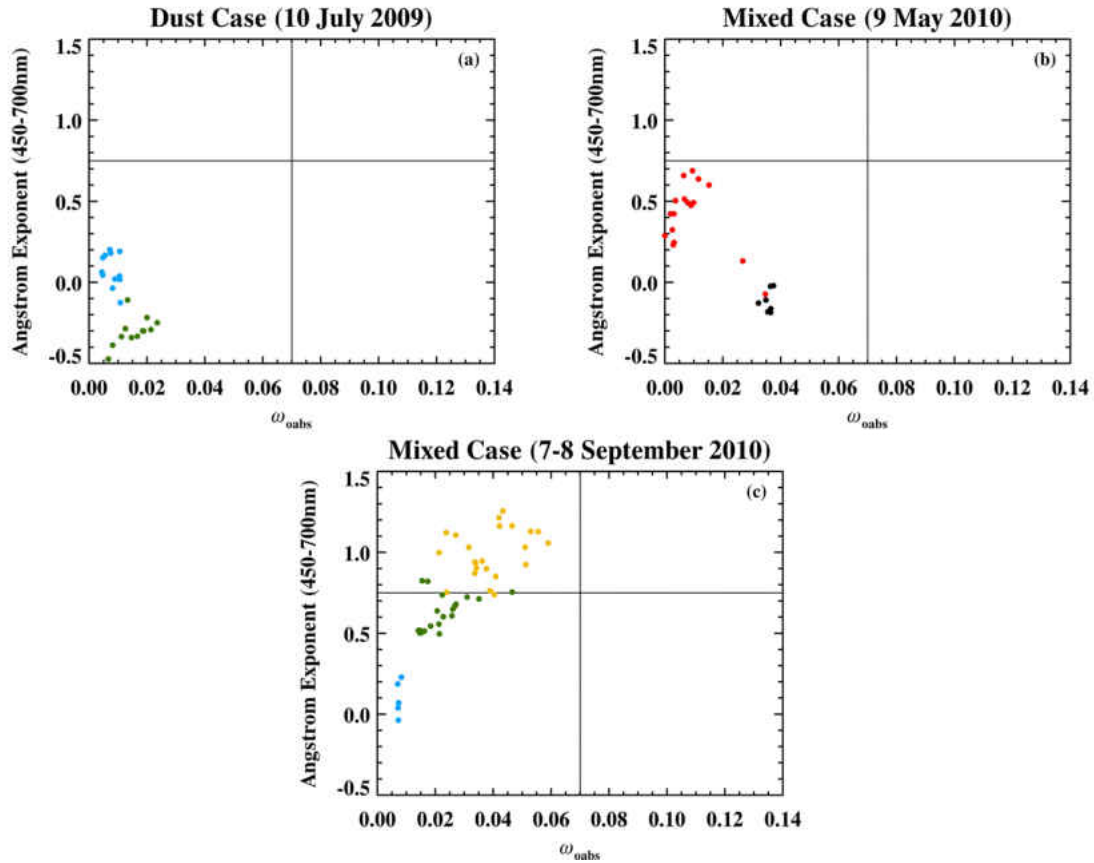


Figure 38. Cases I, II, IV, and V AOS measured aerosol properties as classified by the Logan et al. (2013a) method:  $AE_{neph} > 0.75$  ( $< 0.75$ ) for fine (coarse) mode, and  $\omega_{obs} < 0.07$  ( $> 0.07$ ) for weak (strong) absorption. The colors denote sea salt (blue), mineral dust (green), volcanic ash (red), pollution (gold), and unclassified (black) aerosols. No absorption data exists for Case III (13 May 2010).

Figure 38 shows the aerosol properties from four of the five selected cases classified by the Logan et al. (2013a) method where  $AE_{neph} > 0.75$  ( $< 0.75$ ) was used to denote fine (coarse) mode aerosols while  $\omega_{obs} < 0.07$  ( $> 0.07$ ) denoted weak (strong)

absorption. Note that Case III had no PSAP  $\sigma_{ap}$  absorption measurements and therefore no  $\omega_{obs}$  values. The aerosol types are color sorted according to nephelometer measurements of  $\sigma_{sp}$  as the aerosol plumes pass through the Azores region. In other words, the sharp increase of  $\sigma_{sp}$  from much lower baseline values denotes an aerosol intrusion episode. Figure 39 shows probable plume source regions using HYSPLIT backtrajectory model output (Draxler and Rolph 2012; Rolph 2012). An altitude of 1.5 km was chosen for the trajectories as this was the typical cloud-top height of the MBL clouds over the Azores (Rémillard et al. 2012; Dong et al. 2014). Here, aerosols aloft can either interact with MBL clouds directly or be transported to the surface by turbulence or subsidence where they can affect  $N_{CCN}$ .

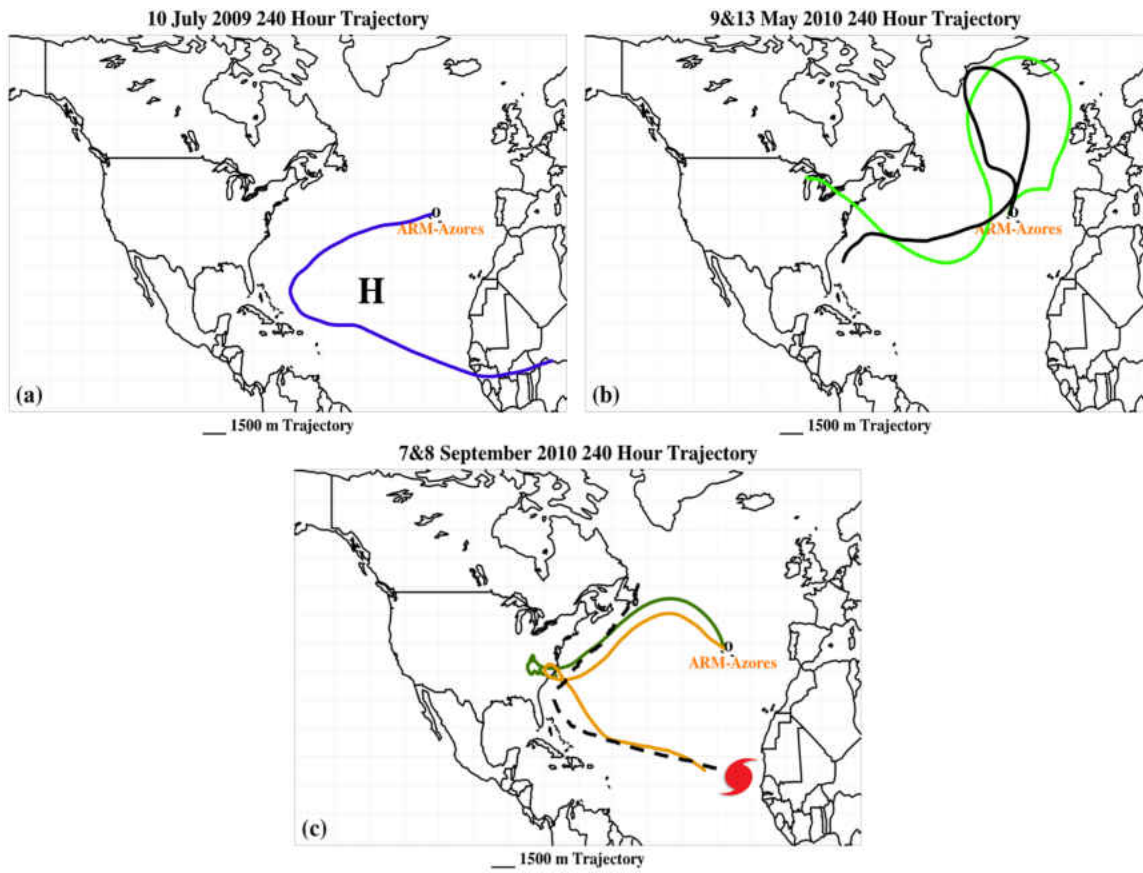


Figure 39. HYSPLIT backward trajectories at 1.5-km level (solid lines) for the five selected cases. (a) Purple line – Saharan mineral dust transported by a strong Azores High pressure system, (b) light green line – volcanic ash from a recent Eyjafjallajökull eruption (6 May 2010); black line – biomass smoke from Central and North America along with urban/industrial pollution were advected to the Azores, and (c) urban/industrial pollution and smoke from North America the eastern United States as well as Saharan dust courtesy of Hurricane Earl (storm track outlined with dashed line) were all advected to the Azores (dark green and gold lines).

For Case I, both sea salt and mineral dust were identified with the mineral dust being coarser and more absorbing than the sea salt (Figure 38a). A high pressure system (Azores High) was likely responsible for transporting Saharan dust around its periphery to the Azores region (NOAA NCEP/NCAR re-analysis: Kalnay et al. 1996; Owen et al. 2006; Dong et al. 2014). The dust particles remained in the supermicron coarse mode likely due to a lack of wet scavenging by clouds along the transport route. Though it was possible that some North American aerosols (e.g., pollution) may have been present

within this plume, the trajectory did not pass very close to the mainland of the United States (Figure 39a).

Figure 38b points out a cluster of weakly absorbing, coarse mode aerosols similar to sea salt. However, these aerosols had stronger  $\sigma_{sp}$  and  $\sigma_{ap}$  spectral dependences compared to sea salt (Figure 40). The trajectory for this case in Figure 39b showed a path from North America through Iceland to the Azores. During the spring of 2010, volcanic activity was occurring in Iceland including confirmed eruptions of Eyjafjallajökull during 4-7 May 2010 (Seifert et al. 2011; Bingemer et al. 2012). In addition, re-analysis data (not shown) suggested that meteorological patterns during this period favored the southward transport of volcanic ash over Western Europe and the eastern remote Atlantic Ocean. Therefore, the particles were identified as volcanic aerosols which can mimic pollution (due to their sulfate content) and mineral dust aerosols (due to their coarse mode size) (Langmann 2013). The black colored aerosols were coarse mode, absorbing type and thus a likely mixture of aged volcanic ash and pollution. For Case III (Figure 39b), no eruptions were occurring within 48 hours prior to 13 May 2010 and winds were not favorable for any ash transport to the Azores. However, mixtures of biomass burning smoke from ongoing fires in Mexico and Central America and urban pollution from the eastern United States were transported to this area.

Figure 38c shows an interesting example of how mineral dust, pollution, and biomass burning aerosols can mix during transport. Saharan dust is rarely transported directly from Africa to the Azores. A tropical wave formed off the West African coast and developed into Hurricane Earl on 3 September 2010 (Figure 39c). Though the hurricane did not make landfall in North America, it did entrain a mixture of urban

pollution and possible biomass burning smoke exiting off the North American mainland. Pollution plumes were visible in Moderate Resolution Imaging Spectroradiometer (MODIS) satellite imagery (not shown) along with reports of fires in the southeast and central plains from the NOAA Hazard Mapping System (HMS) Fire and Smoke Product (<http://www.ospo.noaa.gov/Products/land/hms.html>). As the hurricane transitioned to an extratropical cyclone, it advected the aerosol mixture to the Azores over a two day event. Note how the mineral dust here is less coarse than in Case I due to cloud-processing and wet scavenging along the transport route. Hence, it is apparent that an a priori knowledge of aerosol type and transport is extremely important especially when modeling aerosol effects on cloud properties.

The AMF-Azores AOS was the primary platform to observe aerosol properties during the CAP-MBL campaign. A primary advantage for including retrievals from this platform is that the nephelometer and PSAP instruments can provide more continuous in situ measurements especially when there are no AERONET retrievals. This study assumes sufficient turbulence and subsidence within the boundary layer (e.g., updrafts and downdrafts) will mix aerosols down to the surface such that they can be observed by the AOS and AERONET platforms in real time.

Figure 40 shows the aerosol and CCN measurements for the five selected cases. The scattering and absorption coefficients ( $\sigma_{sp}$  and  $\sigma_{ap}$ ) are used as proxies for aerosol loading, size, and composition and are plotted at three wavelengths on the primary y-axis. The nephelometer-measured fine mode fraction (FMF) is the ratio of the scattering coefficient at 550 nm for 1  $\mu$ m, fine mode size particles ( $\sigma_{sp550fine}$ ) to total (fine and coarse) mode particles at the same wavelength ( $\sigma_{sp550total}$ ) and is plotted on the secondary

y-axis. The FMF parameter can illustrate the mode of aerosol that has a dominant influence of the physical properties of the aerosol plume (Anderson et al. 2003; Yu et al. 2009). Typically, FMF values less than 0.2 represent coarse mode particles such as mineral dust, values greater than 0.6 can represent fine mode particles (e.g., pollution and biomass burning aerosols), and intermediate values denote mixtures (Anderson et al. 2003; Yu et al. 2009). Hourly averaged  $\sigma_{sp}$ , FMF,  $\sigma_{ap}$ , and  $N_{CCN}$  presented in Figure 39 include not only the AERONET defined aerosol events (vertical purple lines) but also 24-48 hours before and after the passage of the plumes over the AMF-Azores site.

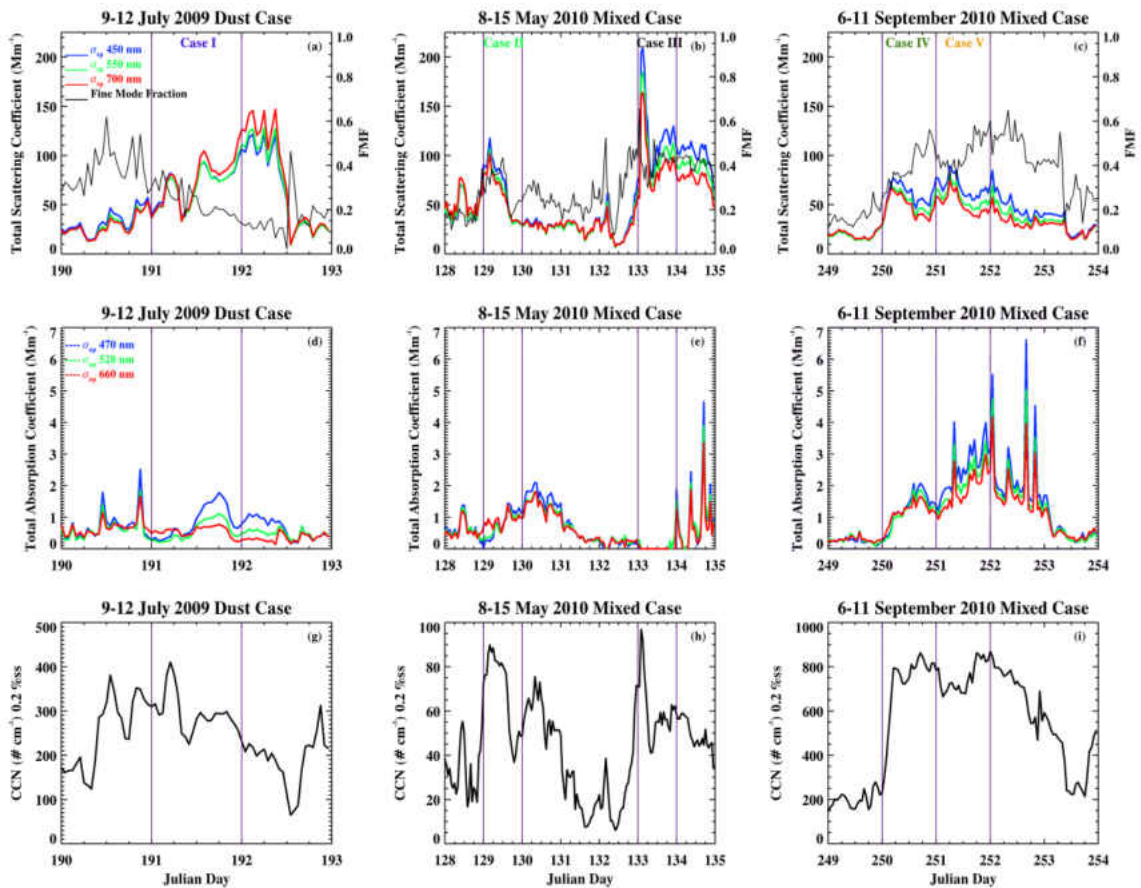


Figure 40. (a-c) Scattering coefficient ( $\sigma_{sp}$ ) and fine mode fraction (FMF), (d-f) absorption coefficient ( $\sigma_{ap}$ ), and (g-i) CCN from hourly averaged AMF-Azores AOS

observations. The AOS captured more of the aerosol events while the AERONET was only operational at certain time intervals for each case (vertical purple lines).

For Case I, the FMF values, ranging from 0.3 to 0.4 from 0000 UTC on 10 July to local noon, mainly indicated coarse mode aerosols. After local noon, there was a sharp rise in  $\sigma_{sp}$  with a corresponding decrease in FMF ( $< 0.2$ ) until local noon of the next day (11 July). The reversed spectral dependence of  $\sigma_{sp}$  with a corresponding daily mean  $AE_{neph}$  value of -0.11 also suggested the presence of supermicron, coarse mode aerosols (Logan et al. 2010). Particles that are exceptionally large ( $\gg 1 \mu m$ ) will scatter more in the longer wavelengths (red and near IR) as opposed to submicron particles that scatter more in the shorter wavelengths (UV and blue). Mineral dust tends to absorb greatly at the visible parts of the E-M spectrum (strong  $\sigma_{ap}$  spectral dependence) which contrasts with the less absorbing sea salt particles (weak  $\sigma_{ap}$  spectral dependence) whose presence was observed earlier in the day (Schuster et al. 2006; Chung et al. 2012; Logan et al. 2013a). There was also a strong correlation ( $r=0.83$ ) between the sea salt aerosols and  $N_{CCN}$  (Figure 41a). Sea salt aerosols can strongly activate as CCN due to their chemical content and hygroscopic nature. These aerosols are high in sodium chloride and sulfate concentration as a result of oceanic minerals and organisms, respectively.

The variation of  $N_{CCN}$  values was nearly the same as that of FMF during the three day period such that the  $N_{CCN}$  values fluctuated before local noon on 10 July, and then monotonically decreased until local noon of 11 July. In this case, there was a negative correlation (-0.5) with  $\sigma_{sp}$  which suggested an inverse relationship between the mineral dust particles (Figure 41b). This is likely due to factors such as insolubility of the dust particles and the size of the particles themselves (Karydis et al. 2011). These factors can lead to a general decrease in  $N_{CCN}$  since insoluble particles will weakly activate as CCN

while large size particles can adsorb more water vapor thereby raising the amount of supersaturation needed for activation (Karydis et al. 2011; Tao et al. 2012).

The late spring season cases, Cases II and III, had different types of aerosols and physical characteristics as shown in Figures 40b, e, and h. Case II showed a slight  $\sigma_{sp}$  spectral dependence with mean  $AE_{neph}$  of 0.26 and FMF of 0.3 which indicated coarse mode influences similar to Case I but having no reversal of spectral dependence. The magnitude of  $\sigma_{sp}$  increased to nearly  $110 \text{ Mm}^{-1}$  during the aerosol event then decreased after 1800 UTC to near background levels ( $\leq 30 \text{ Mm}^{-1}$ ). Figure 41c shows a strong correlation between  $\sigma_{sp}$  and  $N_{CCN}$  throughout the day ( $r=0.95$ ). The FMF rose to 0.43 then declined below 0.20 indicating a mixture of aerosols with a strong coarse mode contribution. Case III shared some physical characteristics of Case II (mixed aerosols) with large  $\sigma_{sp}$  values ( $\sim 200 \text{ Mm}^{-1}$ ) indicating more aerosol loading. However, it was influenced more by fine mode aerosols as evidenced by stronger  $\sigma_{sp}$  spectral dependence and greater FMF values ( $> 0.4$ ). The strong correlation between  $\sigma_{sp}$  and  $N_{CCN}$  ( $r=0.77$ ) indicated a strong ability for these aerosols to activate as CCN (Figure 41d).

The aerosols in Cases II and III were identified as volcanic ash and pollution particles, respectively. During volcanic eruptions, sulfur dioxide ( $\text{SO}_2$ ) can be emitted into the atmosphere and converted to aqueous sulfate ( $\text{SO}_4^{2-}$ ). The sulfate can either form secondary fine mode particles or condense onto and coat the coarse mode volcanic ash particles. In either case, both particle types will become strongly hygroscopic. Similarly,  $\text{SO}_2$  is a main pollutant emitted in urban/industrial regions. This pollutant can be converted into sulfate and mix with carbonaceous compounds from fossil fuel combustion during transport to form fine mode hygroscopic pollution aerosols (Maxwell-

Meier et al. 2004). Therefore, it is likely that the presence of these aerosols can enhance  $N_{CCN}$ .

Cases IV and V showed similar spectral  $\sigma_{sp}$  dependences with daily mean  $AE_{neph}$  values of 0.64 and 0.86, respectively which suggested a possible mixture of mineral dust and pollution (Figures 40c, f, and i). The mean FMF for both cases were similar in magnitude with daily mean values of 0.4 and 0.45, respectively. For Case IV, the  $\sigma_{sp}$  and FMF parameters were well correlated until 0900 UTC when the aerosol loading decreased while the FMF continued to increase until 0000 UTC on 8 September 2010. This pattern repeats for Case V which may suggest a diurnal dependence and will make an interesting case for future study (Smirnov et al. 2002). The overall  $\sigma_{ap}$  values increased until 9 September 2010 while the spectral dependence remained moderate throughout the aerosol event suggesting an ongoing presence of mineral dust and pollution aerosols.

The relationship between  $\sigma_{sp}$ , FMF, and  $N_{CCN}$  was more complex for Cases IV and V. Though the spectral  $\sigma_{sp}$  dependence was moderate throughout the aerosol event, the dependence weakened during the times of diminished FMF ( $\leq 0.4$ ) on both 7 and 8 September 2010. The mean  $AE_{neph}$  values during the morning (0000-1200 UTC) were 0.36 and 0.69 while the mean FMF values were 0.33 and 0.4 for Cases IV and V, respectively. The corresponding  $N_{CCN}$  trends for Cases IV and V differed in that there was little variation in  $N_{CCN}$  for Case IV while there was a clear decrease in  $N_{CCN}$  for Case V. In contrast, mean  $AE_{neph}$  values increased to 0.95 and 1.03 for Cases IV and V, respectively, while maximum FMF values increased to 0.56 and 0.58, respectively, during the latter part of the day. This was followed by an increase in  $N_{CCN}$ . Case IV had

a correlation of 0.51 between  $\sigma_{sp}$  and  $N_{CCN}$  while Case V had a negative correlation of -0.28 (Figures 41e-f).

This suggests that the aerosol mixtures in Cases IV and V had differing effects on  $N_{CCN}$  possibly due to different chemical and physical properties. For example, it was shown that an extra-tropical system transported the dust and pollution over a distance of several thousand kilometers and a time period of 7-10 days. This is likely why the mineral dust identified in these cases was found to be less coarse than in Case I. It is also possible that more pollution was able to mix with and condense onto the mineral dust for Case IV thereby enhancing the  $N_{CCN}$  number concentration (Karydis et al. 2011). In contrast, Case V likely had mineral dust particles that were less hygroscopic due to less of an interaction with the pollution particles. A more detailed explanation of how mineral dust and pollution react with one another is given in Appendix B. However, more chemical analysis of these aerosol events is needed in future investigations. A summary of the correlations between  $\sigma_{sp}$  and  $N_{CCN}$  of all selected cases is given in Figure 41.

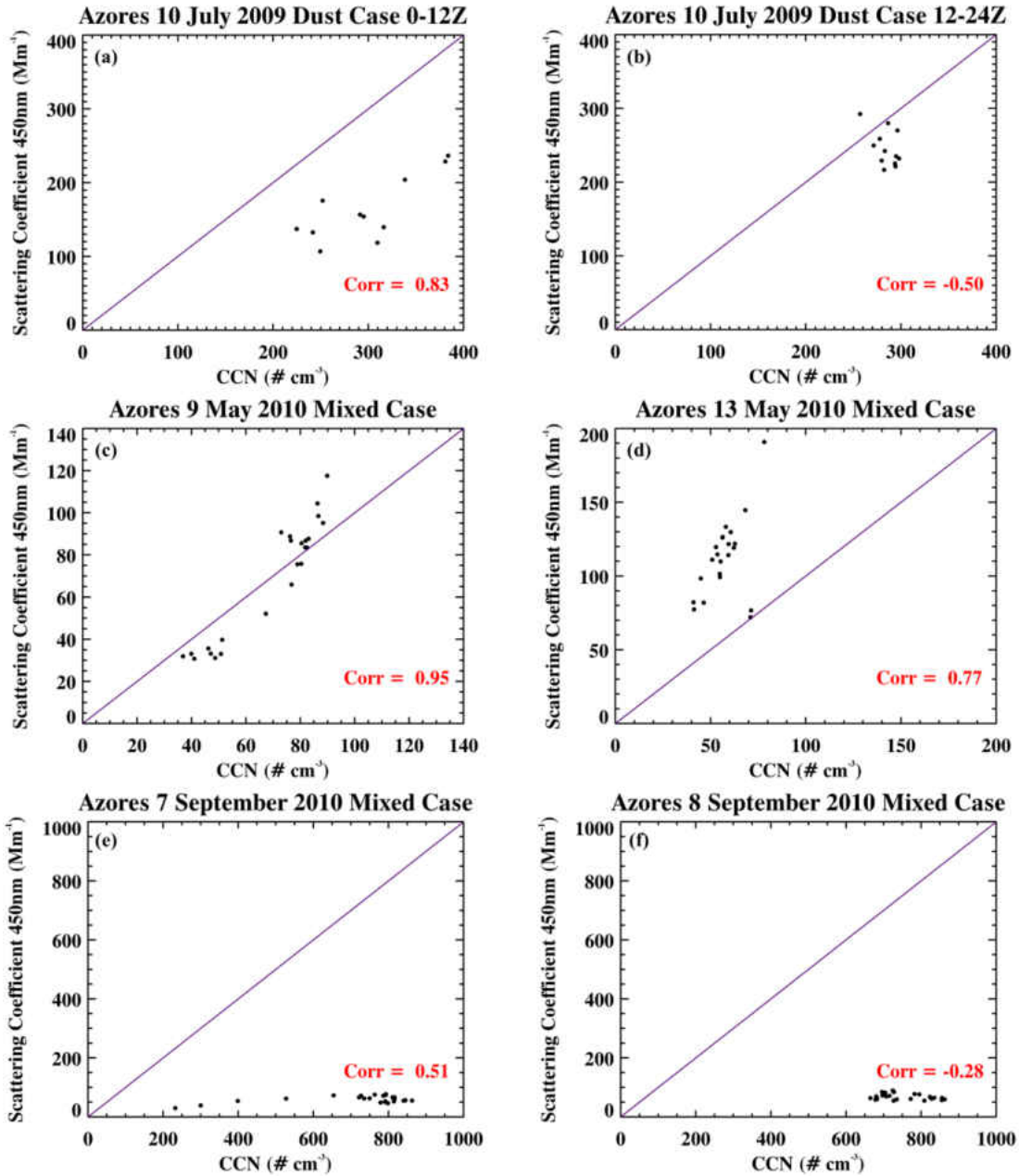


Figure 41. Correlation plots ( $r$ -values) between CCN number concentration ( $N_{CCN}$ ) and  $\sigma_{sp450}$ . The 10 July 2009 dust case is separated into the (a) pre-dust and (b) post-dust event time period. Sea salt is the likely reason for the high correlation prior to the influx of mineral dust particles. The lowest correlation occurred during the dust case while higher correlations occurred for the (c) volcanic ash, (d) pollution, and (e)-(f) mixture cases. Purple line represents 1:1 correlation.

Note that the  $AE_{AOD}$  and  $AE_{neph}$  retrievals had good agreement except for Cases IV and V (Table 8). A possible explanation is due to the fact that the time of the

AERONET retrievals and AOS measurements do not exactly coincide with one another. In addition, aerosols can have different properties at different altitudes and thus requires further investigation. Hence, this can lead to both platforms sampling the same aerosol event at different times while noting that the aerosol properties and composition may change at any given time. For example, Case I had an AERONET retrieval time of 1800 UTC which coincided with the time when the dust plume was detected over the Azores as given by FMF values at or below 0.2.

Similarly, Cases II and III had AERONET retrieval times that coincided with the AOS measurements of the aerosol events. However, Case IV had an AERONET retrieval during the evening (1900 UTC) when the FMF was greater than 0.4 while Case V had a morning retrieval (0900 UTC) when the FMF was less than 0.4. Though both platforms have limitations in representing aerosol events, it is still possible that they can be used to validate one another as long as a transport mechanism that can bring aerosols aloft to near the surface is in place. A summary of both the AERONET and AOS retrievals of AOD, AE, and FMF are provided in Table 8.

Table 8. Summary of mean AOD<sub>440</sub>, Angström exponent (AE), and fine mode fraction (FMF) values for the five selected cases at the AMF-Azores site.

Case	AERONET		AOS Nephelometer	
	AOD <sub>440</sub>	AE <sub>AOD</sub> (440-870 nm)	AE <sub>neph</sub> (450-700 nm)	FMF (550 nm)
I	0.52	0.25	-0.11	0.24
II	0.38	0.71	0.26	0.30
III	0.39	1.08	0.75	0.42 <sup>a</sup>
IV	0.25	1.13	0.64	0.40
V	0.25	0.89	0.86	0.45

<sup>a</sup> Note the maximum FMF for this day was 0.65.

## CHAPTER VI

### CONCLUSIONS

#### The First Scientific Question

A classification method based upon the  $AE_{AOD}$  and  $\omega_{obs}$  parameters has been developed to classify aerosol physico-chemical properties into four separate regions according to their size, absorptive properties, and season. The method is first applied to four AERONET sites, NASA Goddard, Mexico City, Solar Village, and Alta Floresta. These sites represent respective fine mode weakly absorbing (Region I), fine mode strongly absorbing (Region II), coarse mode strongly absorbing (Region III), and coarse mode weakly absorbing (Region IV). Note that Region II often contains fine mode aerosols with variable absorption. The classification method is able to illustrate the relative contributions and seasonal dependence of aerosol types at the four selected sites used in this study.

Four Asian AERONET sites have been selected to represent aerosol properties reflecting biomass burning (Mukdahan), desert-urban (SACOL), pollution (Taihu), and complex mixed particle type (Xianghe) influences. Both Xianghe and Taihu have three identifiable seasonal variations of aerosol types reflecting the influences of local urban/industrial emissions, biomass burning aerosols, mineral dust (Regions I-III). The fine mode Region I aerosols are weakly absorbing ( $\omega_{obs} < 0.07$ ) and are observed mainly during the summer. The fine mode Region II aerosols are strongly absorbing ( $\omega_{obs} > 0.07$ ) and are observed during the late autumn and winter months. During the spring, the

mineral dust influence is evident by more instances of coarse mode, strongly absorbing aerosols in Region III.

SACOL has aerosol cases that occupy all four regions with the majority of the spring cases in Region III (mineral dust) and the winter/autumn cases in Region II (urban/industrial pollution). The weakly absorbing aerosols ( $\omega_{\text{obs}} < 0.07$ ) in Regions I and IV are likely due to outside aerosol influences that mix with local mineral dust (lower overall  $\alpha_{440-870}$ ). The aerosols are less absorbing overall than at Xianghe and Taihu due to fewer sources of urban and industrial pollution. The aerosol cases at Mukdahan occupy Regions I and II similar to Xianghe and Taihu but have the highest overall  $\alpha_{440-870}$  values (fine mode) and are shown to have a seasonal dependence in aerosol absorptive properties with strongly absorbing biomass burning aerosols in the winter and weakly absorbing biomass aerosols in the autumn.

### **The Second Scientific Question**

Asian aerosol plumes were shown to be in various states of existence suggesting interactions between various aerosol types during transport. The  $\sigma_{\text{sp}}$ ,  $\text{AE}_{\text{neph}}$  and  $\delta\alpha$  parameters were able to infer which aerosol mode (coarse or fine) was dominant within the plumes while HYSPLIT trajectory analysis illustrated the probable aerosol source regions. The spectral aerosol scattering coefficients ( $\sigma_{\text{sp}}$ ) for mineral dust aerosols had the weakest dependence and low  $\text{AE}_{\text{neph}}$  ( $< 0.75$ ) while pollution aerosols had the strongest spectral dependences and highest  $\text{AE}_{\text{neph}}$  values ( $> 1$ ). Mixtures of mineral dust and pollution had intermediate spectral dependences and  $\text{AE}_{\text{neph}}$  values. According to HYSPLIT backward trajectory analysis, we conclude that mineral dust dominated plumes likely had origins over the Gobi desert and did not pass through highly polluted areas

while pollution dominated plumes had trajectories over large urban centers in Asia. Aerosol plumes containing mixtures had source regions stemming from both desert and urban areas.

Biomass smoke aerosols were also shown to have variable physical and chemical properties during transport. The newly operational Grand Forks AERONET site observed numerous biomass burning smoke plumes from wildfires in the intermountain western states (Colorado, Utah, Idaho, Wyoming, and Montana) as well as the Pacific states (Washington, Oregon, and California). The smoke plumes were transported by persistent meteorological patterns that varied in strength and location throughout the 2012 warm season (26 June – 15 September). Plume transport times ranged from 24 hours to 3 days. The biomass smoke carbonaceous content was highly dependent on mode of generation. Biomass smoke particles generated from the high temperature flaming combustion mode had stronger spectral  $\omega_{\text{obs}}$  dependences than smoke particles generated from the low temperature smoldering combustion mode. In addition, particles generated from the flaming combustion mode had the strongest ARF and ARF<sub>eff</sub> values, respectively, suggesting a strong cooling effect at the surface and a warming effect aloft during transport.

### **The Third Scientific Question**

In addition to the seasonal variations of aerosol properties, five aerosol events were selected at the AMF-Azores site during the 19-month CAP-MBL campaign to demonstrate the properties of various aerosol types and their impacts on MBL  $N_{CCN}$  which are the precursors to cloud development and sustainability (e.g., AIE). The

selected aerosol events over the Azores were found to contain mixtures of mineral dust, pollution, and biomass burning particles.

The winter months had the highest surface mean wind speed ( $6.7 \text{ m s}^{-1}$ ) which attributed to the greatest contribution of sea salt to AOD. The low  $AE_{AOD}$  values further demonstrated that coarse mode aerosols were dominant. During the spring, strong wind speeds ( $5.5 \text{ m s}^{-1}$ ) and moderate  $AE_{AOD}$  values (0.55-0.95) suggested contributions of coarse and fine mode aerosols (mean  $AOD_{440}=0.18$ ). Higher  $AE_{AOD}$  combined with decreased surface wind speeds suggested continental fine mode aerosols were the main contributors to AOD during the warm season months (May-September).

The aerosols in Case I were identified as mineral dust aerosols with origins in the Saharan desert. These aerosols were generally in the coarse mode, exhibited weak spectral AOD and  $\sigma_{sp}$  dependences, and had FMF values of 0.2 or less. However, the  $\sigma_{ap}$  spectral dependence was particularly strong in the visible which indicated the presence of mineral dust as opposed to sea salt aerosols which have much weaker absorption at all wavelengths. The  $N_{CCN}$  values declined with increasing  $\sigma_{sp}$  and decreasing FMF which suggests a negative correlation between mineral dust loading and their inability to activate as CCN. This was likely a result of the large particle size of the dust particles as the mean  $AE_{neph}$  decreased to negative values (-0.11).

Cases II and III exhibited differing FMF, AOD, and  $\sigma_{sp}$  spectral dependences which suggested two different aerosol types. The spectral dependence for Case II was weaker than Case III while the FMF for Case II was less than for Case III which indicated more of a coarse mode influence. Backward trajectory analysis for Case II identified a possible source region near Iceland during the time of increased volcanic

activity in that area and thus these aerosols were likely coarse mode, volcanic ash particles. Case III likely consisted of mixtures of urban/industrial pollution and biomass burning from Central and North America. The trend in  $N_{CCN}$  paralleled the  $\sigma_{sp}$  and FMF trends in both cases suggesting these aerosols had a strong capability to serve as nuclei likely due to their respective sulfate content (Garrett and Hobbs 1995; Andreae 2009; Langmann 2013; Seifert et al. 2011).

Cases IV and V represented an interesting case of aerosol mixtures. Both cases had similar aerosol properties in terms of spectral dependence and FMF which were in between those of Case I and Case III. However, Case V had a slightly larger coarse mode volume contribution and  $\sigma_{ap}$  spectral dependence than Case IV suggesting a stronger mineral dust influence. Backward trajectory analysis showed influences of urban/industrial pollution and biomass smoke from North America along with Saharan mineral dust likely transported to the Azores by an extratropical cyclone (i.e., remnants of Hurricane Earl). The relationship between the aerosol types and  $N_{CCN}$  were complex in that when the FMF decreased below 0.4, the  $N_{CCN}$  values also decreased. This was more evident in Case V than Case IV and was similar to Case I where mineral dust aerosols had negative influences on  $N_{CCN}$ .

### **Future Areas of Research**

Many assumptions were made in addressing the physico-chemical nature, method of transport from source to sink regions, and impacts on cloud condensation nuclei number concentration of aerosols. In order to validate the assumptions of the chemical nature of the aerosols inferred in this study, chemical measurements will be incorporated into future studies concerning the physico-chemical nature of aerosols (e.g., EAST-AIRE

field campaign). Appendix B contains a more detailed explanation by using chemical ion data to explain the alteration of mineral dust by pollution. For example, mineral dust that is more associated with pollution will have more correlation with anthropogenic cationic compounds such as potassium and ammonium (Maxwell-Meier et al. 2004).

During aerosol transport, more effort needs to be made when discerning between local aerosol influences and influences due to long range transport. Satellite observations generally have good global coverage with spatial resolutions up to 0.25 km x 0.25 km but have long temporal scales in terms of observations over any given area. For example, the MODIS-Aqua satellite has two overpasses per day over any given area. In addition, clouds can be an issue when trying to retrieve aerosol data. In contrast, in situ measurements have shorter temporal resolutions (e.g., seconds or minutes). However, ground-based in situ measurements represent point sources and will not have good spatial coverage while sub-orbital in situ measurements are performed during IOP campaigns which occur for a short period of time. Therefore, any method to quantify aerosol behavior would certainly need a combination of these measurement techniques to ensure locally generated aerosols are not confused with aerosols advected from upwind source regions (Jeong et al. 2005).

Lastly, aerosol impacts on  $N_{CCN}$  can be further investigated by utilizing more cloud physical properties such as  $r_e$ , liquid water path (LWP), and  $N_C$ . The main questions here are: (1) How are aerosols aloft becoming surface CCN? and (2) How are cloud physical properties being impacted by these aerosol-induced changes in  $N_{CCN}$ ? The first question was briefly touched upon by SQ3 in this dissertation. According to the Feingold et al. (2001), (2003), and (2006) studies, the aerosol indirect effect (AIE) can be

predicted by the relationship between the aerosol optical depth (AOD) and cloud droplet effective radius ( $r_e$ ) and is given by the expression,

$$AIE = -\frac{d \ln r_e}{d \ln AOD}, \quad (11)$$

Though this relationship is shown as a total derivative, the partial derivatives are used in order to further explore and predict aerosol-cloud interactions. Figure 42 shows the relationship between  $r_e$  and  $\sigma_{sp}$  (proxy for AOD) for the three cases addressed in SQ3.

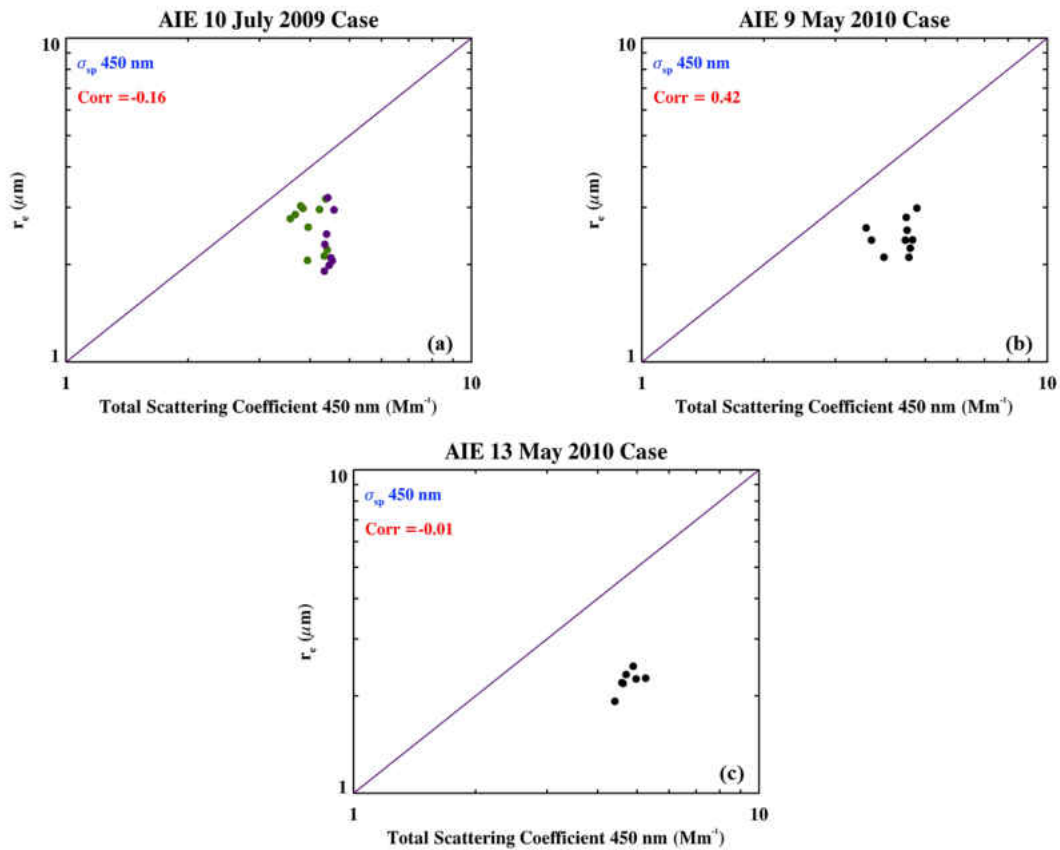


Figure 42. The log-log AIE relationships of the cloud base retrieved  $r_e$  and surface measured  $\sigma_{sp}$  for the (a) 10 July 2009 dust case, (b) 9 May 2010 volcanic ash case, and (c) 13 May 2010 pollution case during the CAP-MBL campaign conducted over the Azores. The dust case in (a) is separated into green data points (sea salt) and purple data points (mineral dust).

Figure 42a shows that there is an overall negative relationship between  $r_e$  and  $\sigma_{sp}$  but it seems to be more pronounced during the mineral dust time period. In other words, the mean effective radius is lower for during the time when mineral dust is present (purple data points) than for the time when sea salt is present (green data points). This supports the conclusion from SQ3 that mineral dust likely has a negative impact on CCN activation, but more cases will certainly be needed to draw any further conclusions. During the volcanic ash and pollution cases (Figures 42b and c), higher  $r_e$  corresponds with higher aerosol loading ( $r=0.42$ ). However, in the pollution case, though the overall correlation is near zero, the highest  $r_e$  values are weakly related with the highest aerosol loading. It should be noted that Feingold et al. (2006) used Raman LIDAR aerosol products and pointed out that using  $\sigma_{sp}$  may not be appropriate due to large variability and uncertainties in measurements. Thus, more investigation is needed in future studies.

A permanent ARM facility is currently being installed in the Azores (ENA-Azores) at the former site used in this study. This will give a more detailed seasonal climatology of both cloud and aerosol properties that will aid in the future study of the AIE over this region. An additional future study will compare aerosol influences on cloud properties over the Southern Great Plains (ARM-SGP facility) with the ENA-Azores facility in order to further investigate the differences of AIE over continental and marine regions.

## **APPENDICES**

## APPENDIX A

### Calculation of Number Size Distribution

The volume size distribution ( $dV/d\ln R$ ) is a derived quantity from inversion algorithms that use solar radiance retrievals (Dubovik et al. 2000) rather than direct in situ, filter-based measurements. This causes some confusion when comparing the units between these two types of observation platforms. The traditional in situ measurements of size distributions are in units of some quantity per sampling volume (e.g.,  $\# \text{ m}^{-3}$ ). However, AERONET size distribution retrievals are column integrated and typically have units that denote a quantity per cross-sectional sampling area (e.g.,  $\mu\text{m}^3 \mu\text{m}^{-2}$ ). In addition, converting between volume ( $dV/d\ln R$ ) and number ( $dN/d\ln R$ ) distributions raises serious concerns due to large uncertainties in AERONET retrievals involving low aerosol loading conditions ( $\text{AOD} < 0.2$ ). This is likely the reason that few studies utilize the AERONET retrieved number size distribution ( $dN/d\ln R$ ).

The Dubovik et al. (2000) developed a method of calculating the  $dV/d\ln R$  parameter by using the general equation,

$$\frac{dR^n(r)}{d \ln r} = \sum_{i=1}^2 \frac{C_{n,i}}{\sqrt{2\pi}\sigma} \exp\left[-\frac{1}{2}\left(\frac{\ln r - \ln r_{n,i}}{\sigma}\right)^2\right], \quad (\text{A1})$$

where  $n$  denotes a moment of size distribution (e.g., 0 for  $dN/d\ln R$  and 3 for  $dV/d\ln R$ ),  $i$  denotes the fine ( $i=1$ ) and coarse ( $i=2$ ) modes,  $C$  denotes particle concentration per cross sectional area (e.g., square length unit) of atmospheric column ( $\# \mu\text{m}^{-2}$  for  $C_N$  and  $\mu\text{m}^3 \mu\text{m}^{-2}$  for  $C_V$ ),  $r$  denotes the particle radius in microns,  $r_{n,i}$  denotes the modal radius (fine ( $i=1$ ) or coarse ( $i=2$ ) modes) in microns, and  $\sigma$  is the dimensionless standard

deviation (Remer et al. 1998). The values for the third moment ( $n=3$ ) of Eq. (A1) are given in the AERONET data set in 22 logarithmically spaced bins of particle radii that range from 0.05  $\mu\text{m}$  to 15  $\mu\text{m}$ . This covers the particle size spectrum from the accumulation to the coarse mode. The  $dN/d\ln R$  parameter can also be derived from the volume size distribution ( $dV/d\ln R$ ) by the following equation (Dubovik et al. 2006),

$$\frac{dV}{d \ln R} = \frac{4}{3} \pi r_e^3 \frac{dN}{d \ln R}, \quad (\text{A2})$$

where  $r_e$  is the AERONET retrieved effective radius of aerosol particle (in microns) in this study rather than the radius of each individual bin ( $dR$ ). The  $dV/d\ln R$  parameter has units of  $\mu\text{m}^3 \mu\text{m}^{-2}$  while  $dN/d\ln R$  has units of  $\# \mu\text{m}^{-2}$ .

We use  $r_e$  in Eq. (A2) in order to quantify the column integrated contribution of fine and coarse mode particles to aerosol number rather than the actual number of aerosol particles. It is well known that fine mode aerosols consisting of smaller sea salt particles, biogenic aerosols, and transported accumulation mode aerosols can all serve to dominate aerosol loading due to their larger number concentration. Therefore, if we use the size bin radius  $R$  rather than  $r_e$ , the relative contributions of both fine and coarse modes is undoubtedly biased towards the fine mode leaving little explanation for any discernible influences of the coarse mode particles as demonstrated in Figure A1. Figures 2b and 3b demonstrate that the use of  $r_e$  can clearly represent both the coarse and fine mode information for the different seasons.

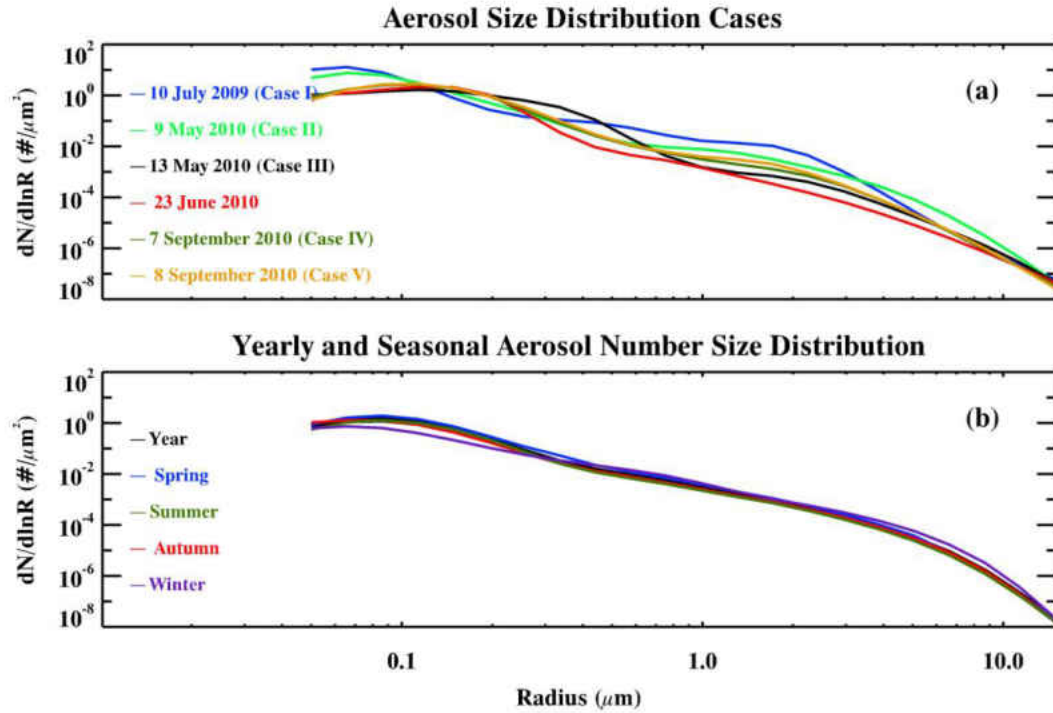


Figure A1. Number size distributions for the (a) individual cases using the AERONET bin radius  $R$  instead of the effective radius of the aerosol particle ( $r_e$ ) as well as the (b) yearly and seasonal means. Figures 2b and 3b using  $r_e$  can clearly represent both the coarse and fine mode information for the different seasons.

## APPENDIX B

### Closure Study

The 2006 INTEX-B field campaign contained a wealth of physical and chemical data on Asian aerosols. This section will provide a brief closure study that links the goals of the M. S. thesis and dissertation using the chemical data of INTEX-B and aerosol classification method of the Logan et al. (2013a) study. Figure B1 shows the chemical ion data for all the INTEX-B flight tracks. From the plots given by Figures B1a and B1b, the top panel shows the balance of cations and anions measured by ion chromatography. This represents the total concentrations of continental and anthropogenic derived compounds along the flight track over the remote Pacific Ocean.

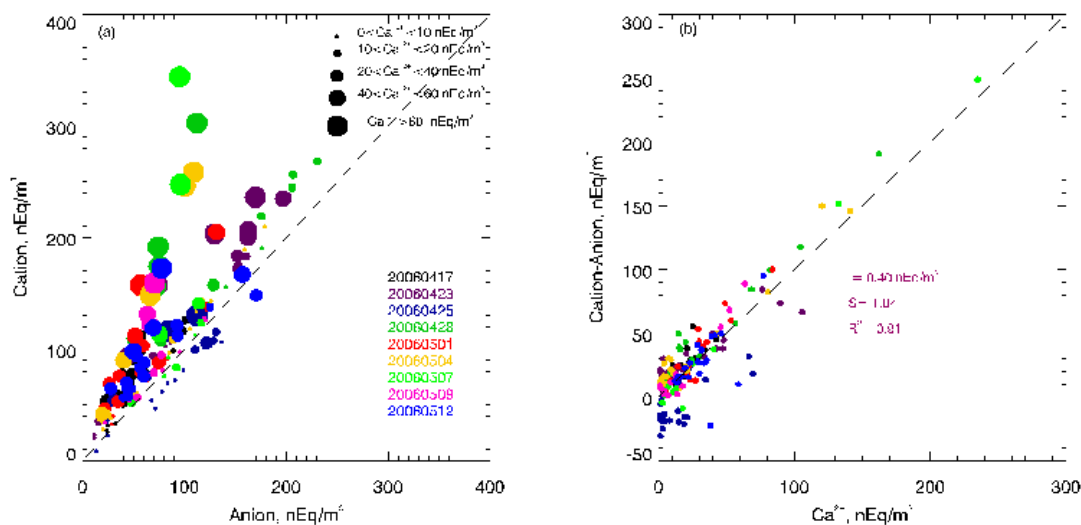


Figure B1. Scatterplots of (a) total cation vs. total anion and (b) calcium vs. carbonate (cation-anion difference).

The cations are given by (a) sea salt (oceanic) sources – sodium ( $\text{Na}^+$ ) and magnesium ( $\text{Mg}^{2+}$ ), (b) mineral dust (continental) sources – calcium ( $\text{Ca}^{2+}$ ), (c) pollution and biomass (anthropogenic) sources – potassium ( $\text{K}^+$ ) and ammonium ( $\text{NH}_4^+$ ). The

anions are given by (a) oceanic sources – chloride ( $\text{Cl}^-$ ), (b) anthropogenic sources – nitrate ( $\text{NO}_3^-$ ) and sulfate ( $\text{SO}_4^{2-}$ ). Their concentrations are compared to the ones taken from an ACE-Asia investigation (Maxwell-Meier et al. 2004) where the dust events were closer to the Asian continent. The concentration of  $\text{Ca}^{2+}$  in the dust plume was found to be much lower over the remote Pacific Ocean than in the plume before it exited the Asian continent. A 1:1 relationship shows a complete balance among the various cation and anion tracers but the top panel shows trending more towards the cations. This is a similar trend to the results from the ACE-Asia experiment with much higher  $\text{Ca}^{2+}$  concentrations closer to the Asian continent.

An anion that was not directly measured was the carbonate ( $\text{CO}_3^{2-}$ ) in the dust plume. Acid aqueous phase aerosols (pollution) can react with the mineral dust. Calcium carbonate ( $\text{CaCO}_3$ ) is the most abundant compound present in mineral dust that will readily react with the pollution. The difference of the cation and anion concentrations can yield the amount of carbonate to a first order approximation as other anions. For example, silicate and organic anions should have concentrations much less than that of carbonate. The bottom panel shows the correlation ( $r^2$ -value) between  $\text{Ca}^{2+}$  and the  $\text{CO}_3^{2-}$  of the entire field campaign.  $\text{Mg}^{2+}$  ions are not included in the abscissa in this study because we did not find a strong general correlation between  $\text{Mg}^{2+}$  and  $\text{Ca}^{2+}$  over the remote Pacific Ocean. Therefore it is suggested that the majority of  $\text{Mg}^{2+}$  did not have continental origins. In fact, magnesium was shown to have a stronger correlation with sodium than calcium throughout the campaign. From Figure B1b, 25 April 2006 was the only day that showed no correlation between  $\text{CO}_3^{2-}$  and  $\text{Ca}^{2+}$  possibly due to a lack of calcium carbonate generation during transport. The surplus of anions for that particular

day may be explained by that particular dust event having more than one source region (e.g., Taklamakan Desert).

Figure B2a may also further prove the coexistence of dust and pollution. It shows the correlation between anthropogenic cations ( $K^+$  and  $NH_4^+$ ) and anions ( $NO_3^-$  and  $SO_4^{2-}$ ) with the trend showing a shift towards the anions. This suggests that the anions are more associated with mineral cations (e.g.,  $Ca^{2+}$ ) other than the  $K^+$  and  $NH_4^+$ . The slopes for each flight are much greater than 1 for 5 out of 9 legs and close to 1 for other four flights. The cases that show a slope much greater than 1 may be a result of the more favored mineral dust and pollution reactions. The overall slope for the data in Figure B2a was 1.25 with an intercept of  $2.80 \text{ nEq m}^{-3}$ . This suggested that the nitrate and sulfate were closely associated with mineral and/or oceanic cations during INTEX-B experiments. The correlation coefficient between  $Ca^{2+}$  and  $SO_4^{2-}/NO_3^-$  is 0.67 and there is no correlation between  $Na^+$  (or  $Mg^+$ ) and  $SO_4^{2-}/NO_3^-$ . Therefore, the analysis further proves that mineral dust particles catalyzed the reaction during the transpacific transport. In Figure B2b, a strong correlation exists for the sea salt tracer ions except for the 25 April 2006 flight leg. As mentioned previously, a shift away from the 1:1 linear regression suggests multiple sources, and in this case, an overabundance of chloride hence another source.

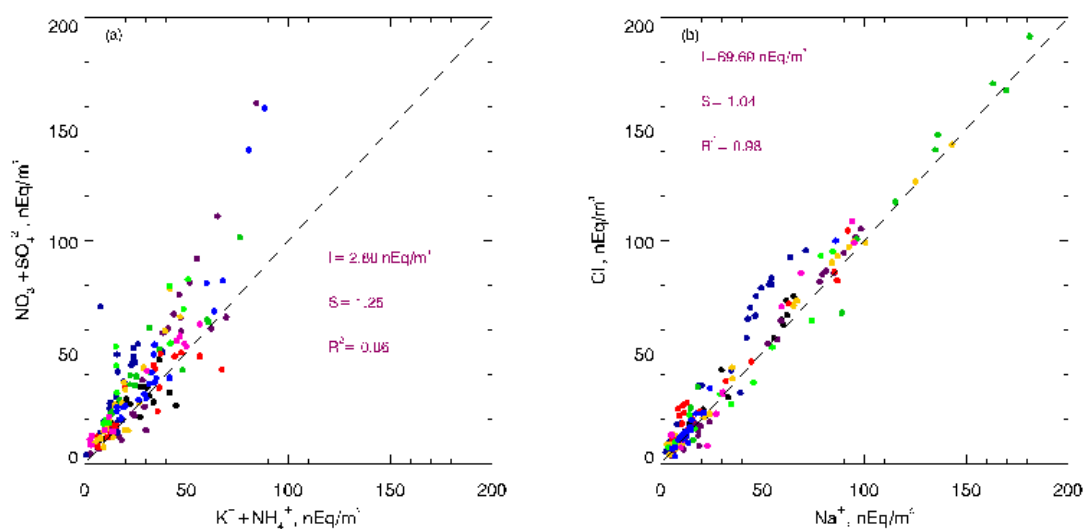


Figure B2. Scatterplots of (a) anthropogenic (pollution) cations vs. anions and (b) sea salt ions ( $\text{Na}^+$  vs.  $\text{Cl}^-$ ).

Figure B3 shows the four selected INTEX-B aerosol cases used in this dissertation as classified by  $\text{Ca}^{2+}$  concentration (colored circles),  $\text{AE}_{\text{neph}}$ , and  $\omega_{\text{oabs}}$ . The  $\text{Ca}^{2+}$  observations are denoted as follows: in-plume (red circles), sea level (ovals), and free troposphere (colored circles). Note that the sea level observations typically have  $\text{AE}_{\text{neph}}$  less than unity suggesting  $\text{Ca}^{2+}$  that are more associated with sea salt (e.g.,  $\text{Na}^+$  and  $\text{Cl}^-$ ). Hence, this was the primary reason flight legs near the marine boundary layer were not studied. The free troposphere  $\text{Ca}^{2+}$  observations were also not included due to stratospheric air intrusions and possible cloud contamination which can likely lead to biases in the data.

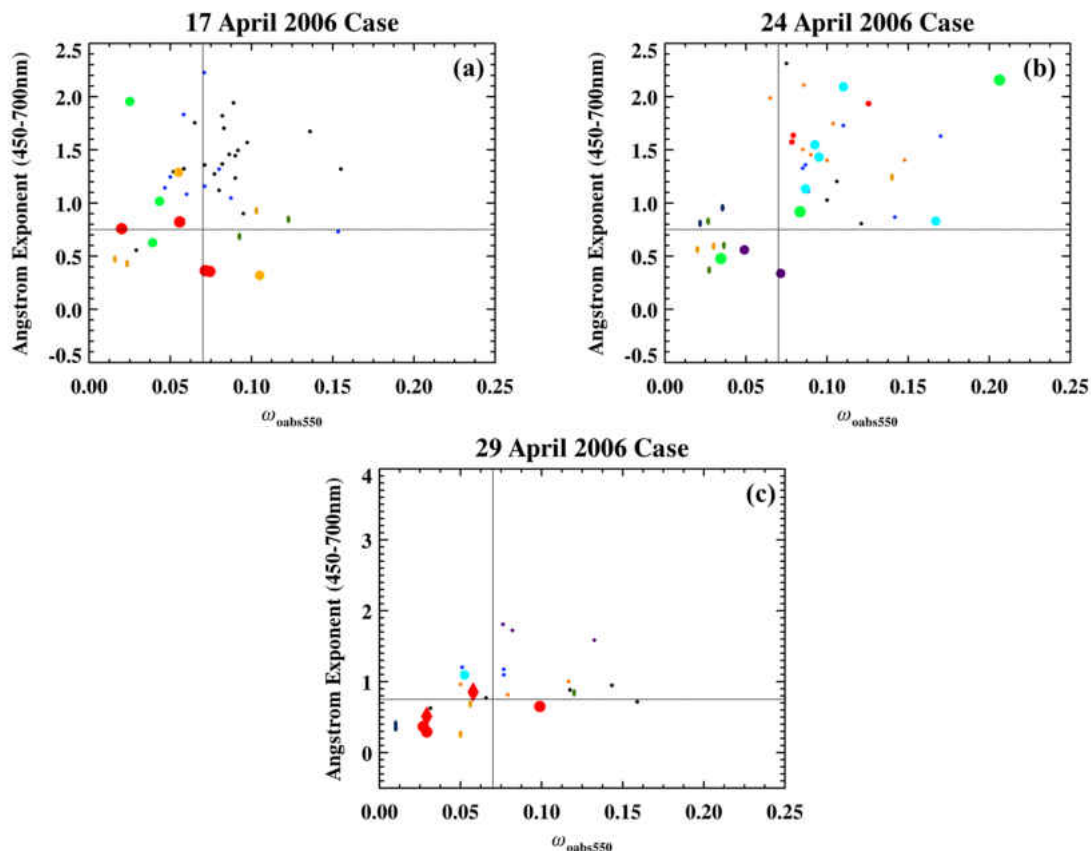


Figure B3. Aerosol classification method using  $\text{Ca}^{2+}$  concentration observations for (a) Case I, (b) Case II, and (c) Cases III and IV. Circle color denotes in-plume (red), sea level (oval), and free troposphere (multi-colored) while circle size denotes relative  $\text{Ca}^{2+}$  concentrations.

The 17 April 2006 case was previously identified as a dust case though some pollution was present. Note that the in-plume  $\text{Ca}^{2+}$  observations have  $\text{AE}_{\text{neph}}$  values near or below 0.75 and are weakly absorbing ( $\omega_{\text{obs}} < 0.07$ ) likely suggesting that the mineral dust aerosols in this case did not extensively react with pollution aerosols during transport. In addition, the  $\text{Ca}^{2+}$  concentrations for this case were moderately correlated ( $r^2=0.42$ ) with  $\text{SO}_4^{2-}$  ions (pollution) which further supports this claim. The 24 April 2006 case is in stark contrast in that the in-plume  $\text{Ca}^{2+}$  observations have  $\text{AE}_{\text{neph}}$  values greater than 1.5 and have stronger absorption ( $\omega_{\text{obs}} > 0.08$ ). This likely indicates that the mineral dust aerosols have reacted with pollution during transport and are more

associated with the fine mode. This is further supported by this case having the strongest correlation of  $\text{Ca}^{2+}$  with  $\text{SO}_4^{2-}$  concentrations ( $r^2=0.84$ ). The 29 April 2006 cases consist of Case III (red circle) and Case IV (red diamond). These cases had the highest  $\text{Ca}^{2+}$ ,  $\text{SO}_4^{2-}$ , and  $\text{NO}_3^-$  concentrations. Both cases have in-plume  $\text{Ca}^{2+}$  observations with  $\text{AE}_{\text{neph}}$  near or less than 0.75 and  $\omega_{\text{obs}}$  less than 0.07 with the exception of one observation where  $\omega_{\text{obs}}$  approaches 0.1. This is likely due to mineral dust coated with strongly absorbing carbonaceous compounds in addition to  $\text{SO}_4^{2-}$  pollution as similar to the 24 April 2006 case. The correlations between  $\text{Ca}^{2+}$  and  $\text{SO}_4^{2-}$  are between Cases I and II ( $r^2=0.53$ ).

## REFERENCES

- Ackerman, P. and O. B. Toon (1981), Absorption of visible radiation in atmosphere containing mixtures of absorbing and nonabsorbing particles, *Appl. Opt.*, *20*, 3661–3668.
- Ackerman, S., K. Strabala, P. Menzel, R. Frey, C. Moeller, and L. Gumley (1998), Discriminating clear sky from clouds with MODIS, *J. Geophys. Res.*, *103*, 32,139-32,140.
- Anderson, T. L., and J. A. Ogren (1998), Determining aerosol radiative properties using the TSI 3563 Integrating Nephelometer, *Aerosol Sci. Technol.*, *29*, 57-69.
- Anderson, T. L., D. S. Covert, J. D. Wheeler, J. M. Harris, K. D. Perry, B. E. Trost, D. J. Jaffe and J. A. Ogren (1999), Aerosol backscatter fraction and single scattering albedo: Measured values and uncertainties at a coastal station in the Pacific Northwest, *J. Geophys. Res.*, *104*, D21, 26,793-26,807.
- Anderson, T. L., S. J. Masonis, D. S. Covert, N. C. Ahlquist, S. G. Howell, A. D. Clarke, and C. S. McNaughton (2003), Variability of aerosol optical properties derived from in situ aircraft measurements during ACE-Asia, *J. Geophys. Res.*, *108*, D23, 8647, doi:10.1029/2002JD003247.
- Andreae, M. O. (2009), Correlation between cloud condensation nuclei concentration and aerosol optical thickness in remote and polluted regions, *Atmos. Chem. Phys.*, *9*, 543–556, [www.atmos-chem-phys.net/9/543/2009/](http://www.atmos-chem-phys.net/9/543/2009/).

- Andreae, M. O. and A. Gelencsér (2006), Black carbon or brown carbon? The nature of light-absorbing carbonaceous aerosols, *Atmos. Chem. Phys.*, *6*, 3131–3148.
- Bachmeier, A. S., R. E. Newel, M. C. Shipham, Y. Zhu, D. R. Blake, and E. V. Browell (1996), PEM-West A: Meteorological overview, *J. Geophys. Res.*, *101*, D1, 1655-1677.
- Bergstrom, R. W., P. B. Russell, and P. Hingett (2002), Wavelength Dependence of the Absorption of Black Carbon Particles: Predictions and Results from the TARFOX Experiment and Implications for the Aerosol Single Scattering Albedo, *J. Atmos. Sci.*, 567–577.
- Bergstrom, R. W., P. Pilewskie, J. Pommier, M. Rabbette, P. B. Russell, B. Schmid, J. Redemann, A. Higurashi, T. Nakajima, and P. K. Quinn (2004), Spectral absorption of solar radiation by aerosols during ACE-Asia, *J. Geophys. Res.*, *109*, D19S15, doi:10.1029/2003JD004467.
- Bergstrom, R. W., P. Pilewskie, P. B. Russell, J. Redemann, T. C. Bond, P. K. Quinn, and B. Sierau (2007), Spectral absorption properties of atmospheric aerosols, *Atmos. Chem. and Phys.*, *7*, 5937–5943.
- Bi, J., J. Huang, Q. Fu, X. Wang, J. Shi, W. Zhang, Z. Huang, B. Zhang (2010), Toward characterization of the aerosol optical properties over Loess Plateau of Northwestern China, *JQSRT*, *112*, 346–360, doi:10.1016/j.jqsrt.2010.09.006.
- Bingemer H., et al. (2012), Atmospheric ice nuclei in the Eyjafjallajökull volcanic ash plume, *Atmos. Chem. Phys.*, *12*, 857–867, [www.atmos-chem-phys.net/12/857/2012/](http://www.atmos-chem-phys.net/12/857/2012/) doi:10.5194/acp-12-857-2012.

- Bond, T. C., T. L. Anderson, and D. Campbell (1999), Calibration and intercomparison of filter-based measurements of visible light absorption by aerosols, *Aerosol Sci. Technol.*, *30*, 6, 582-600, doi:10.1080/027868299304435.
- Bond, T. C., and R. W. Bergstrom (2005), Light absorption by carbonaceous particles: An investigative review, *Aerosol Sci. Technol.*, *39*, 1-41, doi:10.1080/02786820500421521.
- Browell, E. V., S. Ismail, and W. B. Grant (1998), Differential absorption lidar (DIAL) measurements from air and space, *Appl. Phys. B*, *67*, 399-410.
- Chambers, L.H., B. Lin, and D.F. Young (2002), Examination of new CERES data for evidence of tropical Iris feedback, *J. Clim.*, *15*, 3719-3726.
- Chung, C. E., V. Ramanathan, and D. Decremer (2012), Observationally constrained estimates of carbonaceous aerosol radiative forcing, *P. Natl. Acad. Sci. USA*, *109*, 11,624-11,629.
- Clarke, A. D., et al. (2004), Size distributions and mixtures of dust and black carbon aerosol in Asian outflow: Physiochemistry and optical properties, *J. Geophys. Res.*, *109*, D15S09, doi:10.1029/2003JD004378.
- Corr, C. A., et al. (2012), Spectral absorption of biomass burning aerosol determined from retrieved single scattering albedo during ARCTAS, *Atmos. Chem. Phys.*, *12*, 10,505–10,518, [www.atmos-chem-phys.net/12/10505/2012/](http://www.atmos-chem-phys.net/12/10505/2012/)doi:10.5194/acp-12-10505-2012.
- Corrigan, C. E., V. Ramanathan, and J. J. Schauer (2006), Impact of monsoon transitions on the physical and optical properties of aerosols, *J. Geophys. Res.*, *111*, D18208, doi:10.1029/2005JD006370.

- Dong, X., B. Xi, A. Kennedy, P. Minnis, and R. Wood (2014), A 19-month record of marine aerosol-cloud-radiation derived from the DOE ARM AMF deployment at the Azores: Part I: Cloud fraction and single-layered MBL cloud properties, *J. Clim*, doi: 10.1175/JCLI-D-13-00553.1.
- Draxler, R.R. and Rolph, G.D. (2003), HYSPLIT (Hybrid Single-Particle Lagrangian Integrated Trajectory) Model access via NOAA ARL READY Website (<http://www.arl.noaa.gov/ready/hysplit4.html>), NOAA Air Resources Laboratory, Silver Spring, MD.
- Draxler, R.R. and G.D. Rolph (2012), HYSPLIT (HYbrid Single-Particle Lagrangian Integrated Trajectory) Model access via NOAA ARL READY Website (<http://ready.arl.noaa.gov/HYSPLIT.php>). NOAA Air Resources Laboratory, Silver Spring, MD.
- Dubovik, O., A. Smirnov, B. N. Holben, T. F. Eck, M.D. King, Y. J. Kaufman, and I. Slutsker (2000), Accuracy assessments of aerosol optical properties retrieved from Aerosol Robotic Network (AERONET) Sun and sky radiance measurements, *J. Geophys. Res.*, *105*, D8, 9791-9806.
- Dubovik, O., and M. King (2000), A flexible inversion algorithm for retrieval of aerosol optical properties from Sun and sky radiance measurements, *J. Geophys. Res.*, *105*, D16, 20,673-20,696.
- Dubovik, O., B. Holben, T. F. Eck, A. Smirnov, Y. J. Kaufman, M. D. King, D. Tanré, and I. Slutsker (2002), Variability of absorption and optical properties of key aerosol types observed in worldwide locations, *J. Atmos. Sci.*, *59*, 590-608.

- Dubovik, O., et al. (2006), Application of spheroid models to account for aerosol particle nonsphericity in remote sensing of desert dust, *J. Geophys. Res.*, *111*, D11208, doi:10.1029/2005JD006619.
- Eck, T. F., B. N. Holben, J. S. Reid, O. Dubovik, A. Smirnov, N. T. O'Neill, I. Slutsker, and S. Kinne (1999), Wavelength dependence of the optical depth of biomass burning, urban, and desert dust aerosols, *J. Geophys. Res.*, *D24*, 31,333-31,349.
- Eck, T. F., et al. (2005), Columnar aerosol optical properties at AERONET sites in central eastern Asia and aerosol transport to the tropical mid-Pacific, *J. Geophys. Res.*, *110*, D06202. doi:10.1029/2004JD005274, 2005.
- Eck, T. F., et al. (2010), Climatological aspects of the optical properties of fine/coarse mode aerosol mixtures, *J. Geophys. Res.*, *115*, D19205, doi:10.1029/2010JD014002, 2010.
- Feingold, G., L. A. Remer, J. Ramaprasad, and Y. J. Kaufman (2001), Analysis of smoke impacts on clouds in Brazilian biomass burning regions: An extension of Twomey's approach, *J. Geophys. Res.*, *106*, D19, 22,907-22,922.
- Feingold, G., W. L. Eberhard, D. E. Veron, and M. Previdi (2003), First measurements of the Twomey indirect effect using ground-based remote sensors, *Geophys. Res. Lett.*, *30*, 1287-1291.
- Feingold, G., R. Furrer, P. Pilewskie, L. A. Remer, Q. Min, and J. Jonsson (2006), Aerosol indirect effect studies at Southern Great Plains during the May 2003 Intensive Operations Period, *J. Geophys. Res.*, *111*, D05S14, doi:10.1029/2004JD005648.

- Fiahlo, P., et al. (2005), Absorption coefficients by aerosols in remote areas: A new approach to decouple dust and black carbon absorption coefficients using seven wavelength Aethalometer data, *J. Aer. Sci.*, 36(2), 267-282.
- García, O. E., et al. (2012), Shortwave radiative forcing and efficiency of key aerosol types using AERONET data, *Atmos. Chem. Phys.*, 12, 5129–5145, [www.atmos-chem-phys.net/12/5129/2012/doi:10.5194/acp-12-5129-2012](http://www.atmos-chem-phys.net/12/5129/2012/doi:10.5194/acp-12-5129-2012).
- Garrett, T. J., and P. V. Hobbs (1995), Long-range transport of continental aerosols over the Atlantic Ocean and their effects on cloud structures, *J. Atmos. Sci.*, 52(16), 2977-2984.
- Gautam, R., et al. (2012), Characterization of aerosols over the Indochina peninsula from satellite-surface observations during biomass burning pre-monsoon season, *Atmos. Environ.*, <http://dx.doi.org/10.1016/j.atmosenv.2012.05.038>.
- Ge, J. M., et al. (2010), Dust aerosol optical properties retrieval and radiative forcing over northwestern China during the 2008 China-U.S. joint field experiment, *J. Geophys. Res.*, 115, D00K12, doi:10.1029/2009JD013263.
- Giles, D. M., B. N. Holben, S. N. Tripathi, T. F. Eck, W. W. Newcomb, I. Slutsker, R. R. Dickerson, A. M. Thompson, S. Mattoo, S.-H. Wang, R. P. Singh, A. Sinyuk, and J. S. Schafer (2010), Aerosol properties over the Indo-Gangetic Plain: A mesoscale perspective from the TIGERZ experiment, *J. Geophys. Res.*, 116, D18203, doi:10.1029/2011JD015809.
- Gobbi, G. P., Y. J. Kaufman, I. Koren, and T. F. Eck (2007), Classification of aerosol properties derived from AERONET direct sun data, *Atmos. Chem. Phys.*, 7, 453-458.

- Gyawali, M., et al. (2009), In situ aerosol optics in Reno, NV, USA during and after the summer 2008 California wildfires and the influence of absorbing and non-absorbing organic coatings on spectral light absorption, *Atmos. Chem. Phys.*, *9*, 8007–8015, [www.atmos-chem-phys.net/9/8007/2009/](http://www.atmos-chem-phys.net/9/8007/2009/).
- Hansen, J. and Sato M (2001), Trends of measured climate forcing agents, [http://pubs.giss.nasa.gov/docs/2001/2001\\_Hansen\\_Sato.pdf](http://pubs.giss.nasa.gov/docs/2001/2001_Hansen_Sato.pdf).
- Higurashi, A., and T. Nakajima (2002), Detection of aerosol types over the East China Sea near Japan from four-channel satellite data, *Geophys. Res. Lett.*, *29*(17), 1836, doi:10.1029/2002GL015357.
- Holben, B. N., T. F. Eck, I. Slutsker, D. Tanré, J. P. Buis, A. Setzer, E. Vermote, J. A. Reagan, Y. J. Kaufman, T. Nakajima, F. Lavenu, I. Jankowiak, and A. Smirnov (1998), AERONET – A federated instrument network and data archive for aerosol characterization, *Rem. Sens. Environ.*, *66*, 1–16.
- Holben, B. N., T. F. Eck, I. Slutsker, A. Smirnov, A. Sinyuk, A. J. Schafer, D. Giles, and O. Dubovik (2006), AERONET’s version 2.0 quality assurance criteria, *Remote Sensing of Atmosphere and Clouds, Proc. SPIE Int. Soc. Opt. Eng.*, *6408*, 64080Q, doi:10.1117/12.706524.
- Huang, J. P., et al. (2008a), Long-range transport and vertical structure of Asian dust from CALIPSO and surface measurements during PACDEX, *J. Geophys. Res.*, *113*, D23212, doi:10.1029/2008JD010620, 2008a.
- Huang, J. P., et al. (2008b), An overview of the semi-arid climate and environment research observatory over the Loess Plateau, *Adv. Atmos. Sci.*, *25*(6), 906–921, doi: 10.1007/s00376-008-0906-7.

- Hudson, J. G. and S. N. Noble (2013), CCN and vertical velocity influences on droplet concentrations and supersaturations in clean and polluted stratus clouds, *J. Atmos. Sci.*, *71*(1), 312-331, doi: 10.1175/JAS-D-13-086.1.
- Huebert, B. J., T. Bates, P. B. Russell, G. Shi., Y. J. Kim, K. Kawamura, G. Carmichael, and T. Nakajima (2003), An overview of ACE-Asia: Strategies for quantifying the relationships between Asian aerosols and their climatic impacts, *J. Geophys. Res.*, *108*, D23, doi:10.1029/2003JD003550.
- Husar, R. B., et al. (2001), Asian dust events of April 1998, *J. Geophys. Res.*, *106*, 18,317-18,330.
- Ignatov, A., P. Minnis, N. Loeb, B. Wielicki, W. Miller, S. Sun-Mack, D. Tanré, L. Remer, I. Laszlo, and E. Geier (2005), Two MODIS Aerosol Products over Ocean on the Terra and Aqua CERES SSF Datasets, *J. Atmos. Sci.*, *62*, 1008-1031.
- Intergovernmental Panel on Climate Change (2001), *Climate Change 2001: The Scientific Basis*, Contribution of Working Group I to the Third Assessment Report of the Intergovernmental Panel on Climate Change, edited by J. T. Houghton et al., Cambridge Univ. Press, New York, 881 pp.
- Intergovernmental Panel on Climate Change (2007), *Climate Change 2007: The Physical Science Basis*. Contribution of Working Group I to the Fourth Assessment Report of the Intergovernmental Panel on Climate Change, edited by Solomon, S., D. Qin, M. Manning, Z. Chen, M. Marquis, K.B. Avery, M. Tignor and H.L. Miller, Cambridge Univ. Press, New York, 996 pp.

- Jacob, D. J., J. H. Crawford, M. M. Kleb, V. S. Connors, R. J. Bendura, J. L. Raper, G. W. Sachse, J. C. Gille, L. Emmons, and C. L. Heald (2003), Transport and Chemical Evolution over the Pacific (TRACE-P) aircraft mission: Design, execution, and first results, *J. Geophys. Res.*, *108*, 9000, doi:10.1029/2002JD003276.
- Jefferson, A. (2010), Empirical estimates of CCN from aerosol optical properties at four remote sites, *Atmos. Chem. Phys.*, *10*, www.atmos-chem-phys.net/10/6855/2010/ doi:10.5194/acp-10-6855-2010, 6855-6861.
- Jefferson, A. (2011), Aerosol Observing System (AOS) Handbook, ARM-TR-014.
- Jeong, M.-J. and Z. Li (2005), Quality, compatibility, and synergy analyses of global aerosol products derived from the advanced very high resolution radiometer and Total Ozone Mapping Spectrometer, *J. Geophys. Res.*, *110*, D10S08, doi:10.1029/2004JD004647.
- Jin, M. S., W. Kessomkiat, and G. Pereira (2011), Satellite-Observed Urbanization Characters in Shanghai, China: Aerosols, Urban Heat Island Effect, and Land-Atmosphere Interactions, *Rem. Sens.*, *3*, 83-99, doi:10.3390/rs3010083.
- Jordan, C. E., J. E. Dibb, B. E. Anderson, and H. E. Fuelberg (2003), Uptake of nitrate and sulfate on dust aerosols during TRACE-P, *J. Geophys. Res.*, *108*(D21), 8817, doi:10.1029/2002JD003101.
- Kalnay, E., et al. (1996), The NCEP/NCAR re-analysis 40-year project, *Bull. Amer. Meteor. Soc.*, *77*, 437-471.

- Karydis, V. A., P. Kumar, D. Barahona, I. N. Sokolik, and A. Nenes (2011), On the effect of dust particles on global cloud condensation nuclei and cloud droplet number, *J. Geophys. Res.*, *116*, D23204, doi:10.1029/2011JD016283.
- Kato, S., et al. (2010), Relationships among cloud occurrence frequency, overlap, and effective thickness derived from CALIPSO and CloudSat merged cloud vertical profiles, *J. Geophys. Res.*, *115*, D00H28, doi:10.1029/2009JD012277.
- Kim, B.-G., S. E. Schwartz, M. A. Miller, and Q. Min (2003), Effective radius of cloud droplets by ground-based remote sensing: Relationship to aerosol. *J. Geophys. Res.*, *108*, D23, 4740-4758, doi:10.1029/2003JD003721.
- Kim, M.-H., et al. (2013), Comparison of aerosol optical depth between CALIOP and MODIS-Aqua for CALIOP aerosol subtypes over the ocean, *J. Geophys. Res.*, *118*, 13,241–13,252, doi:10.1002/2013JD019527.
- Kondo, Y., et al. (2011), Emissions of black carbon, organic, and inorganic aerosols from biomass burning in North America and Asia in 2008, *J. Geophys. Res.*, *116*, D08204, doi:10.1029/2010JD015152.
- Koven, C. D. and I. Fung (2006), Inferring dust composition from wavelength-dependent absorption in Aerosol Robotic Network (AERONET) data, *J. Geophys. Res.*, *111*, D14205, doi:10.1029/2005JD006678.
- Lack, D. A., and C. D. Cappa (2010), Impact of brown and clear carbon on light absorption enhancement, single scatter albedo and absorption wavelength dependence of black carbon, *Atmos. Chem. Phys.*, *10*, 4207–4220. doi:10.5194/acp-10-4207-2010.

- Lack, D. A., et al. (2008), Bias in filter-based aerosol light absorption measurements due to organic aerosol loading: Evidence from ambient measurements, *Aer. Sci. Tech.*, 42(12), 1033-1041, doi:10.1080/02786820802389277.
- Langmann, B. (2013), Volcanic ash versus mineral dust: Atmospheric processing and environmental and climate impacts, *ISRN Atmospheric Sciences*, 245076, 1-17, <http://dx.doi.org/10.1155/2013/245076>.
- Leaitch, W. R., et al. (2009), Evidence for Asian dust effects from aerosol plume measurements during INTEX-B 2006 near Whistler, BC, *Atmos. Chem. Phys.*, 9, 3523-3546, 2009.
- Lewis, K., W. P. Arnott, H. Moosmüller, and C. E. Wold (2008), Strong spectral variation of biomass smoke light absorption and single scattering albedo observed with a novel dual-wavelength photoacoustic instrument, *J. Geophys. Res.*, 113, D16203. doi:10.1029/2007JD009699.
- Li, Z., X. Xia, M. Cribb, W. Mi, B. Holben, P. Wang, H. Chen, S.-C. Tsay, T. Eck, F. Zhao, E. Dutton, and R. Dickerson (2007a), Aerosol optical properties and its radiative effects in Northern China, *J. Geophys. Res.*, 112, D22S01, doi:10.1029/2006JD007382.
- Li, Z., H. Chen, M. Cribb, R. Dickerson, B. Holben, C. Li, D. Lu, Y. Luo, H. Maring, and G. Shi (2007b), Preface to special section on East Asian Studies of Tropospheric Aerosols: An International Regional Experiment (EAST-AIRE), *J. Geophys. Res.*, 112(D22), D22S00, doi:10.1029/2007JD008853.

- Li, Z., F. Niu, J. Fan, Y. Liu, D. Rosenfeld, and Y. Ding (2011), Long-term impacts of aerosols on the vertical development of clouds and precipitation, *Nat. Geosci.*, *4*, doi: 10.1038/NGEO1313.
- Ling, X.-L., et al. (2011), A case study of a typical dust storm event over the Loess Plateau of Northwest China, *Atmos. Oceanic Sci. Lett.*, *4*, 344–348.
- Liu, X., et al. (2005), Global modeling of aerosol dynamics: Model description, evaluation, and interactions between sulfate and nonsulfate aerosols, *J. Geophys. Res.*, *110*, D18206, doi:10.1029/2004JD005674.
- Loeb, N. G., N. Manalo-Smith, S. Kato, W. F. Miller, S. K. Gupta, P. Minnis, and B. A. Wielicki (2003), Angular distribution models for top-of-atmosphere radiative flux estimation from CERES instrument on the TRMM satellite, Part I: Methodology, *J. Appl. Meteor.*, *42*, 240-265.
- Logan, T., B. Xi, X. Dong, R. Obrecht, Z. Li, and M. Cribb (2010), A study of Asian dust plumes using satellite, surface, and aircraft measurements during the INTEX-B field experiment, *J. Geophys. Res.*, *115*, D00K25.
- Logan, T., B. Xi, X. Dong, Z. Li, and M. Cribb (2013a), Classification and investigation of Asian aerosol properties, *Atmos. Chem. Phys.*, *13*, 2253-2265, [www.atmos-chem-phys.net/13/2253/2013/](http://www.atmos-chem-phys.net/13/2253/2013/)doi:10.5194/acp-13-2253-2013.
- Logan, T., B. Xi, and X. Dong (2013b), A Comparison of the Mineral Dust Absorptive Properties from Two Asian Dust Events, *Atmosphere*, *4*(1), 1-16; doi:10.3390/atmos4010001.

- Logan, T., B. Xi, and X. Dong (2013c), Biomass Burning Aerosol Properties over the Northern Great Plains during the 2012 Warm Season, *Atmos. Chem. Phys. Discuss.*, 13, 32,269–32,289, [www.atmos-chem-phys-discuss.net/13/32269/2013/doi:10.5194/acpd-13-32269-2013](http://www.atmos-chem-phys-discuss.net/13/32269/2013/doi:10.5194/acpd-13-32269-2013).
- Logan, T., B. Xi, and X. Dong (2014), Aerosol properties and their influences on marine boundary layer cloud condensation nuclei at the ARM mobile facility over the Azores, *J. Geophys. Res.*, 119, doi:10.1002/2013JD021288.
- Mack, L. A., et al. (2010), Optical closure experiments for biomass smoke aerosols, *Atmos. Chem. Phys.*, 10, 9017–9026, [www.atmos-chem-phys.net/10/9017/2010/doi:10.5194/acp-10-9017-2010](http://www.atmos-chem-phys.net/10/9017/2010/doi:10.5194/acp-10-9017-2010).
- Martins, J. V., et al. (1998a), Effects of black carbon content, particle size, and mixing on light absorption by aerosols from biomass burning in Brazil, *J. Geophys. Res.*, 103, D4, 32,041-32,050.
- Martins, J. V., et al. (1998b), Sphericity and morphology of smoke particles from biomass burning in Brazil, *J. Geophys. Res.*, 103, D4, 32,051-32,057.
- Martins, J., D. Tanré, L. Remer, Y. Kaufman, S. Mattoo, and R. Levy (2002), MODIS cloud screening for remote sensing of aerosols over oceans using spatial variability, *Geophys. Res. Lett.*, 29, 8009, doi:10.1029/2001GL013252.
- Matthews, G., K. Priestley, P. Spence, D. Cooper and D. Walikainen (2005), Compensation for spectral darkening of short wave optics occurring on the Cloud's and the Earth's Radiant Energy System, *Earth Observing Systems X (Proc. SPIE)*, 588212.

- Maxwell-Meier, K., R. Weber, C. Song, D. Orsini, Y. Ma, G. R. Carmichael, and D. G. Streets (2004), Inorganic composition of fine particles in mixed mineral dust–pollution plumes observed from airborne measurements during ACE-Asia, *J. Geophys. Res.*, *109*, D19S07, doi:10.1029/2003JD004464.
- McNaughton, C. S., et al. (2009), Observations of heterogeneous reactions between Asian pollution and mineral dust over the Eastern North Pacific during INTEX-B, *Atmos. Chem. Phys. Discuss.*, *9*, 8469–8539, 2009, <http://www.atmos-chem-phys-discuss.net/9/8469/2009/>.
- Meng, Z., et al. (2010), Single-scattering properties of tri-axial ellipsoidal mineral dust aerosols: A database for application to radiative transfer calculations, *J. Aer. Sci.*, *41*, 501–512.
- Murayama, T., N. Sugimoto, I. Uno, K. Kinoshita, K. Aoki, N. Hagiwara, Z. Liu, I. Matsui, T. Sakai, T. Shibata, K. Arao, B.-J. Sohn, J.-G. Won, S.-C. Yoon, T. Li, J. Zhou, H. Hu, M. Abo, K. Iokibe, R. Koga, and Y. Iwasaka (2001), Ground-based network observation of Asian dust events of April 1998 in East Asia, *J. Geophys. Res.*, *106*, D16, 18,345-18,359.
- Osborne, S. R. and J. M. Haywood (2005), Aircraft observations of the microphysical and optical properties of major aerosol species, *Atmos. Res.*, *73*, 173-201.
- Owen, R. C., O. R. Cooper, A. Stohl, and R. E. Honrath (2006), An analysis of the mechanisms of North American pollutant transport to the central North Atlantic lower free troposphere, *J. Geophys. Res.*, *111*, D23S58, doi:10.1029/2006JD007062.

- Pan, L., et al. (2010), Aerosol optical properties based on ground measurements over the Chinese Yangtze Delta Region, *Atmos. Environ.*, *44*, 2587-2596.
- Pathak, R. K., W. S. Wu, and T. Wang (2009), Summertime PM<sub>2.5</sub> ionic species in four major cities of China: nitrate formation in an ammonia-deficient atmosphere, *Atmos. Chem. Phys.*, *9*, 1711–1722, [www.atmos-chem-phys.net/9/1711/2009/](http://www.atmos-chem-phys.net/9/1711/2009/).
- Pope, C. A. (2004), Air pollution and health – good news and bad, *N. Engl. J. Med.*, *351*(11), 1132-4.
- Qiu, J. H., and J. Sun (1994), Optical remote sensing of the dust storm and the analysis, *Chin. J. Atmos. Sci.*, *18*, 1-10.
- Qiu, Y.-J., et al. (2013), Effects of Clouds and Aerosols on Surface Radiation Budget Inferred from DOE AMF at Shouxian, China, *Atmos. Oceanic. Sci. Lett.*, *6*(1), 1-5.
- Qu, W.J., X. Y. Zhang, R. Arimoto, D. Wang, Y. Q. Wang, L. W. Yan, and Y. Li (2008), Chemical composition of the background aerosol at two sites in southwestern and northwestern China: potential influences of regional transport, *Tellus*, *60B*, 657-673.
- Ramanathan, V., P. J. Crutzen, J. T. Kiehl, D. Rosenfeld (2001), Aerosols, Climate, and the Hydrological Cycle, *Science*, *294*, 2119, doi: 10.1126/science.
- Reid, J. S. and P. V. Hobbs (1998), Physical and optical properties of young smoke from individual biomass fires in Brazil, *J. Geophys. Res.*, *103*, 32,013-32,030.
- Reid, J. S., et al. (1998), Physical, chemical, and optical properties of regional hazes dominated by smoke in Brazil, *J. Geophys. Res.*, *103*, 32,059-32,080.

- Reid, J. S., et al. (1999), Use of the Angström exponent to estimate the variability of optical and physical properties of aging smoke particles in Brazil, *J. Geophys. Res.*, *104*, D22, 27,473-27,489.
- Remer, L. A., et al. (1998), Biomass burning aerosol size distribution and modeled optical properties, *J. Geophys. Res.*, *103*, D24, 31,879-31,891.
- Remer, L., Y. Kaufman, D. Tanré, S. Mattoo, S. Chu, J. Martins, R.-R. Li, C. Ichoku, R. Levy, R. Kleidman, T. Eck, E. Vermote, and B. Holben (2005), The MODIS aerosols algorithm, products, and validation, *J. Atmos. Sci.*, *62*, 947-973.
- Rémillard, J., P. Kollias, E. Luke, and R. Wood (2012), Marine boundary layer cloud observations in the Azores, *J. Climate*, *25*, doi: 10.1175/JCLI-D-11-00610.1, 7381-7398.
- Robock, A. (1998), Enhancement of surface cooling due to forest fire smoke, *Science*, *242*, 911-913.
- Rolph, G.D. (2012), Real-time Environmental Applications and Display sYstem (READY) Website (<http://ready.arl.noaa.gov>). NOAA Air Resources Laboratory, Silver Spring, MD.
- Rosenfeld, D., U. Lohmann, G. B. Raga, C. D. O'Dowd, M. Kulmala, S. Fuzzi, A. Reissell, and M. O. Andreae (2008), Flood or drought: How do aerosols affect precipitation? *Science*, *321*, 1309-1313, doi:10.1126/science.1160606.
- Russell, P. B., et al. (2010), Absorption Angström Exponent in AERONET and related data as an indicator of aerosol composition, *Atmos. Chem. and Phys.*, *10*, 1155–1169, [www.atmos-chem-phys.net/10/1155/2010/](http://www.atmos-chem-phys.net/10/1155/2010/).

- Saleh, R., et al. (2013), Absorptivity of brown carbon in fresh and photo-chemically aged biomass-burning emissions, *Atmos. Chem. Phys.*, *13*, 7683–7693, [www.atmos-chem-phys.net/13/7683/2013/doi:10.5194/acp-13-7683-2013](http://www.atmos-chem-phys.net/13/7683/2013/doi:10.5194/acp-13-7683-2013).
- Schuster, G. L., et al. (2005), Inferring black carbon content and specific absorption from Aerosol Robotic Network (AERONET) aerosol retrievals, *J. Geophys. Res.*, *110*, D10S17. doi:10.1029/2004JD004548.
- Schuster, G. L., O. Dubovik, and B. N. Holben (2006), Angstrom exponent and bimodal aerosol size distributions, *J. Geophys. Res.*, *111*, D07207, doi:10.1029/2005JD006328.
- Seifert, P., et al. (2011), Ice formation in ash-influenced clouds after the eruption of the Eyjafjallajökull volcano in April 2010, *J. Geophys. Res.*, *116*, D00U04, doi:10.1029/2011JD015702.
- Singh, H. B., W. H. Brune, J. H. Crawford, H. Fuelberg, and D. J. Jacob (2006), The Intercontinental Chemical Transport Experiment – Phase B (INTEX-B): An update. [Available online at [http://avdc.gsfc.nasa.gov/Documentation/Validation\\_Plan/PDF/INTEXB\\_WhitePaper.pdf](http://avdc.gsfc.nasa.gov/Documentation/Validation_Plan/PDF/INTEXB_WhitePaper.pdf).]
- Smirnov, A., B. N. Holben, O. Dubovik, N. T. O'Neill, T. F. Eck, D. L. Westphal, A. K. Goroch, C. Pietras, and I. Slutsker (2002), Atmospheric aerosol optical properties in the Persian Gulf, *J. Atmos. Sci.*, *59*, 620-634.
- Sun, J., M. Zhang, and T. Liu (2001), Spatial and temporal characteristics of dust storms in China and its surrounding regions, 1960-1999: Relations to source area and climate, *J. Geophys. Res.*, *106*, 10,325-10,333.

- Sun, Y., et al. (2005), Chemical composition of dust storms in Beijing and implications for the mixing of mineral aerosol with pollution aerosol on the pathway, *J. Geophys. Res.*, *110*, D24209, doi:10.1029/2005JD006054.
- Takemura, T., et al. (2002), Single-Scattering Albedo and Radiative Forcing of Various Aerosol Species with a Global Three-Dimensional Model, *J. Clim.*, *15*(4), 333-352.
- Tanré, D., Y. Kaufman, M. Herman, and S. Matoo (1997), Remote sensing of aerosol properties over oceans using the MODIS/EOS spectral radiances, *J. Geophys. Res.*, *102*, 16,971-16,988.
- Tanré, D., Y. J. Kaufman, B. N. Holben, B. Chatenet, A. Karnieli, F. Lavenu, L. Blarel, O. Dubovik, L. A. Remer, and A. Smirnov (2001), Climatology of dust aerosol size distribution and optical properties derived from remotely sensed data in the solar spectrum, *J. Geophys. Res.*, *106*, D16, 18,205-18,217.
- Tao, W.-K., J.-P. Chen, Z. Li, C. Wang, and C. Zhang (2012), Impact of aerosols on convective clouds and precipitation, *Rev. Geophys.*, *50*, RG2001, doi:10.1029/2011RG000369.
- Tsunematsu, N., K. Kenji, T. Matsumoto (2005), The Influence of Synoptic-Scale Air Flow and Local Circulation on the Dust Layer Height in the North of the Taklimakan Desert, *Water, Air, and Soil Pollution*, *5*, 175-193.
- Uematsu, M, R. A. Duce, J. M. Prospero, L. Chen, J. T. Merrill, and R. L. McDonald (1983), Transport of mineral aerosol from Asia over the North Pacific Ocean, *J. Geophys. Res.*, *88*, C9, 5343-5352.

- Val Martin, M., R. E. Honrath, R. C. Owen, G. Pfister, P. Fiahlo, and F. Barata (2013), Significant enhancements of nitrogen oxides, black carbon, and ozone in the North Atlantic lower free troposphere resulting from North American boreal wildfires, *J. Geophys. Res.*, *111*, D23S60, doi:10.1029/2006JD007530.
- Virkkula, A., et al. (2005), Modification, Calibration and a Field Test of an Instrument for Measuring Light Absorption by Particles, *Aerosol Sci. and Tech.*, *39*, 68-83.
- Virkkula, A. (2010), Correction of the calibration of the 3-wavelength Particle Soot Absorption Photometer (PSAP), *Aerosol Sci. Tech.*, *44*, 706-712.
- Wang, X., et al. (2010), Surface measurements of aerosol properties over northwest China during ARM China 2008 deployment, *J. Geophys. Res.*, *115*, D00K27, doi:10.1029/2009JD013467.
- Wang, Y., et al. (2011), Seasonal variations in aerosol optical properties over China, *J. Geophys. Res.*, *116*, D18209, doi:10.1029/2010JD015376.
- Wielicki, B. A., B. R. Barkstrom, E. F. Harrison, R. B. Lee III, G. L. Smith, and J. E. Cooper (1996), Clouds and the Earth's Radiant Energy System (CERES): An Earth Observing System Experiment, *Bull. Amer. Meteor. Soc.*, *77*, 853-868.
- Winker, D. M., et al. (2007), Initial performance assessment of CALIOP, *Geophys. Res. Lett.*, *34*(19), L19803, doi:10.1029/2007GL030135.
- Wood, R., et al. (2014), Clouds, aerosol, and precipitation in the marine boundary layer: An ARM mobile facility deployment. Accepted by Bull. Amer. Meteor. Soc.
- Xin, J., et al. (2007), Aerosol optical depth (AOD) and Ångström exponent of aerosols observed by the Chinese Sun Hazemeter Network from August 2004 to September 2005, *J. Geophys. Res.*, *112*, D05203. doi:10.1029/2006JD007075.

- Yang, Y. Q., et al. (2008), Sand/dust storm processes in Northeast Asia and associated large-scale circulations, *Atmos. Chem. Phys.*, 8, 25–33, [www.atmos-chem-phys.net/8/25/2008/](http://www.atmos-chem-phys.net/8/25/2008/).
- Yang, M., et al. (2009), Attribution of aerosol light absorption to black carbon, brown carbon, and dust in China – interpretations of atmospheric measurements during EAST-AIRE, *Atmos. Chem. Phys.*, 9, 2035–2050, [www.atmos-chem-phys.net/9/2035/2009/](http://www.atmos-chem-phys.net/9/2035/2009/).
- Yao, X., et al. (2002), The water-soluble ionic composition of PM<sub>2.5</sub> in Shanghai and Beijing, China, *Atmos. Environ.*, 36, 4223–4234.
- Yi, B. et al. (2011), Radiative transfer simulation of dust-like aerosols: Uncertainties from particle shape and refractive index, *J. Aer. Sci.*, 42, 631–644.
- Yoon, Y. J., et al. (2007), Seasonal characteristics of the physicochemical properties of North Atlantic marine atmospheric aerosols, *J. Geophys. Res.*, 112, D04206, doi:10.1029/2005JD007044.
- Yu, H., M. Chin, L. A. Remer, R. G. Kleidman, N. Bellouin, H. Bian, and T. Diehl (2009), Variability of marine aerosol fine-mode fraction and estimates of anthropogenic aerosol component over cloud-free oceans from the Moderate Resolution Imaging Spectroradiometer (MODIS), *J. Geophys. Res.*, 114, D10206, doi:10.1029/2008JD010648.
- Zheng, M., et al. (2005), Seasonal trends in PM<sub>2.5</sub> source contributions in Beijing, China, *Atmos. Environ.*, 39, 3967–3976.